



THE HONG KONG
POLYTECHNIC UNIVERSITY

香港理工大學

Pao Yue-kong Library

包玉剛圖書館

Copyright Undertaking

This thesis is protected by copyright, with all rights reserved.

By reading and using the thesis, the reader understands and agrees to the following terms:

1. The reader will abide by the rules and legal ordinances governing copyright regarding the use of the thesis.
2. The reader will use the thesis for the purpose of research or private study only and not for distribution or further reproduction or any other purpose.
3. The reader agrees to indemnify and hold the University harmless from and against any loss, damage, cost, liability or expenses arising from copyright infringement or unauthorized usage.

IMPORTANT

If you have reasons to believe that any materials in this thesis are deemed not suitable to be distributed in this form, or a copyright owner having difficulty with the material being included in our database, please contact lbsys@polyu.edu.hk providing details. The Library will look into your claim and consider taking remedial action upon receipt of the written requests.

**SYNTHESIS OF AU NANORODS-BASED
PLASMONIC NANOSTRUCTURES AND THEIR
APPLICATIONS IN MONITORING AND
PROMOTING CHEMICAL REACTIONS**

BAO ZHIYONG

Ph.D

The Hong Kong Polytechnic University

2018

The Hong Kong Polytechnic University
Department of Applied Physics

**Synthesis of Au Nanorods-based Plasmonic
Nanostructures and Their Applications in Monitoring
and Promoting Chemical Reactions**

BAO Zhiyong

A thesis submitted in partial fulfillment of the requirements for
the degree of Doctor of Philosophy

February 2017

CERTIFICATE OF ORIGINALITY

I hereby declare that this thesis is my own work and that, to the best of my knowledge and belief, it reproduces no material previously published or written, nor material that has been accepted for the award of any other degree or diploma, except where due acknowledgement has been made in the text.

_____ (Signed)

_____ BAO Zhiyong (Name of student)



Abstract

Noble metal nanoparticles (NPs) made of, for instance, Au and Ag, have attracted great attention because of their intriguing plasmonic behaviors arising from the collective oscillations of free electrons. Under resonant excitation conditions, the metal nanoparticles exhibit large scattering and absorption cross sections, as well as great electromagnetic field enhancement. These distinctive plasmonic behaviors can serve as the basis for using localized surface plasmons-based nanosensors to locally detect nanoscale environmental changes, such as molecular-binding events, plasmon-enhanced spectroscopies, biosensing and plasmon-enhanced chemical reactions. For example, surface-enhanced Raman scattering (SERS) spectroscopy can be used as a sensitive optical probe for monitoring of the catalytic reaction process. In this thesis work, Au nanorods-based plasmonic nanostructures have been fabricated and their various applications have been demonstrated. Details of the thesis work include:

In the first part of this thesis, Pt NPs-decorated Au nanorods (NRs) with tunable localized surface plasmon resonance wavelength have been fabricated. It has been demonstrated that the controlled surface density of Pt NPs is a vital influence on both the SERS enhancement and catalytic efficiency. The optimized Au@Pt NRs hybrid has been used to monitor in real time the catalytic reaction process of 4-nitrothiophenol (4-NTP) to 4-aminothiophenol (4-ATP).

In the second part, Au@Ag core-shell nanocuboids (CSNCs) have been prepared to promote the chiral cysteine molecules assembly process by recording the changes in the intensities of induced circular dichroism (CD) peaks with the reaction time. Comprehensive experiments and simulations reveal that the formation of an extended



helical network of cysteine molecules on the Ag surface is responsible for the origin of the new CD band that is strongly amplified by the interband transition of Ag through Coulomb coupling and enhanced local fields around the Au@Ag CSNC.

In the third part of this work, anisotropic C_3N_4 nanosheets/Au@Pt NRs heterostructures have been fabricated. This kind of anisotropic heterocatalyst can increase photocatalytic H_2 generation rate to 150% compared to the nanosheets where Au NRs and Pt NPs reside individually because of the effective electron separation and cascading transfer process. Moreover, different underlying mechanisms responsible for the observed wavelength-dependent photocatalytic performance as well as the mutative hydrogen evolution augmentation with altered irradiation wavelength range are investigated.

It is believed that the rational design and preparation of plasmonic bimetallic nanostructures or heterostructure complex not only offers new horizons for diverse functionalities of each single entity, but also flourish the applications of plasmons in catalysis, life sciences, and energy fields.



List of Publications and Conference Presentations

List of Publications

1. **Z. Y. Bao**, W. Zhang, Y.-L. Zhang, J. J. He, J. Dai, C.-T. Yeung, G.-L. Law, D. Y. Lei, "Interband absorption enhanced optical activity in discrete core-shell nanocuboids: Probing extended helical conformation of chemisorbed cysteine molecules", *Angewandte Chemie International Edition*, 2017, 129, 1303-1308.
2. N. Fu[#], **Z. Y. Bao**[#], Y. L. Zhang, G. Zhang; S. Ke; P. Lin; J. Dai; D. Y. Lei, H. T. Huang, Panchromatic Thin Perovskite Solar Cells with Broadband Plasmonic Absorption Enhancement and Efficient Light Scattering Management by Au@Ag Core-Shell Nanocuboids, *Nano Energy*, 2017, 41, 654-664 (# co-first author).
3. **Z. Y. Bao**, X. Liu, Y. Chen, Y. C. Wu, H. L. W. Chan, J. Dai, D. Y. Lei, "Quantitative SERS Detection of Low-concentration Aromatic Polychlorinated Biphenyl-77 and 2,4,6-Trinitrotoluene", *Journal of Hazardous Materials*, 2014, 280, 706-712.
4. Y. Zhao, Y. Xie, **Z. Y. Bao**, Y. H. Tsang, L. Xie, and Y. Chai. "Enhanced SERS Stability of R6G Molecules with Monolayer Graphene", *The Journal of Physical Chemistry C*, 2014, 118, 11827-11832.
5. X. Huang, Y. Zhu, X. Zhang, **Z. Y. Bao**, D. Y. Lei, W. Yu, J. Dai, Y. Wang, "Clam-inspired nanoparticle immobilization method using adhesive tape as microchip substrate", *Sensors and Actuators B: Chemical*, 2015, 222, 106-111.
6. J. J. He, W. Zheng, F. Ligmajer, C.-F. Chan, **Z. Y. Bao**, K.-L. Wong, X. Y. Chen, J.



H. Hao, J. Y. Dai, S.-F. Yu, D. Y. Lei, "Plasmonic enhancement and polarization dependence of nonlinear upconversion emissions from single gold nanorod@SiO₂@CaF₂:Yb³⁺, Er³⁺ hybrid core-shell-satellite nanostructures, *Light: Science & Applications*, 2017, 6, e16217; doi:10.1038/lisa.2016.217.

7. F.-W. Kang, J. J. He, T. Y. Sun, **Z. Y. Bao**, F. Wang, D. Y. Lei, "Plasmonic dual-enhancement and precise color tuning of gold nanorod@SiO₂ coupled core-shell-shell upconversion nanocrystals", *Advanced Functional Materials*, 2017, 27, 1701842(1-11).

Conference presentations

1. *Global Student Conference 2016 & Global Nanophotonics 2016*, Oral: Hotspot-mediated chiroptical transfer and amplification effect, **Z. Y. Bao**, J. Dai, K. H. Ho, S. Li, G. Zheng, J. He, W. Zhang, D. Y. Lei, **Osaka**, 2016.
2. *The 18th Conference of The Physical Society of Hong Kong*, Poster: Bifunctional Au@Pt core-shell nanostructures for *in situ* monitoring of catalytic reactions by surface enhanced Raman scattering spectroscopy, **Z. Y. Bao**, D. Y. Lei, R. Jiang, X. Liu, J. Dai, J. Wang, H. L. W. Chan and Y. H. Tsang, **Hong Kong**, 2015.
3. *PIERS2014, Progress In Electromagnetics Research Symposium*, **Poster**: Label-free and high-sensitivity SERS detection of organic pollutants and explosive substances using bifunctional nanostructures, **Z. Y. Bao**, X. Liu, Y. Chen, Y. Wu, H. L.W. Chana, J. Dai, D. Y. Lei, **Guangzhou**, 2014.



Acknowledgements

There are too many people deserve my incredible gratitude for their encouragement and support in my Hong Kong study period.

Firstly, I am of very gratefulness to my supervisor, Prof. Jiyan Dai, for providing the opportunity for me to pursue my PhD study here. He gives me a great many valuable suggestions on both my study and life. Under his supervision I have practiced the art of kindly and efficiently collaborating with other researchers. Without his keen guidance and continuous support, I cannot be able to complete this thesis work on time. I would also express my sincere gratitude to my co-supervisor Dr. Dangyuan Lei. His immense knowledge and high enthusiasm to the scientific research inspire me to overcome the obstacles and finish my PhD study. Without his enthusiastic guidance and generous help, I can't accomplish my doctoral study. I deeply appreciate the unselfish assistance from the collaborators, Prof. Jianfang Wang from The Chinese University of Hong Kong, Prof. Wei Zhang, from Institute of Applied Physics and Computational Mathematics of Beijing. It is also my honor to get advice and help from Prof. Feng Yan, Prof. Jianhua Hao, Dr. Peter Tsang and Dr. Xuming Zhang.

Further, I want to thanks my group members Dr. Yongliang Zhang, Mr. Guangcan Li, Dr. Guangchao Zheng, Mr. Jijun He, Dr. Zhi Zhang, Mr. Fan Zhang, Dr. Jinlai Duan and Dr. Jianhui Sun. I am very happy to make joint efforts with my colleagues, Dr. Gongxun Bai, Dr. Yang Liu and Dr. Xin Liu. I would also like to thank Dr. Ruibin Jiang from Shaanxi Normal University, Dr. Nianqing Fu from South China University of Technology, Dr. Yidong Hou from Sichuan University for their cooperation and support in our collaborative works. I feel grateful to the technicians who supported me in my PhD study. I would like to appreciate Dr. Wei Lu and Dr. Vincent Chan for their guidance in the department facility.

Besides, my sincere gratitude is given to Dr. Shenghua Liu, Dr. Yuda Zhao, Dr.



Hui Long, Dr. Li Chen, Dr. Xiaowen Huang and Dr. Xiao Wu. Your accompanying and encouragement bring me too much pleasure and happiness, making me joyful toward the life in Hong Kong.

Finally, I would like to express my deep love and cordial thanks to my parents and my family who unconditionally support and encourage me. It's you who encourage me to continuously pursue on the road of scientific research.



Table of Content

Abstract	I
List of Publications and Conference Presentations	III
Acknowledgements	V
Table of Content	VII
List of Figures	X
Chapter 1 Introduction	1
1.1 Overview of Light-matter Interactions.....	1
1.2 Surface Plasmons and Localized Surface Plasmon Resonances.....	2
1.3 Plasmonic Applications of Au NRs.....	5
1.3.1 Surface-enhanced Raman Scattering.....	7
1.3.2 Photothermal Therapy	9
1.3.3 Plasmonic Nanoantennas	11
1.3.4 Plasmon-enhanced Circular Dichroism.....	12
1.3.5 Plasmon-assisted Photochemical Reactions.....	13
1.4 Motivation of the Thesis Work.....	15
1.5 Outline of the Thesis	16
References	17
Chapter 2 Experimental Instruments, Sample Preparations, Theory and Simulations	19
2.1 Sample Preparations.....	19
2.2 Characterization methods.....	21
2.3 Theory and Simulation	23
2.3.1 Theoretical Background	24
2.3.2 Finite-difference Time-domain (FDTD) Simulation Method	26
References	28
Chapter 3 Au@Pt NRs for <i>in-situ</i> Monitoring of Catalytic Reactions by SERS	29
3.1 Introduction	29



3.2 Synthesis of Au@Pt core-shell Nanostructures	31
3.3 Optical and Morphological Characterizations of Au@Pt NRs	31
3.4 Monitoring of Catalytic Reactions of the Au@Pt NRs by SERS	35
3.4.1 Catalytic Activity of Au@Pt NRs.....	35
3.4.2 Recyclability of Catalysts	39
3.4.3 SERS Activity of the Au@Pt NRs	40
3.4.4 Mechanisms for the Different SERS Enhancements	42
3.4.5 Reproducibility and Stability of SERS Substrates	44
3.4.6 Monitoring of Catalytic Reaction by the SERS Substrates.....	45
3.5 Summary	48
References	48
Chapter 4 Interband Absorption Enhanced Optical Activity by Au@Ag nanocuboids	51
4.1 Introduction.....	51
4.2 Morphological Characterizations of Au@Ag Nanocuboids	53
4.3 Characterizations of Conformation Change of Cysteine on Ag Surface.....	55
4.4 Interband Absorption Enhanced CD	57
4.4.1 The Unusual Observed CD in Au@Ag/cysteine System	57
4.4.2 The Generality of Observed CD	58
4.4.3 Ag-exclusive Feature of Induced CD	60
4.4.4 Mechanism Discussion of Induced CD.....	61
4.4.5 Generality of Induced CD for Probing Conformational Changes of Other Molecules	71
4.4.6 Simulation Model.....	74
4.5 Summary	76
References	77
Chapter 5 Au@Pt/C ₃ N ₄ Complex for Plasmon-enhanced Photocatalytic hydrogen Evolution.....	81



5.1 Introduction.....	81
5.2 Experimental Methodology.....	83
5.2.1 Synthesis of Samples.....	83
5.2.2 Hydrogen Production and Photocurrent Experiments.....	84
5.2.3 Morphological and Componential Characterization of samples.....	85
5.2.3 The Advantages of Samples with Anisotropic Configuration.....	88
5.2.4 The Electric Property and Chemical Status of Samples.....	89
5.2.5 The Hydrogen Evolution Experiments.....	93
5.2.6 Mechanisms for the plasmon-enhanced hydrogen evolution.....	97
5.3 Summary	105
References	105
Chapter 6 Conclusion and Future Prospect.....	109



List of Figures

- Figure 1.1 Collective oscillation of free electrons excited by incident electromagnetic field in an Au nanosphere.3
- Figure 1.2 Lycurgus cup, which looks green (left view) when it is illuminated from the outside, but red (right view) when illuminated from inside of the cup.³¹5
- Figure 1.3 Dependence of the plasmonic properties of Au NRs on the aspect ratio. (a) Schematic showing Au NRs with a fixed diameter but different aspect ratios.³² (b) Simulated dependence of the extinction spectra on the aspect ratio. (c) TEM images of prepared Au NRs. (d) Electric field enhancement contour of an Au NR with an aspect ratio of 2.....6
- Figure 1.4 Tuning the LSPRs wavelengths of Au NRs. (a) Extinction spectra obtained at a fixed time interval after the addition of H₂O₂. (b) NR shortening rate versus the volume ratio between H₂O₂ and the NR solution. (c)-(g) TEM images of different shortened Au NRs.³².....7
- Figure 1.5 (a) TEM images and (b) extinction properties of the self-assembled NRs. (c) Evolution of normalized ensemble-averaged SERS spectra in self-assembled NR chains. (d) Variation in the normalized SERS peak intensity measured at 563 cm⁻¹ plotted as a function of the average aggregation number of the NR chains.³³9
- Figure 1.6 Site-dependent photothermolysis mediated by F-NRs (red). (a,b) Cells with membrane-bound F-NRs exposed to cw NIR laser irradiation. (c,d) Cells with internalized F-NRs required 60 mW to produce a similar level of response. (e,f) F-NRs internalized in KB cells labeled by folate-Bodipy (green) were exposed to laser irradiation at 60 mW, resulting in both membrane blebbing and disappearance (melting) of the F-NRs. (g,h) NIH-3T3 cells were unresponsive to F-NRs, and did not suffer photoinduced damage upon 60 mW laser irradiation. (i,j) Cells with

membrane-bound F-NRs exposed to fs-pulsed laser irradiation produced membrane blebbing at 0.75 mW. (k,l) Cells with internalized F-NRs remained viable after fs-pulsed irradiation at 4.50 mW, as indicated by a strong calcein signal (green).³⁴ 10

Figure 1.7 Emission and scattering polarization of the Au nanorod-fluorophore hybrid nanostructures: (a) schematic showing a single hybrid nanostructure; (b) TEM image of a representative nanostructure sample; (c) Degree of polarizations (DOPs) of the scattering (blue squares) and fluorescence emission (red circles) from the hybrid nanostructure vs the LSPR wavelength. The black solid triangles are the calculated DOPs of the plasmon-enhanced excitation electric field intensity. The dashed curves are guides for the eyes.³⁵ 11

Figure 1.8 (a) UV-vis-NIR spectra of the original Au NRs and 1D self-assembled Au NRs formed by three types of Cys; (b) SEM image of the 1D self-assembled Au NRs; (c) CD spectra of original Au NRs and assembled Au NRs by different Cys.³⁶ 13

Figure 1.9 (a) TEM image of Au NR/TiO₂ nanodumbbell. (b) Structure and mechanism of operation under visible light of an individual Au NR/TiO₂ dumbbell. Comparison of (c) H₂ evolution rate by various catalysts, and (d) normalized concentration of methylene blue vs irradiation time; both under visible illumination and in the presence of methanol and water.³⁷ 14

Figure 2.1 Schematic showing a Yee cell used in FDTD simulations.⁴ 27

Figure 3.1 Morphology and composition characterizations of Au@Pt nanostructures. (a), (b) and (c) show the TEM images of Au and Au@Pt samples. (d) and (e) are the element mapping of Au and Pt. (f) The EDX map spectrum. 32

Figure 3.2 TEM images of the Au@Pt hybrid nanostructures with gradual



increase in the surface coverage of Pt NPs on Au NRs.	33
Figure 3.3 (a) Absorption spectra of two kinds of Au NRs. (b) Absorption spectra were measured for the four hybrid nanostructures.	34
Figure 3.4 Representation of the reduction of 4-NTP by NaBH ₄ to 4-ATP, which takes place on Au@Pt superstructure surfaces. The reaction is catalyzed by the Pt NPs, while the SERS signal is brought about by local optical fields of the Au NRs.	36
Figure 3.5 (a)-(c) Absorption spectra of the 4-NTP solution mixed respectively with the Au@Pt superstructures. (d) Normalized concentration of 4-NTP as a function of time.	37
Figure 3.6 (a) The plot of $\ln(A_{410(t)}/A_{410(0)})$ as a function of time for the reaction catalyzed by different samples. (b) Three cycles of catalytic activity of the Au@Pt-c hybrids.	39
Figure 3.7 TEM images of Au@Pt core/shell nanostructures before (a) and (b) and after (c) and (d) three cycles.	40
Figure 3.8 (a), (b) Measured SERS responses and (c), (d) calculated near-field for different Au@Pt samples.	41
Figure 3.9 (a): SERS spectra collected for 4-NTP molecules adsorbed on two types of Au NRs with LSPR wavelengths at 628 nm (black curve) and 693 nm (red curve), respectively. (b) SERS spectra for the same measurements as that in (a) while the laser excitation wavelength is changed to 488 nm.	44
Figure 3.10 The SERS-RSD spectrum of 4-NTP molecules in the Raman shift range of 1000-1700 cm ⁻¹ , randomly collected from a number of positions on the Au@Pt core/shell substrate.	45
Figure 3.11 SERS spectroscopy recorded upon addition of different amounts of the NaBH ₄ with Au@Pt nanohybrids. (a) Raman spectra recorded from 4-NTP molecules. (b) Raman intensities extracted from (a) at the	



bands 1340, 1160 and 1590 cm^{-1} , respectively.....	46
Figure 4.1 Morphology and composition characterizations of as-prepared Au@Ag CSNCs.	54
Figure 4.2 FT-IR spectra of L-cys and Au@Ag/L-cys solution.....	55
Figure 4.3 ^1H NMR spectra of L-cysteine and L-cysteine absorbed Au@Ag CSNCs solution.....	56
Figure 4.4 (a) Extinction spectra. (b) CD spectra. (c) Simulated surface charge and electric near-field distributions in an Au@Ag CSNC structure at different wavelengths.	58
Figure 4.5 UV and CD spectra of Ag NSs/cysteine system.	59
Figure 4.6 (a) TEM of as-prepared Ag NRs. (b) CD spectra of L-/D-cysteine-adsorbed Ag NRs.	60
Figure 4.7 Measured CD spectra for L-cysteine-coated Au NSs of diameter 20 nm (A) and 60 nm (B), and (C) Au NRs. All the spectra show no induced CD signal above the level of background noise.	61
Figure 4.8 (a) Quantum transitions in the cysteine-coated Au@Ag CSNC system. (b) It shows the simulated charge distributions and electric near-field at wavelength 300 nm for an Au@Ag CSNC and Ag NS, respectively. (c) The real and imaginary parts of the electric permittivity for bulk Ag.	62
Figure 4.9 (a) Measured CD spectra for the hybrid L-cysteine-coated Au@Ag CSNC as a function of reaction time. (b) Time evolution of the CD as a function of temperature.	64
Figure 4.10 (a1-3) Schematic representations of three possible charge states in a cysteine molecule. (b) Formation of an extended helical network and high-pH-enabled dissociation of COOH-NH_2 (right).	65
Figure 4.11 (a) Measured CD spectra for the complex with decreasing the solution pH from 7 to 4. (b) Measured CD spectra for the Au@Ag-L-	



cysteine complex with increasing the solution pH from 7 to 10. (c) pH-switched CD “active” and “silence” of the complex.	66
Figure 4.12 (a-b) Schematic diagram showing the block effect of PSS ions. (c) Measured CD spectra for the complex with increasing the PSS concentration.	68
Figure 4.13 SERS spectra of bare Au@Ag CSNCs (black curve) and the complex solution measured with different time.	69
Figure 4.14 Measured CD spectra of the hybrid D-cysteine-coated Au@Ag CSNC with and without adding chloride ions.	70
Figure 4.15 Measured CD spectra of Ag ⁺ -L-cysteine (blue) and Ag ⁺ -D-cysteine complex (black), reproducing the previous observation of the CD signal at 360 nm due to the Ag ⁺ ...Ag ⁺ interaction.....	70
Figure 4.16 (a) CD spectra of L/D-penicillamine, L/D-penicillamine-coated Au@Ag CSNCs. (b) Chemical structures of L/D-penicillamine.....	72
Figure 4.17 (a) CD spectra of pure C-cysteine, C-cysteine-coated Au@Ag CSNCs. (b) CD spectra of pure N-cysteine, N-cysteine-coated Au@Ag CSNCs.....	73
Figure 4.18 Simulated near-field distributions at wavelength 290 nm for an Ag nanocuboid (a) and Au@Ag CSNC (b).....	74
Figure 4.19 Simulated CD spectra for an Ag NS (red curves) or an Au@Ag NP (black curves) capped with vertically-aligned right-handed (a) or left-handed spiral molecules (b), respectively. The insets show the detailed models used in the simulations.....	76
Figure 4.19 Simulated CD spectra for an Ag NS (red curves) or an Au@Ag NP (black curves) capped with vertically-aligned right-handed (a) or left-handed spiral molecules (b), respectively. The insets show the detailed models used in the simulations.....	76
Figure 5.1 Schematic illustration of the preparation of the Au@Pt/CNNs	



anisotropic heterogeneous nanostructure.	85
Figure 5.2 Morphological characterizations of Au@Pt/CNNs anisotropic heterogeneous nanostructures.	86
Figure 5.3 TEM images of different Au@Pt/CNNs anisotropic heterogeneous nanostructures with various Pt loading.	87
Figure 5.4 Cross-sectional view of the normalized electric-field intensity distribution profiles for the bare Au NR (a) and Au@Pt hybrids (b)-(e).	88
Figure 5.5 (a) HRTEM images of CNNs/Au@Pt NR anisotropic heterogeneous nanostructures. b) STEM image of single Au@Pt hybrid deposited on CNNs. c, d) Elemental mapping of Au and Pt in the Au@Pt hybrid, respectively. e, f) HRTEM and SEAD images for single CNNs/Au NR nanostructure.	89
Figure 5.6 a) XRD patterns of different CNNs samples. b) UV-vis spectra of Au NR and Au@Pt hybrids. c, d) Raman and UV-vis characterizations of different CNNs samples.	91
Figure 5.7 XPS spectra of (a) C 1s, (b) N 1s, (c) Au 4f and (d) Pt 4f of the Au@Pt/CNNs anisotropic heterogeneous nanostructure.	92
Figure 5.8 TEM images of Au NR/CNNs heterostructure.	93
Figure 5.9 a) Time course of H ₂ evolution over Au NR/CNNs, Au/Pt/CNNs and Au@Pt/CNNs photocatalysts. b) Photocatalytic H ₂ generation activity of Au@Pt/CNNs (0.01 wt% Pt loading). c) Photocatalytic activity comparison of Au@Pt/CNNs with various Pt loading.	95
Figure 5.10 TEM and HRTEM images of Au/Pt/CNNs hybrid nanostructure.	95
Figure 5.11 (a) PL spectra and (b) decay curves of CNNs, Au NR/CNNs, Au/Pt/CNNs and Au@Pt/CNNs photocatalysts.	98
Figure 5.12 Photocurrent-time dependence of (a) CNNs and (b)	



Au@Pt/CNNs anisotropic heterogeneous nanostructure under different light irradiation. (c)-(e) Photocurrent-time dependence of (a) CNNs and (b) Au@Pt/CNNs anisotropic heterogeneous nanostructure under different wavelength range irradiation. (f) Calculation spatially averaged E-field enhancement at 460, 520 and 750 nm of Au@Pt 99

Figure 5.13 TEM images of Au@Pt NSs/CNNs hybrid nanostructure..... 101

Figure 5.14 Photocatalytic activity comparison of Au@Pt NSs/CNNs and Au@Pt NRs/CNNs with the identical Pt loading. 102

Figure 5.15 Schematic illustration and b) proposed mechanism of H₂ evolution by the Au@Pt/CNNs anisotropic heterocatalyst under visible light irradiation. Route 1) represents the photogenerated electrons from conduction band of CNNs transfer to Au and then to Pt while route 2) indicates SPR-excitation hot electrons of Au transfer to Pt. 103



Chapter 1 Introduction

Plasmonics utilize the coupling of light to charges like electrons in metals, and allows breaking the diffraction limit for the localization of light into subwavelength dimensions enabling strong light-matter interactions and near-field enhancements.¹⁻⁴ Although theoretical descriptions for the plasmonic concepts have been well-developed in recent years, new experimental discoveries and phenomena have frequently been found and also the novel applications of multifarious plasmonic nanostructures are continuously being exploited. In this chapter, I will begin by briefly introducing the basic concepts of localized surface plasmon resonances (LSPRs) supported by noble metals nanostructures in Section 1.1. In the following (Section 1.2) the attention is focused on Au NRs as one of the most promising plasmonic nanostructures and their applications in a wide range of research areas. Then the significance of the thesis is shown in Section 1.3 to promote the comprehension. In the end (Section 1.4), the overall structure of the thesis is introduced for the reading guidance.

1.1 Overview of Light-matter Interactions

When white light passes through a prism under an appropriate condition a spectrum of colors is visible in the transmitted light, as observed by Newton a long time ago. This phenomenon stems from two reasons: one is that white light is composed of many fractions with different frequencies, the other is that light-matter interactions lead to a dispersion of the initial white light into its various components. Confinement and enhancement of light by plasmonics result in the light-matter interaction studies becoming more and more thriving. Besides, light-matter interaction is primarily vital physical process because it governs the phenomena ranging from



atomic transitions to macroorganism photosynthesis on Earth. Therefore, accurate manipulation of this interaction has become more and more impressive.⁵⁻⁸ However, light-matter interactions are normally restricted by the optical diffraction limit, which severely hinders the control ability of the light within the subwavelength scale. Amazingly, when the sizes of noble metals reach down to ~ 100 nm, these nanostructures show some distinctive characteristics that totally differ from their bulk counterparts in terms of electronic, optical and catalytic properties because of the large surface-area-to-volume ratio and the spatial confinement of the free electrons.⁹⁻¹²

Furthermore, strong light-matter interactions and electric field enhancement are generally introduced in applications such as plasmon-enhanced catalytic reactions, plasmon-enhanced photoluminescence, surface-enhanced Raman scattering (SERS) and plasmon-enhanced interactions between the molecule and metal. Note that chiral plasmonic structures have also been recently investigated for enhancing the optical activity and sensing of molecules.¹³⁻¹⁷

1.2 Surface Plasmons and Localized Surface Plasmon Resonances

Au and Ag nanocrystals are pioneering and widely studied plasmonic materials. Surface plasmon that is oscillations of free electrons in Au and Ag nanostructures can be excited by application of external electromagnetic fields. The first documented laboratory observation of collective electron oscillations in metallic nanostructures dates back to the year 1902 when Wood observed an anomaly that narrow dark bands appeared in reflection spectra of a metallic diffraction grating.¹⁸ In 1908, Mie reported the analytical solution of Maxwell's equations for the scattering of electromagnetic radiation by spherical nanoparticles (Mie scattering).¹⁹ In 1941 Fano used theoretical methods of electromagnetic surface waves on metal surfaces with finite conductivity proposed by Sommerfeld and Zenneck to explain the Wood's anomaly.²⁰ The concept

of “surface plasmon” was first presented by Ritchie in 1957.²¹ He proposed that the surface of a metallic film (the thickness of the film should not exceed the penetration depth of the evanescent field) can support coherent oscillations of conduction electrons, and he also provided the first theoretical description of surface plasmons. In 1968, Andreas Otto, Erich Kretschmann and Heinz Ritchie almost simultaneously reported the optical excitation of surface plasmons and they independently developed two convenient methods for generating surface plasmons.²² Since 1900s, the significantly expanding research in the field of plasmonics can be attributed to the development of numerical methods for precisely controlling noble metal nanocrystals of different geometries, as well as high-sensitivity optical characterization techniques. Especially, dark-field scattering spectroscopy combined with SEM imaging is a powerful tool for investigating the plasmonic properties in a single particle level. Later, various new plasmon models have been investigated. In 2003, Peter Nordlander studied the hybridization model for plasmon coupling.²³ Few years later, quantum plasmon resonances of individual metallic nanoparticles were experimentally observed in 2012.²⁴

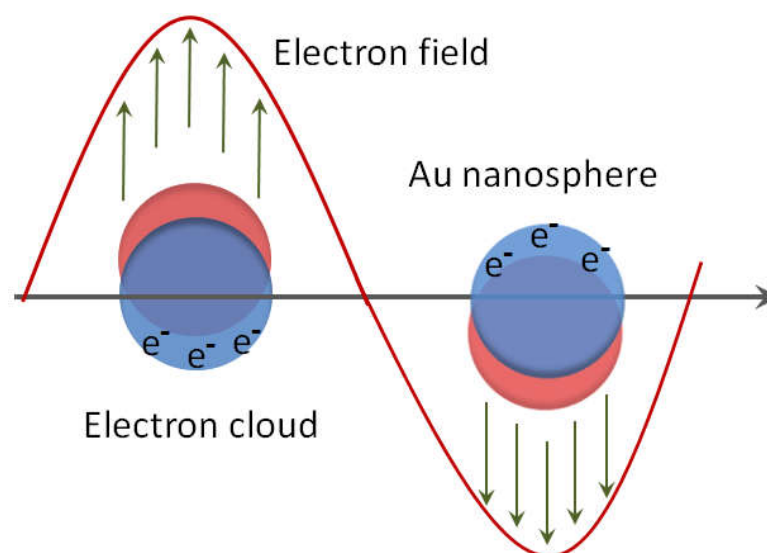


Figure 1.1 Collective oscillation of free electrons excited by incident electromagnetic field in an Au nanosphere.



LSPRs are collective and non-propagating oscillations of free electrons in the conduction band of noble metal nanostructures, as shown in Figure 1.1. Noble metal nanostructures are good candidates for supporting LSPRs because of the good chemical stability and high electric conductivity. It should be pointed out that there are some distinctive differences between the surface plasmon polaritons (SPP) and LSPRs. Compared with the propagating counterpart (SPP), LSPRs have a number of unique features. First of all, the localized nature of this resonance provides a way to a direct conversion of near-field energy into far-field radiation for detection and probing, and vice versa, to convert far-field signals into near-field ones for light focusing. Moreover, the LSPR supported by metallic NPs allows the excitation by incident light over a wide range of angles while SPP cannot be excited directly by the free-space light. It's because the SPP dispersion relation $\omega(k)$ lies below that of free-space light. Therefore, additional setups are necessary to overcome the momentum mismatches between the SPP and free-space light. Furthermore, the LSPR wavelengths of metal nanocrystals are closely related to their composition, size, and shape. As a result, LSPRs wavelengths can be facilely tuned over a wide range, from the ultraviolet to near-infrared region. In addition, excitation of LSPRs can extremely concentrate light into a nanoscale vicinity of metal nanostructures leading to a prominent enhancement of near-field. The greatly increased optical density of states enables strong light-matter interactions and enriches the plasmon-enhanced spectroscopy areas, plasmon-enhanced nonlinear effects and plasmon-driven catalytic reactions.²⁵⁻³⁰

Although the concept of surface plasmons was proposed many years ago, the history of exploiting optical properties of noble metal NPs may be traced back to the Roman times. The most representative example is the Lycurgus cup made of dichroic glass in 4th century A.D, which contains plenty of nano-sized Au-Ag alloy NPs (as shown in Figure 1.2).³¹ Interestingly, when the cup is illuminated from the outside, the scattered and reflected lights bring about green color. While when the illumination is

shone from the inside of the cup, the transmitted light leads to a red color. This is due to the Ag-Au alloy NPs contained in the cup which can absorb the light strongly with wavelengths near the green light.



Figure 1.2 Lycurgus cup, which looks green (left view) when it is illuminated from the outside, but red (right view) when illuminated from inside of the cup.³¹

1.3 Plasmonic Applications of Au NRs

The fast growth in colloidal chemistry preparation methods has facilitated the progress in the fields of the LSPRs. Unprecedented control over the composition, shape and size of noble metal nanocrystals can be easily achieved. Au and Ag nanocrystals with various morphologies and geometries can be fabricated with excellent control, such as nanorods, nanospheres, nanoprisms, nanocubes and nanobipyramids. Their sizes can be tuned from few to hundreds of nanometers. Because of the dependence of the LSPR wavelength on the shape and size, LSPR energies of these NRs can be tailored from the UV to near-infrared range.

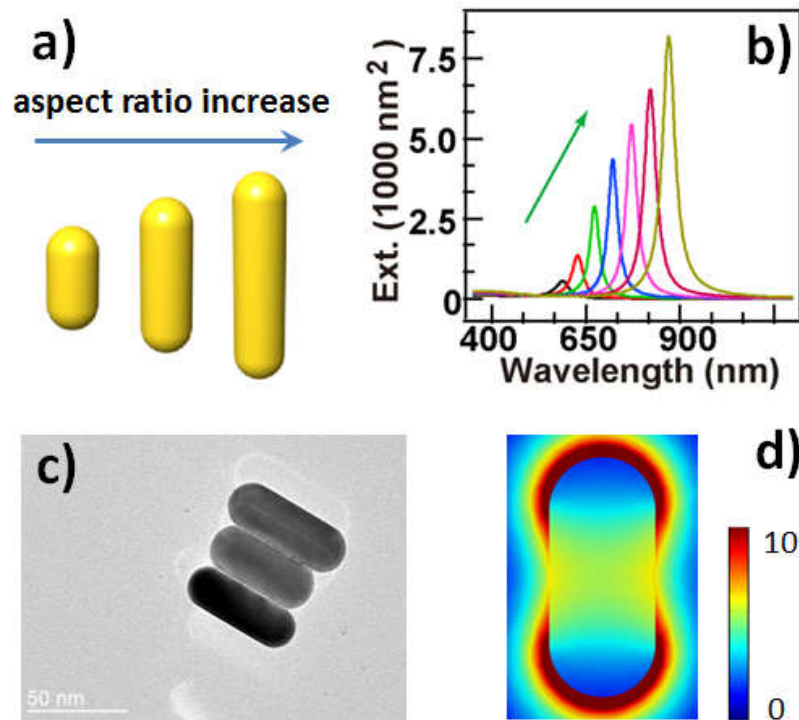


Figure 1.3 Dependence of the plasmonic properties of Au NRs on the aspect ratio. (a) Schematic showing Au NRs with a fixed diameter but different aspect ratios.³² (b) Simulated dependence of the extinction spectra on the aspect ratio. (c) TEM images of prepared Au NRs. (d) Electric field enhancement contour of an Au NR with an aspect ratio of 2.

Compared to other nanocrystals, Au NRs present significant advantages in tuning the LSPRs energies because Au NRs support two plasmon modes. One is longitudinal LSPR mode excited by the light polarized along the length direction, and the other is transverse LSPR mode associated with electron oscillations along the transverse axis of the NR. The plasmon wavelength of the longitudinal mode can be synthetically tuned across a broad spectral range from the visible to near-infrared wavelength regions by tailoring the aspect ratio. Au NRs can exhibit large electric near-field enhancement under resonant excitation. Such enhancement is basically located in the regions around the ends of the NRs. Furthermore, Au NRs can be integrated into plenty of bimetallic structures and heterostructures in different geometries, which resulting

in more complicated plasmonic properties due to the anisotropic nature of Au NRs (Figure 1.3 and 1.4).

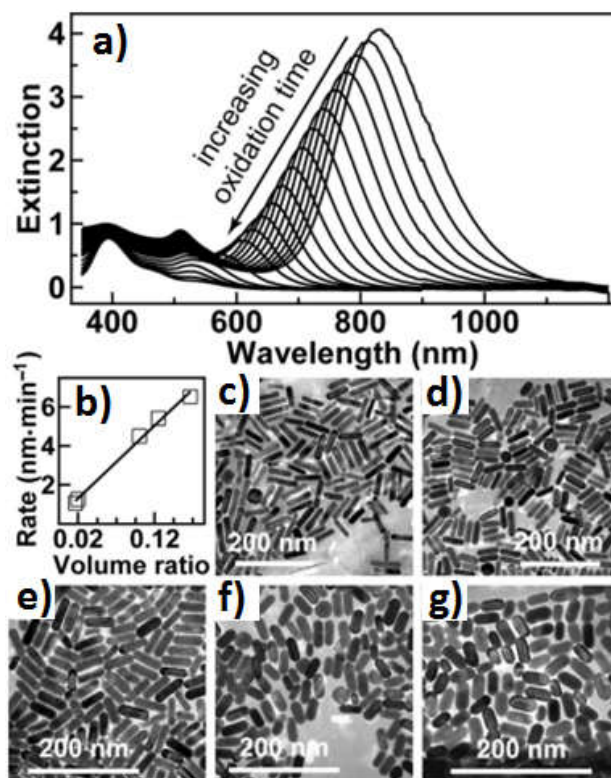


Figure 1.4 Tuning the LSPRs wavelengths of Au NRs. (a) Extinction spectra obtained at a fixed time interval after the addition of H₂O₂. (b) NR shortening rate versus the volume ratio between H₂O₂ and the NR solution. (c)-(g) TEM images of different shortened Au NRs.³²

1.3.1 Surface-enhanced Raman Scattering.

SERS can be seen as a representative example of the plasmonic applications of noble metal nanostructures. Because of its significance for clinical diagnosis and chemical analysis, massive efforts have been done to design and fabricate SERS substrates with large scattering cross section and strong Raman enhancements. In comparison with other nanostructures, Au NRs have become excellent SERS substrates due to strong electric field enhancements and effective tunability of the



LSPR in a wide spectral range to match the excitation wavelength. The SERS mechanism has been generally considered to involve the contributions from the electromagnetic field enhancement and the chemical enhancement, with the former being dominant for excitations which are in resonance with the LSPRs of metal nanostructures. Strong field enhancements located at the ends of Au NRs because of the high curvature. The field enhancements can be further improved when two NRs close to each other. The gap region between the NRs will form 'hot spots' with extremely large electromagnetic field and therefore can give unprecedented SERS signals. The smaller SERS signal corresponding to the hot spot creation is ascribed to the mismatch between the laser excitation wavelength and the plasmon resonance (Figure 1.5c).³³

The representative STEM images and optical properties of the self-assembled chains of Au NRs in Figure 1.5 confirm dynamic generation of hot-spots between neighboring assembled Au NRs. The authors established a direct correlation between ensemble-averaged SERS and extinction properties of the chains. The established relationship between the structure of NR ensembles and their optical properties provides the basis for creating plasmonic platforms that can be utilized in applications ranging from sensing to nanoelectronics.

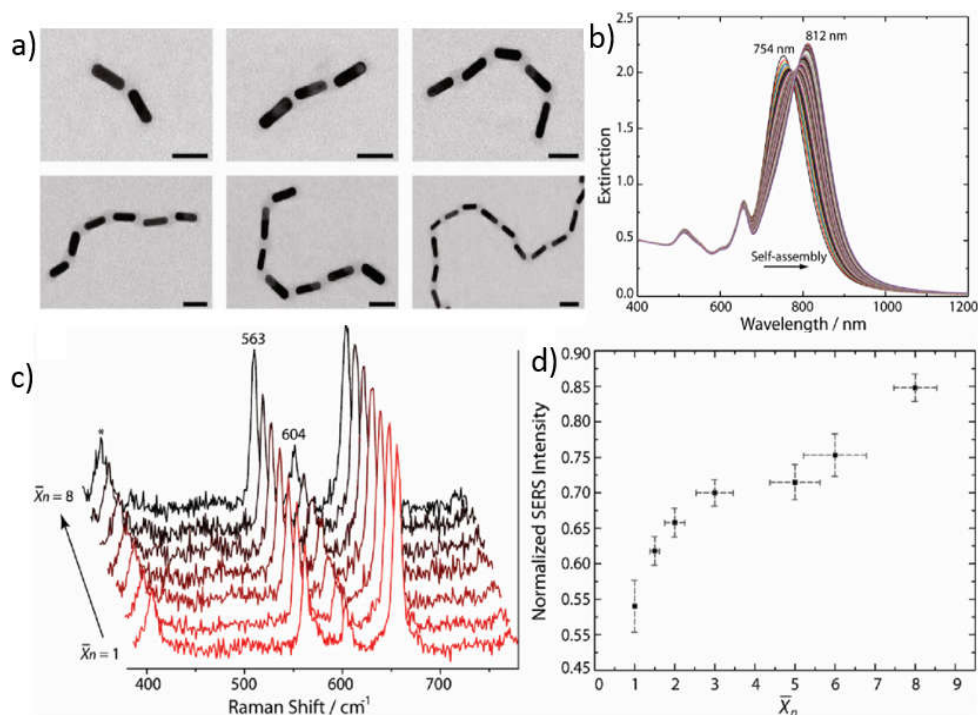


Figure 1.5 (a) TEM images and (b) extinction properties of the self-assembled NRs. (c) Evolution of normalized ensemble-averaged SERS spectra in self-assembled NR chains. (d) Variation in the normalized SERS peak intensity measured at 563 cm⁻¹ plotted as a function of the average aggregation number of the NR chains.³³

1.3.2 Photothermal Therapy

Light-activated therapy could be used to deracinate the diseased cells in a safe manner. Much attention has been focused on the emerging potential of photothermolysis, which involves the conversion of absorbed light into heat via non-radiative mechanisms. Photo-activated effects can be localized and intensified by employing exogenous agents with large absorption cross sections, confining damage to areas of interest with minimal collateral effects. In particular, targeted photothermolysis may be most effective when mediated by photothermal agents that absorb strongly at near-infrared (NIR) frequencies and thus enable deeper penetration into biological tissues. For example, Tong investigated the mechanisms and extent of photothermal injury inflicted by Au NRs targeted to cell-surface receptors.³⁴ Folate-

conjugated Au NRs (F-NRs) were monitored in real time by TPL microscopy, and were observed to be particularly effective at inducing tumor cell necrosis when localized on the cell membrane. As shown in Figure 1.6, the mechanistic insights in this study reveal the photothermal activity of Au NRs.

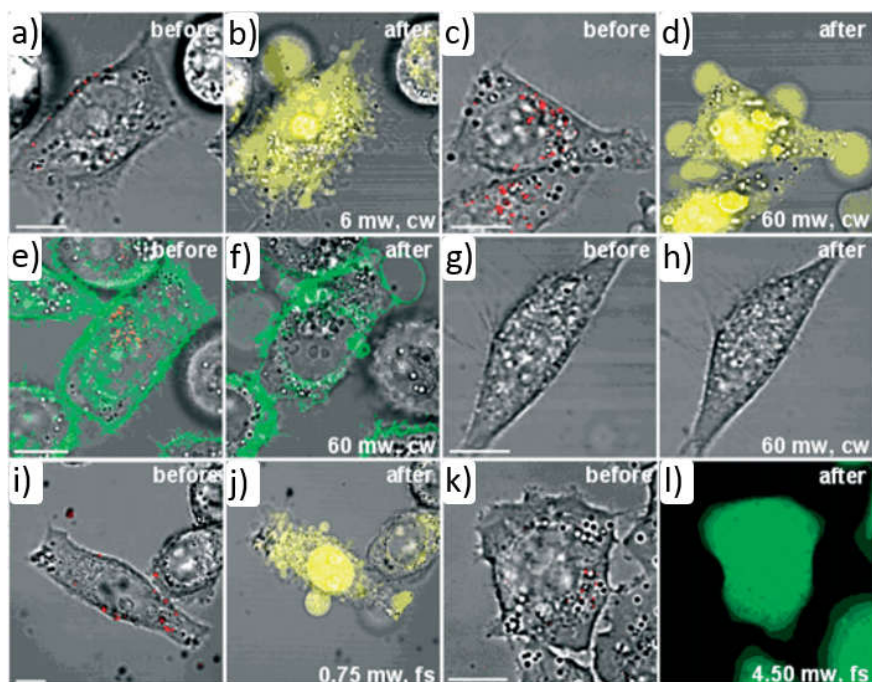


Figure 1.6 Site-dependent photothermolysis mediated by F-NRs (red). (a,b) Cells with membrane-bound F-NRs exposed to cw NIR laser irradiation. (c,d) Cells with internalized F-NRs required 60 mW to produce a similar level of response. (e,f) F-NRs internalized in KB cells labeled by folate-Bodipy (green) were exposed to laser irradiation at 60 mW, resulting in both membrane blebbing and disappearance (melting) of the F-NRs. (g,h) NIH-3T3 cells were unresponsive to F-NRs, and did not suffer photoinduced damage upon 60 mW laser irradiation. (i,j) Cells with membrane-bound F-NRs exposed to fs-pulsed laser irradiation produced membrane blebbing at 0.75 mW. (k,l) Cells with internalized F-NRs remained viable after fs-pulsed irradiation at 4.50 mW, as indicated by a strong calcein signal (green).³⁴

1.3.3 Plasmonic Nanoantennas

Plasmonic metal nanostructures, which possess strong light absorption/scattering capabilities and relatively narrow linewidths, can act as nanoantennas and thereby open up the possibilities for controlling and manipulating light-matter interactions at the nanoscale. Plasmonic nanostructures, as nanoantennas, can function as a transducer between far- and near-field light signals. Free-space radiation can be captured by a plasmonic antenna and transferred to a nanoscale object. The capture of light by plasmonic nanoantennas causes strongly confined electromagnetic fields around them, which can not only enhance the optical transitions of adjacent nano-objects, but also allow for nanoscale optical signal processing.

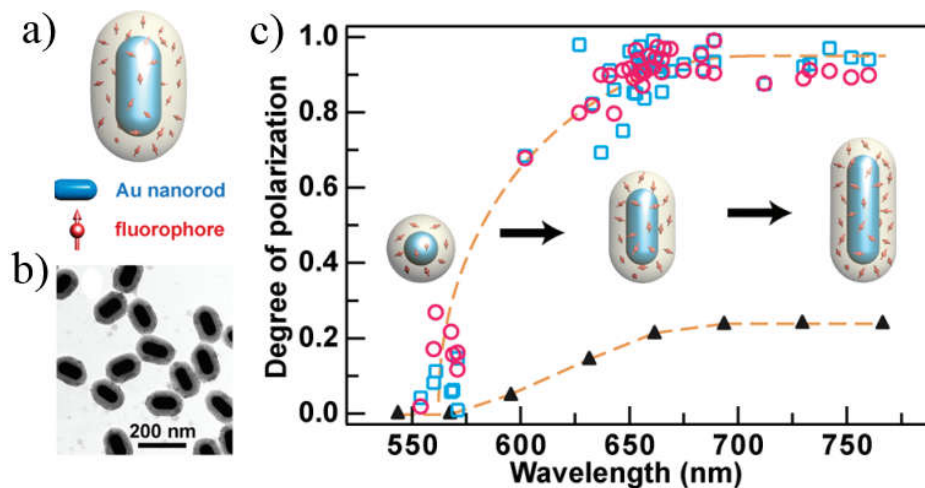


Figure 1.7 Emission and scattering polarization of the Au nanorod-fluorophore hybrid nanostructures: (a) schematic showing a single hybrid nanostructure; (b) TEM image of a representative nanostructure sample; (c) Degree of polarizations (DOPs) of the scattering (blue squares) and fluorescence emission (red circles) from the hybrid nanostructure vs the LSPR wavelength. The black solid triangles are the calculated DOPs of the plasmon-enhanced excitation electric field intensity. The dashed curves are guides for the eyes.³⁵



Wang and his group demonstrated that the interactions of the plasmon resonance of the NR with the excitation and emission processes of the fluorophores were temporally separated under unsaturated excitation conditions.³⁵ The emission polarization was found through electrodynamic calculations to arise from the plasmon-coupled emission instead of the plasmon-enhanced excitation polarization. The emission carries direction and polarization properties that are essentially determined by the dipolar plasmon of the NR antenna. The result provided direct and concrete evidence that has been proposed recently for plasmon-enhanced fluorescence.

1.3.4 Plasmon-enhanced Circular Dichroism

Optical circular dichroism (CD), originating from the chirality of molecules, is an intriguing phenomenon of biomolecules. CD signals are usually employed to detect biological species with chiralities as well as their conformational changes. In this sense, the accuracy of CD spectroscopy relies on the intensity of CD signals. In recent years, the plasmon resonance of metal nanostructures has been found to be able to enhance the electronic transition of adjacent chiral molecules and thus enhance their CD signals. These findings have opened up new opportunities for traditional CD spectroscopy and brought up a new research branch in this plasmonic CD spectroscopy area. Most of the previous studies have mainly focused on plasmonic CD signals induced by isolated metal nanocrystals. In view of future applications that require ultrasensitive detection, the use of the plasmon coupling in nanocrystal assemblies to enhance CD signals is highly desired. Tang and his group reported the optical activity in the templateless 1D assembly of cysteine (Cys) and Au NRs (Figure 1.8).³⁶ CD response can be manipulated in both intensity and wavelength in the range from 500 nm to more than 900 nm by tuning the aspect ratio of the Au NRs. Individual Cys-attached Au NRs and Cys-assembled Au NPs substantiate that the form of assembly and the shape of building blocks are significant not only for the intensity but for the line shape of the CD signals as well.

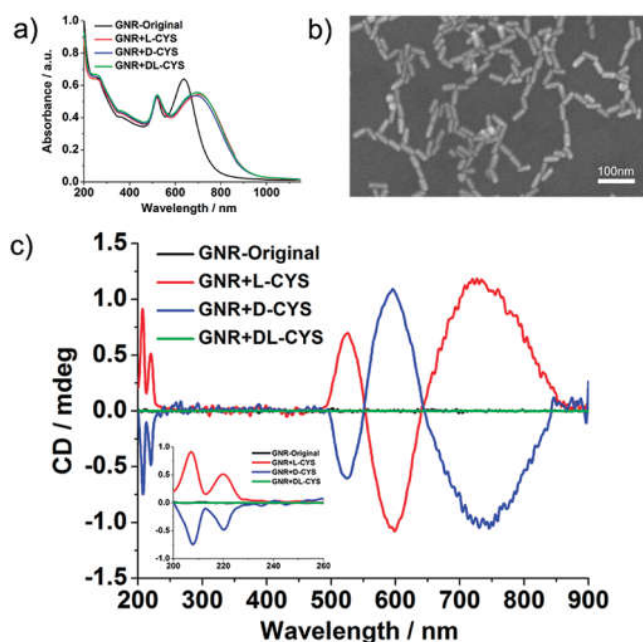


Figure 1.8 (a) UV-vis-NIR spectra of the original Au NRs and 1D self-assembled Au NRs formed by three types of Cys; (b) SEM image of the 1D self-assembled Au NRs; (c) CD spectra of original Au NRs and assembled Au NRs by different Cys.³⁶

1.3.5 Plasmon-assisted Photochemical Reactions

The plasmon resonances of metal nanostructures, owing to their strong light absorption capabilities, can provide benefits for various photochemical reactions. Plasmon-enhanced photochemical reactions can be achieved by integrating metal nanocrystals with traditional photocatalysts, such as TiO_2 and iron oxides. On the one hand, the strong near field around metal nanocrystals under resonant excitation can accelerate the generation of electron-hole pairs in the adjacent semiconductors, whereby the related photochemical reactions can be enhanced. On the other hand, the reaction environment around metal nanocrystals can be heated up due to the plasmonic photothermal conversion. In addition, the collective electron oscillations associated with the plasmon resonance can decay into hot electrons through Landau damping. These energetic electrons can thereafter participate in the reaction processes. These

two photothermally related effects are important driving forces for enhancing photochemical reactions. In recent years, plasmon-assisted photochemical reactions have attracted much attention due to their great prospects in highly efficient utilization of solar energy, which is a promising solution to the worldwide energy crisis.

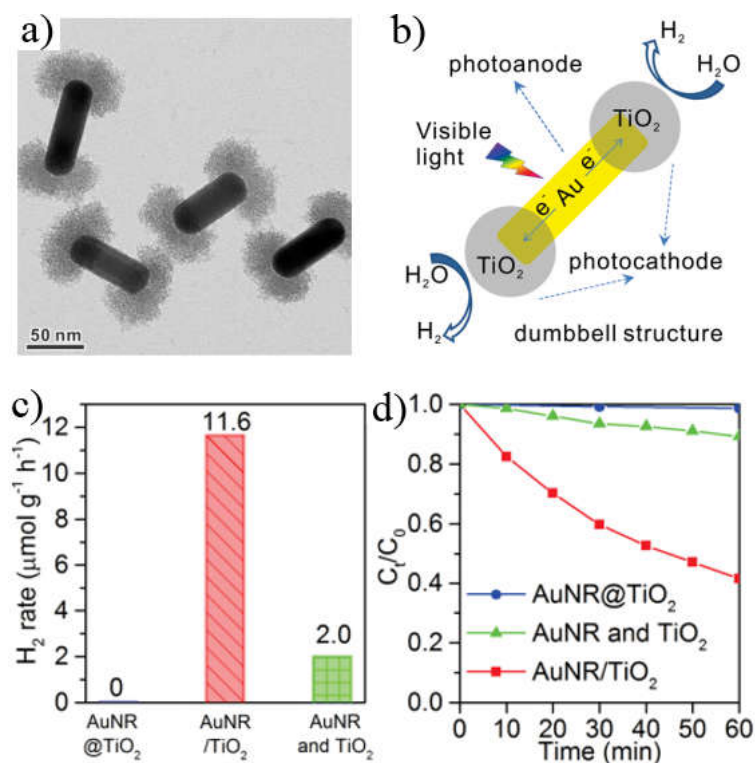


Figure 1.9 (a) TEM image of Au NR/TiO₂ nanodumbbell. (b) Structure and mechanism of operation under visible light of an individual Au NR/TiO₂ dumbbell. Comparison of (c) H₂ evolution rate by various catalysts, and (d) normalized concentration of methylene blue vs irradiation time; both under visible illumination and in the presence of methanol and water.³⁷

For example, recently, Wu reported a wet-chemistry method for the anisotropic overgrowth of TiO₂ on Au NRs structure, which satisfies the electron refilling requirement and exhibits plasmon-enhanced hydrogen production from water reduction under visible and NIR light irradiation. The created Au NR/TiO₂ interface with the Au NR side exposed serves as a Schottky junction that can filter out SPR hot electrons from the Au NRs. This work demonstrated an alternative way to achieve



anisotropic TiO₂ overgrowth chemically rather than by nanofabrication techniques, and is expected to be a promising platform for the development of free-standing functional photocatalysts (Figure 1.9).³⁷

1.4 Motivation of the Thesis Work

Au NRs have been receiving extensive attention owing to their extremely attractive applications in biomedical technologies, plasmon-enhanced spectroscopies and optoelectronic devices. The growth methods and plasmonic properties of Au NRs, as well as their complex nanostructures have been intensively studied. Au NRs present many outstanding physical and chemical properties. Therefore, it is very important to utilize the superior properties of Au NRs to resolve the existing challenges and problems, for example:

a) Monitoring of catalytic reactions by SERS spectroscopy. As far as we know, controlling the surface coverage of catalytic NPs on Au NRs core such that a balance between SERS enhancement and catalytic efficiency can be achieved but due to the fact that large coating of catalytic metals on a plasmonic NP significantly degrade its near-field enhancement it has not been fully investigated before.

b) Interband absorption enhanced optical activity. Previous studies seldom reported the use of interband transitions in noble metals because of their high energy levels located in the UV region. However, considering significant matching of their resonance energies, the interband transitions of noble metals could accelerate the electronic transitions of adhered chiral molecules and thus amplify the absorption difference of circularly polarized light by the molecules.

c) Asymmetrically anisotropic Au NR-based heterocatalysts. Sufficient photoexcited carrier separation and transfer are the main two processes that allow efficient photocatalytic water splitting. Anisotropic junction may provide multichannel separation of the photoexcited charges to effectively inhibit the carrier



recombination and facilitate the electron transfer. Although many efforts have been made in the past few years to improve the photocatalytic efficiency, engineering asymmetrically anisotropic heterocatalysts is still a considerable challenge and is rarely reported to date. In this thesis, the above mentioned issues will be discussed and studied.

1.5 Outline of the Thesis

The chapters of the thesis are organized as follows:

Chapter 1: Introduction. In this chapter, light-matter interaction concept is first introduced, followed by the SPP and LSPR. Then, the preparation, properties and various plasmonic applications of Au NRs are presented. Then, the significance of the thesis is illustrated and its overall structure is presented at the end.

In Chapter 2, the optical and morphological characterization methods, instruments used in experimental part, as well as the simulation method performed in the work are briefly introduced.

In Chapter 3, it is demonstrated, that the dual functionalities allowing catalysis and SERS of the Au/Pt hybrid structure can be tailored by adjusting the decoration density of Pt NPs on the surface of Au NRs, and a balance between them can be achieved at an optimal surface density. Then the optimized hybrid nanostructure has been used as a sensitive probe to monitor the catalytic reaction processes *in situ*.

In Chapter 4, it is demonstrated that an individual Au@Ag CSNC can serve as a plasmonic reporter of an extended helical network formed among chemisorbed cysteine molecules, through generating an interband absorption enhanced, Ag-surface-exclusive CD band in the UV region.

In Chapter 5, the synthesis of an anisotropic heterophotocatalyst is described where the Au NRs coated by 2-5 nm-Pt NPs are well deposited on the surface of C₃N₄ nanosheets. It was demonstrated that the optical antenna effect of Au NRs can be used



to directly enhance light absorption, consequently accelerating the light-matter interaction and improving the H₂ productivity.

Finally, conclusions and future work are presented in Chapter 6.

References

- 1 K. M. Mayer, J. K. Hafner, *Chem. Rev.*, 2011, **111**, 3828.
- 2 G. Peng, U. Tisch, O. Adams, M. Hakim, N. Shehada, Y. Y. Broza, S. Billan, R. Abdah-Bortnyak, A. Kuten, H. Haick, *Nat. Nanotechnol.*, 2009, **4**, 669.
- 3 E. M. Larsson, C. Langhammer, I. Zoric, B. Kasemo, *Science*, 2009, **326**, 1091.
- 4 D.-K. Lim, K.-S. Jeon, H. M. Kim, J.-M. Nam, Y. D. Suh, *Nat. Mater.*, 2010, **9**, 60.
- 5 X. Huang, S. Neretina, M. A. El-Sayed, *Adv. Mater.*, 2009, **21**, 4880.
- 6 R. Bardhan, A. Lal, A. Joshi, N. J. Halas, *Acc. Chem. Res.*, 2011, **44**, 936.
- 7 N. J. Halas, S. Lal, W.-S. Chang, S. Link, P. Nordlander, *Chem. Rev.*, 2011, **111**, 3913.
- 8 M. Pelton, J. E. Sader, J. Burgin, M. Z. Liu, P. Guyot-Sionnest, D. Gosztola, *Nat. Nanotechnol.*, 2009, **4**, 492.
- 9 J. A. Fan, C. Wu, K. Bao, J. Bao, R. Bardhan, N. J. Halas, V. N. Manoharan, P. Nordlander, G. Shvets, F. Capasso, *Science*, 2010, **328**, 1135.
- 10 J. T. Choy, J. M. Hausmann, T. M. Babinec, I. Bulu, M. Khan, P. Maletinsky, A. Yacoby, M. Loncar, *Nat. Photonics*, 2011, **5**, 738.
- 11 T. Schumacher, K. Kratzer, D. Molnar, M. Hentschel, H. Giessen, M. Lippitz, *Nat. Commun.*, 2011, **2**, 333.
- 12 V. Giannini, A. I. Fernandez-Dominguez, S. C. Heck, S. A. Maier, *Chem. Rev.*, 2011, **111**, 3888.
- 13 P. Zijlstra, J. W. M. Chon, M. Gu, *Nature*, 2009, **459**, 410.
- 14 F. M. Wang, N. A. Melosh, *Nano Lett.*, 2011, **11**, 5426.
- 15 H. A. Atwater, A. Polman, *Nat. Mater.*, 2010, **9**, 205.
- 16 P. Christopher, H. L. Xin, S. Linic, *Nat. Chem.*, 2011, **3**, 467.



- 17 S. Linic, P. Christopher, D. B. Ingram, *Nat. Mater.*, 2011, **10**, 911
- 18 R. W. Wood, *Phil. Mag.*, 1902, **4**, 396
- 19 G. Mie, *Ann. der Physik*, 1908, **25**, 377
- 20 U. Fano, *J. Opt. Soc. Am.*, 1941, **31**, 213
- 21 R. H. Ritchie, *Phys. Rev.*, 1957, **106**, 874.
- 22 A. Z. Otto, *Physik*, 1968, **216**, 398.
- 23 E. Prodan C. Radloff, N. J. Halas, P. Nordlander. *Science*, 2003, **17**,419.
- 24 A. Jonathan, A. L. K. Scholl, A. D. Jennifer, 2012, *Nature*, **483**, 421.
- 25 P. Berini, I. De-Leon, *Nat. Photonics*, 2011, **6**, 16.
- 26 S. Kim, J. Jin, Y.-J. Kim, I.-Y. Park, Y. Kim, S.-W. Kim, *Nature*, 2008, **453**, 757.
- 27 M. W. Klein, C. Enkrich, M. Wegener, S. Linden, *Science*, 2006, **313**, 502.
- 28 D.-K. Lim, K.-S. Jeon, H. M. Kim, J.-M. Nam, Y. D. Suh, *Nat. Mater.*, 2010, **9**, 60.
- 29 S. Schietinger, T. Aichele, H.-Q. Wang, T. Nann, O. Benson, *Nano Lett.*, 2010, **10**, 134.
- 30 T. Ming, H. J. Chen, R. B. Jiang, Q. Li, J. Wang, *J. Phys. Chem. Lett.*, 2012, **3**, 191.
- 31 www.dreamsofglass.com/dichronic-glass-info.html.
- 32 H. J. Chen, L. Shao, Q. Li, J. F. Wang, *Chem. Soc. Rev.*, 2013, **42**, 2679.
- 33 L. Anna, A. F. S. Gustavo, A. Aftab, L. S. Michele, C. Neil, T. Ethan, L. Kun, G. Reuven, G. B. Alexandre, and K. Eugenia, *J. Am. Chem. Soc.*, 2011, **133**, 7563.
- 34 L. Tong, Y. Zhao, T. B. Huff, M. N. Hansen, A. Wei, and J.-X. Cheng, *Adv. Mater.*, 2007, **19**, 3136.
- 35 T. Ming, L. Zhao, H. Chen, K. C. Woo, J. Wang, and H.-Q. Lin, *Nano Lett.*, 2011, **11**, 2296.
- 36 Z. Zhu, W. Liu, Z. Li, B. Han, Y. Zhou, Y. Gao, and Z. Tang, *ACS Nano*, 2012, **6**, 2326.
- 37 B. Wu, D. Liu, S. Mubeen, T. T. Chuong, M. Moskovits, and G. D. Stucky, *J. Am. Chem. Soc.*, 2016, **138**, 1114.

Chapter 2 Experimental Instruments, Sample Preparations, Theory and Simulations

In this chapter, I will briefly show the characterization instruments and the calculation method employed in my work.

2.1 Sample Preparations

Chemicals

Tetrachloroauric (III) acid (HAuCl_4), cetyltrimethylammonium bromide (CTAB), silver nitrate (AgNO_3), hexachloroplatinic (IV) acid (H_2PtCl_6), ascorbic acid (AA), 4-nitrothiophenol, 4-aminothiophenol, cetyltrimethylammonium chloride (CTAC), L/D-cysteine, Poly(styrenesulfonate) (PSS) of average $M_w \sim 70,000$, trisodium citrate, sodium hydroxide (NaOH) and sodium borohydride (NaBH_4) were purchased from Sigma and all chemicals were used without further purification. Ultrapure water was used for all experiments.

Synthesis of Au nanorods

The starting Au NRs were grown according to previous seed-mediated method. Specifically, the seed solution was prepared by mixing HAuCl_4 (0.01 M, 0.25 mL) and CTAB (0.1 M, 9.75 mL) in a 15 mL plastic tube. An ice-cold NaBH_4 solution (0.01 M, 0.6 mL) was then injected quickly into the mixture solution followed by rapid inversion for 1 min. The seed solution was kept at room temperature for at least 2 h before use. To grow Au NRs, HAuCl_4 (0.01 M, 2.0 mL) and AgNO_3 (0.01 M, 0.4 mL) were mixed with CTAB (0.1 M, 40 mL) in a 50 mL plastic tube. HCl (1.0 M, 0.8 mL)



was then added to adjust the pH of the solution to 1-2, followed by the addition of AA (0.1 M, 0.32 mL). Finally, the seed solution (10 μ L) was injected into the growth solution. The solution was gently mixed for 20 s and left undisturbed at room temperature for at least 6 h before use. Then the Au NRs were centrifuged two times and redispersed in water. With the purpose of tailoring the surface plasmon resonance to match the excitation laser wavelength at 633 nm in SERS measurements, the starting Au NRs were oxidized by adding a certain amount of HAuCl₄ (0.01 M), and the longitudinal plasmon wavelength was therefore tailored to around 633 nm. Due to the oxidation of the added Au⁺, the Au NR can be oxidized anisotropically. The oxidation often takes place at the ends more quickly than at the side. Therefore, the aspect ratio of the Au NR becomes smaller and the plasmon wavelength shifts blue.

Synthesis of Au@Ag core-shell nanocuboids

The Au@Ag core-shell nanocuboids were prepared according to a reported procedure. Briefly, the Au NRs solution of 2 mL was centrifuged and re-dispersed into 2 mL aqueous CTAC solution (0.08 M). The AgNO₃ solution (0.4 mL, 0.01 M) was subsequently added into the Au nanorod solution followed by adding 0.2 mL AA solution (0.1 M). The resultant solution was kept in an isothermal oven at 65 °C for 4.5 h to produce Au@Ag core-shell nanocuboids.

Synthesis of Au nanospheres

CTAC-capped Au nanospheres were synthesized by using a modified seed-mediated growth method. Au seeds were synthesized by adding 0.6 mL ice-cold sodium borohydride solution (10 mM) into a solution containing 0.25 mL HAuCl₄ (10 mM) and 9.75 mL CTAB (0.1 M) under vigorous stirring at room temperature. The color of the seed solution changed from yellow to brown. Seed solution was kept undisturbed at room temperature for 3 h. Growth solution was prepared by mixing 6 mL HAuCl₄ (0.5 mM) and 6 mL CTAC (0.2 M) under stirring followed by adding 4.5 mL ascorbic



acid (AA, 0.1 M). Subsequently, 0.3 mL Au seed solution was added to the growth solution. Au nanospheres were centrifuged and redispersed in DI water for further use.

Synthesis of Ag nanospheres

CTAB-capped Ag nanoparticles were prepared by a one-step reaction in an ethanol/water system. In brief, 2 mL of CTAB ethanol solution (1 mM) was mixed with 30 mL of AgNO₃ (5 mM) under vigorous stirring. After 10 min, freshly prepared aqueous NaBH₄ (1%) was added to the mixed solution until the color of the colloids changed to yellow-green and the color did not change when more NaBH₄ was added.

Synthesis of Ag nanorods

Ag nanorods were prepared by a two-step method. Preparation of Ag nanoseed: a 20 mL solution with a final concentration of 0.25 mM AgNO₃ and 0.25 mM trisodium citrate in water was prepared. While stirring vigorously, 0.6 mL of 10 mM NaBH₄ was added at once. Stirring was stopped after 30 s. Procedure for Ag rods: first, 6 sets of solutions were prepared containing 0.25 mL of 10 mM AgNO₃, 0.50 mL of 100 mM ascorbic acid, and 10 mL of 80 mM CTAB. Next, 2 mL amount of Ag nanoseed solution was added. Finally, 0.10 mL of 1M NaOH was added to each set. After the reaction finished, the Ag nanorods were centrifugated twice for further use.

2.2 Characterization methods

Nanoparticle structure, optical and SERS are characterized. Details of the method include:

UV-Vis and FT-IR spectrophotometer

The extinction spectra of the samples were obtained with a UV-visible spectrometer (Shimadzu Scientific Instruments, UV2550). In this study, the UV-Vis



spectrophotometer was employed to measure the absorption spectra of Au NRs in solutions and determine their LSPR wavelengths. The longitudinal LSPR wavelength undergoes a blue shift when the aspect ratio of Au NRs decreases. Moreover, the concentration of Au NRs was estimated based on the Beer-Lambert law.

The FT-IR measurements were performed on Thermo Scientific (Nicolet 380) at 298 K.

Circular dichroism spectroscopy

CD only occurs at wavelengths of light that can be absorbed by a chiral molecule. At these wavelengths left- and right-circularly polarized light will be absorbed to different extents. CD measured as a function of wavelength is termed CD spectroscopy. The CD spectra of L/D-cysteine and other colloid samples were measured with a commercially available CD spectrometer (JASCO, J-810). The samples at appropriate concentrations were loaded in 5-mm-thick quartz cells for recording their CD spectra as a function of reaction time, temperature, pH value and added ion concentration.

Transmission electron microscopy

The as-prepared metal nanostructures were drop-cast on a TEM grid to perform high-resolution morphological characterization and EDX element mapping (JEM2100F TEM system operating at 200 kV).

Raman spectroscopy

The Raman spectra of the samples were recorded by using a commercial Raman spectrometer (HORIBA HR800) with excitation laser wavelength at 488 nm ($\sim 2 \mu\text{m}$ diameter and 0.1 mW output) and signal integration time of 5 sec. The excitation light and the scattering light were focused to and collected from the samples respectively



by the same long-working distance objective (W.D. 3.18 mm, NA 0.7, Mag. 60×).

Nuclear magnetic resonance imaging

The ^1H NMR measurements for L-cysteine and L-cysteine-functionalized Au@Ag CSNCs dispersions have been performed on Bruker Advance-III, 600 MHz FT-NMR system at 298 K. The spectra were acquired with the D₂O solvent.

X-ray diffractometer

The crystal structures of the samples were investigated by an X-ray diffractometer (XRD, Rigaku Smart LabX XRD-6000) (Cu K α radiation, $\lambda=1.54056 \text{ \AA}$, accelerating voltage of 45 kV and current of 200 mA).

X-ray photoelectron spectroscopy

X-ray photoelectron spectroscopy (XPS) measurements of the samples were carried out on a VG ESCALAB MKII instrument at a pressure greater than 10^{-6} Pa. The general scan and Au4f, Pt4f, C1s, and N1s spectra were recorded with unmonochromatized Al K α radiation.

2.3 Theory and Simulation

Here I will give an overview of the theoretical background of the LSPRs in noble metal nanocrystals. It is known that the optical responses of metallic structures are fully determined by the dielectric properties of the metal and the dielectric, the properties of the excitation light, as well as the boundary conditions of the interfaces. Surface plasmons (SPs) are described as coherent delocalized electron oscillations that exist at the interface between any two materials, such as metal and air.¹ In classical



electromagnetic theories, SPs are surface electromagnetic waves confined at metal-dielectric interfaces. From the basis of Maxwell's equations, the interaction of metals with electromagnetic fields can be understood in a classical framework.² In this chapter, I will briefly introduce Maxwell's equations and the electrodynamic theory for calculating the optical response of metal NPs.³ Besides, I will discuss the numerical methods for calculating the plasmonic properties of metal nanostructures, especially the finite-difference time-domain (FDTD) method used in this thesis.

2.3.1 Theoretical Background

Maxwell's equations are the basis for stating the electrodynamic processes in macroscopic systems where quantum effects are negligible. Typically, Maxwell's equations can be written as following:

$$\nabla \times \mathbf{E} = -\frac{\partial \mathbf{B}}{\partial t} \quad (2.1)$$

$$\nabla \times \mathbf{H} = \mathbf{J}_f + \frac{\partial \mathbf{D}}{\partial t} \quad (2.2)$$

$$\nabla \cdot \mathbf{D} = \rho_f \quad (2.3)$$

$$\nabla \cdot \mathbf{B} = 0 \quad (2.4)$$

where ρ_f and \mathbf{J}_f are free charge density and free current density, respectively. From the above four partial differential equations it can be found the electric field \mathbf{E} and the magnetic field \mathbf{B} are related closely with each other. In the case of the interaction between light and noble metal NPs, the free charges and current densities $\rho_f = 0$ and $\mathbf{J}_f = 0$. The electric displacement \mathbf{D} and the magnetizing field \mathbf{H} are determined by the polarization and magnetization properties of the system

$$\mathbf{D} = \epsilon_0 \mathbf{E} + \mathbf{P} \quad (2.5)$$

$$\mathbf{B} = \mu_0 \mathbf{H} + \mathbf{M} \quad (2.6)$$



where P (polarization) and M (magnetization) are defined as the electric dipole moment and the magnetic dipole moment per unit volume, respectively. ϵ_0 and μ_0 are the permittivity and permeability of vacuum, respectively. If the response of the system is linear, then P and M can be written as

$$P = \epsilon_0 x_e E \quad (2.7)$$

$$M = \mu_0 x_M H \quad (2.8)$$

in which x_e represents the dielectric susceptibility and describes the linear relationship between P and E . x_M means the magnetic susceptibility, describing the linear relationship between M and H . For the isotropic and nonmagnetic media, therefore equations (2.5) and (2.6) turn into

$$D = \epsilon_0 E + P = (1 + x_e)\epsilon_0 E \quad (2.9)$$

$$B = \mu_0 H + M = (1 + x_M)\mu_0 H \quad (2.10)$$

We define ϵ_r and μ_r represent the relative permittivity and permeability, respectively. They can be described as

$$\epsilon_r = 1 + x_e \quad (2.11)$$

$$\mu_r = 1 + x_M \quad (2.12)$$

From equations (2.1), (2.2), (2.9), (2.10), (2.11) and (2.12) we can obtain the following equations describing the electromagnetic waves propagating in a linear media.

$$\nabla(\nabla \cdot E(r, t)) - \nabla^2 E(r, t) + \mu_0 \frac{\partial}{\partial t} [\nabla \times \mu_r(r) H(r, t)] = 0 \quad (2.13)$$

$$\nabla(\nabla \cdot H(r, t)) - \nabla^2 H(r, t) + \epsilon_0 \frac{\partial}{\partial t} [\nabla \times \epsilon_r(r) E(r, t)] = 0 \quad (2.14)$$

In the case of given the initial conditions, the boundary conditions, as well as the spatially dependent $\epsilon_r(r)$ and $\mu_r(r)$, the electric and magnetic components of the electromagnetic wave in the system therefore can be determined by solving equations (2.13) and (2.14).



2.3.2 Finite-difference Time-domain (FDTD) Simulation

Method

There are two main types of numerical methods for electrodynamic calculations. One is discrete dipole approximation (DDA) which is carried out in frequency domain. The other is FDTD carried out in both the time domain and the frequency domain.

FDTD method was first developed by Yee in 1966⁴ and has being regarded as the most widely used numerical method. FDTD is a time-marching method in this which the key is how to replace all the derivatives in Maxwell's equations with finite discrete grids, the Yee cells. A Yee cell shown in Figure 2.1, is the basic element of an interlocked grid in which E and H are shifted by half-grid points relative to each other. As interpreted in the Figure, (i, j, k) represents a specific grid point in the space. The offsets between E and H both in space and time are used to generate the accurate derivatives. For example, if the time delay is A_t , the one-dimensional discrete form of Maxwell's equations can be expressed as

$$E_x^{n+\frac{1}{2}}\left(k+\frac{1}{2}\right)=E_x^{n-\frac{1}{2}}\left(k+\frac{1}{2}\right)-\frac{\Delta t}{\Delta z \varepsilon\left(k+\frac{1}{2}\right)}\left[H_y^n(k+1)-H_y^n(k)\right] \quad (2.15)$$

$$H_y^{n+1}(k)=H_y^n(k)-\frac{\Delta t}{\Delta z \mu(k)}\left[E_x^{n+\frac{1}{2}}\left(k+\frac{1}{2}\right)-E_x^{n+\frac{1}{2}}\left(k-\frac{1}{2}\right)\right] \quad (2.16)$$

in which k is the spatial coordinate and n represents the time. The distributions of E and H at each time step can be obtained by solving (2.15) and (2.16) equations. The frequency-related properties, for example, scattering and absorption cross sections as well as far- and near-field distributions, can be further calculated via Fourier transform.

5,6

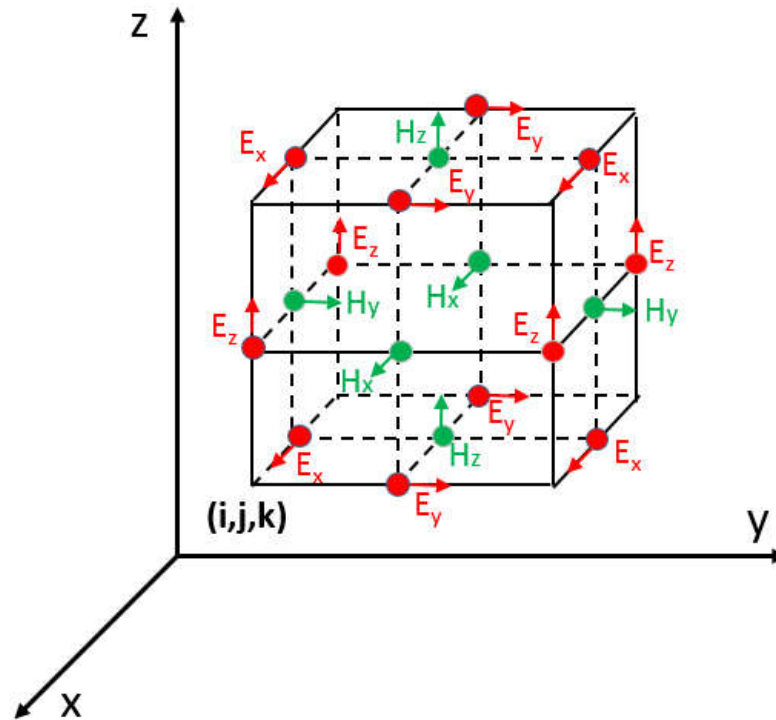


Figure 2.1 Schematic showing a Yee cell used in FDTD simulations.⁴

It needs to point out that in practical simulations, calculations cannot be performed over an infinite space. FDTD uses a perfectly matched layer technique to model the propagation of electromagnetic waves into the infinite space. To be special, the perfectly matched layer technique needs to place a boundary around the simulated target. The electromagnetic energies are almost completely absorbed by this boundary in case of the electromagnetic wave is incident on. The method has successfully been applied to many nanosystems seen in several well-known literatures.^{7,8} The FDTD method has several advantages. Firstly, it is fully explicit and employs no linear algebra, which can significantly reduce the computational overhead needed to solve a particular problem. Besides, it is based on the time domain, and thereby the calculation produces a full spectrum with a single run. Moreover, the time-marching aspect of this algorithm enables the observation of the electromagnetic field distribution at any time of the simulation. Last but not least, the discretization-based algorithm is easy to achieve parallel simulation on different computers, which facilitates the calculation of



large and complex objects. Every coin has two sides. The accuracy of the FDTD calculations depends on the setting of the grid size and the time step. Setting smaller grid sizes and time steps can usually bring more accurate results, but needs higher equipment demands and would be very time-consuming.

References

- 1 [https://en.wikipedia.org/wiki/Surface plasmon](https://en.wikipedia.org/wiki/Surface_plasmon).
- 2 S. A. Maier, *Plasmonics: Fundamentals and Applications*. Springer Science+Business Media LLC, **2007**.
- 3 Jackson, J. D. *Classical Electrodynamics*. John Wiley & Sons, Inc., 1962.
- 4 Yee, K. *IEEE Trans. Antennas Propag.* **1966**, 302, AP-14.
- 5 Taflove, A. *Computational Electrodynamics: the Finite-Difference Time-domain Method*. Artech House Boston, **1995**.
- 6 Sullivan, D. M. *Electromagnetic Simulation Using the FDTD Method*. IEEE Press, Piscataway, NJ, **2000**.
- 7 H. J. Chen, Z. H. Sun, W. H. Ni, K. C. Woo, H.-Q. Lin, L. D. Sun, J. F. Wang, C. H. Yan, *Small*, **2009**, 5, 2111.
- 8 L. Shao, C. H. Fang, H. J. Chen, Y. C. Man, J. F. Wang, H.-Q. Lin, *Nano Lett.*, **2012**, 12, 1424.

Chapter 3 Au@Pt NRs for *in-situ* Monitoring of Catalytic Reactions by SERS

3.1 Introduction

Noble metal NPs have attracted extensive research attention due to their distinctive plasmonic behaviors, which have been employed in a wide range of local near-field related applications including fluorescence enhancement,^{1,2} SERS,^{3,4} photothermal therapy,^{5,6} and more recently in catalysis, photocatalysis and photovoltaics.⁷⁻⁹ Integration of plasmonic NPs with catalytically-active metals such as Pt and Pd has been obtained to achieve both SERS and catalytic functionalities in a single entity. The resultant bifunctional, hybrid nanostructures have been used to characterize different types of Pt- or Pd-catalyzed reactions by monitoring the SERS response.¹⁰⁻¹⁹ Early demonstrations include the use of Au or Ag NPs coated with a complete shell of Pt or Pd,¹¹⁻¹⁵ and Pd islands deposited on Au nanoshells.¹⁶ More recently, bifunctional Au/Pt/Au nanoraspberries have been synthesized for quantitatively *in-situ* monitoring of Pt-catalyzed reactions by application of SERS.¹⁷ Characterizing the kinetics of catalytic reactions has also been demonstrated using simultaneously immobilized Au and Pt NPs on a substrate.¹⁸

Despite of the significant progress made over the last few years, the following design considerations must be addressed when selecting a target nanostructure that exploits plasmonic effects for SERS enhancement and Pt or Pd for catalysis purpose. The first consideration is the optimization of plasmonic near-field enhancement that directly determines the SERS intensity. In general, one important criterion has to be taken into account for maximizing the near-field enhancement in NPs of regular shapes, namely matching the localized surface plasmon resonance with the excitation laser wavelength and across the



Stokes frequency range. The bifunctional NPs used previously often have a spherical shape, whose localized surface plasmon resonance is difficult to be tuned flexibly,¹³⁻¹⁹ and hence restrict their applications to specific excitation wavelengths. The second design consideration is to have the largest possible surface area of Pt or Pd so as to obtain high catalytic efficiency, which usually requires the use of sub-5 nm catalytic metal NPs and thus a complete shell of Pt or Pd is obviously less favorable.^{11,13,14,17} The third one is to control the surface coverage of catalytic NPs on plasmonic metal cores such that a balance between SERS enhancement and catalytic efficiency can be achieved due to the fact that large-area coating of metals on a plasmonic NP significantly degrade its near-field enhancement.¹⁴ This consideration has not been fully taken into account in previous studies.¹¹⁻¹⁹ Last but not least, in addition to existing approaches using NP films immobilized on a solid support,^{15,16,18,19} it is necessary to monitor catalytic reactions directly in colloidal suspension because many chemical reactions take place in solution environment.

It is worthwhile pointing out that the SERS or tip-enhanced Raman scattering (TERS) technique has also been used to monitor a general class of chemical reactions,²⁰⁻²⁶ such as the photocatalytic decomposition reaction at the interface between metal or metal oxide NPs and flat metal surfaces,^{22,23} and plasmonic “hot” electrons-mediated or plasmon-driven reactions.^{26,27}

In this study, a seed-mediated growth approach was employed to fabricate sub-5 nm Pt NPs-decorated Au NRs with tunable localized surface plasmon resonance wavelength. The surface density of Pt NPs is readily controlled by adjusting the molar ratio of the precursor reaction solution in order to identify an optimized surface coverage of Pt, and its effects on the SERS enhancement and catalytic efficiency are examined in a systematic manner. Finally, the optimized structure is used to monitor in real time the catalytic reaction process of 4-nitrothiophenol (4-NTP) to 4-aminothiophenol (4-ATP) process by



observing the changes of characteristic Raman peaks with increased amount of reductant.

3.2 Synthesis of Au@Pt core-shell Nanostructures

The as-prepared Au NRs were precipitated by centrifugation (6300 g, 10 min), washed once with water (10 mL) and then redispersed in water (10 mL). A mixture of CTAB (3 mL, 0.1 M) and AA (0.4 mL, 0.1 M) were added to the resultant solution followed by adding four different amounts of H_2PtCl_6 (0.01 M) to have different surface coverage of Pt on Au. The four mixed solutions were then placed in an oven set at 60°C overnight. The resultant Au@Pt core/shell nanostructures were separated by centrifugation (6300 g, 10 min) and finally redispersed in water.

3.3 Optical and Morphological Characterizations of Au@Pt NRs

As shown in Figure 3.1(a), the TEM image indicates the as-prepared Au NRs of ~70 nm in length and ~20 nm in diameter. Figures 3.1(b) and (c) show the low and high-magnification TEM images of Au@Pt core/shell nanohybrids, respectively. We can clearly see from Figure 3.1(b) that all the Au NRs are successfully coated with small Pt NPs. Figure 3.1(c) further reveals that the whole surface of each Au NR is uniformly coated by a large number of well-dispersed, discontinuous Pt NPs with diameters of 2-5 nm, which is confirmed by the high-magnification TEM image taken at one end of the Au NR. As discussed above, such configuration is particularly important to achieve strong dual functionalities because the sub-5 nm Pt NPs are expected to have robust catalytic activity benefited from the large surface area to volume ratio, while a significantly-enhanced local electromagnetic field can be generated at the

uncoated areas of Au NRs due to the creation of nanometer-scale gaps.

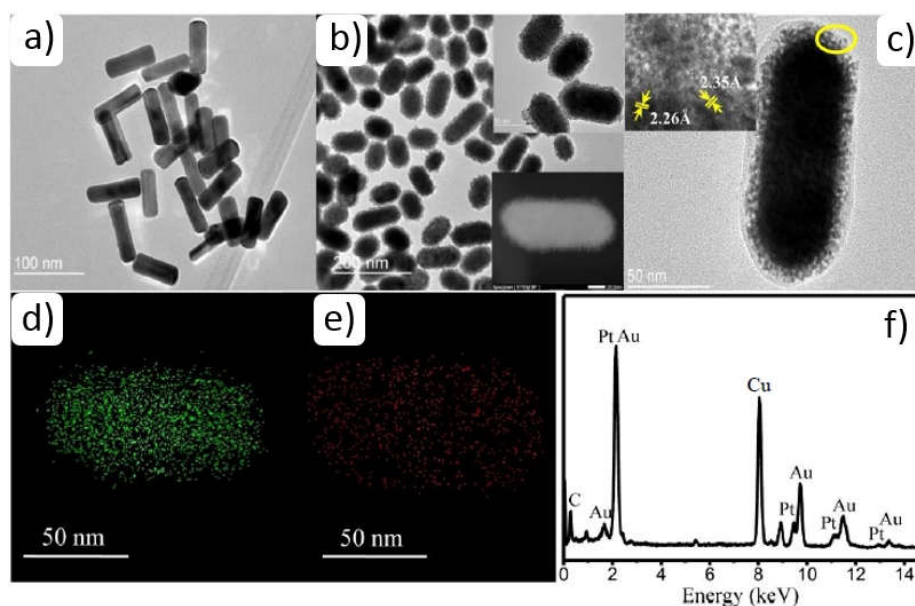


Figure 3.1 Morphology and composition characterizations of Au@Pt nanostructures. (a), (b) and (c) show the TEM images of Au and Au@Pt samples. (d) and (e) are the element mapping of Au and Pt. (f) The EDX map spectrum.

In addition, the high-magnification TEM image also shows that both the Au NRs and most of Pt NPs are single-crystalline and the measured lattice spacings of 0.226 and 0.235 nm correspond to the (111) planes of Pt and Au, respectively (Details shown in Figure 3.1c). Figures 3.1(d) and (e) show the element mapping of Au and Pt in the hybrid nanostructure, respectively, indicating that the Au NRs are uniformly wrapped with Pt NPs. The EDX map spectrum of the hybrid structure also suggests successful coating of Pt on Au. Except the peaks of Cu and C coming from the TEM supporting grid, no other peaks have been observed in the EDX spectrum, indicating high purity of the as-prepared samples.

In order to examine systematically the effects of Pt surface coverage on the

catalytic activity and SERS response of the hybrid Au@Pt core/shell nanohybrids, four samples were prepared with different molar ratios of the Pt precursor and Au NRs. In this experiment, the amount of the selected Au NRs was fixed (10 mL, 10 nM) and four different amounts (60 μ l, 120 μ l, 180 μ l and 240 μ l) of H₂PtCl₆ (0.01 M) were added separately with details described in the experimental section. For the purpose of convenience, the resulting Au@Pt core-shell nanostructures were labelled as Au@Pt-a, Au@Pt-b, Au@Pt-c and Au@Pt-d, with their TEM images shown in Figure 3.2, respectively. One can clearly see from the images that the gradual increase of the amount of Pt precursor has little effects on the NP size but significantly increases the surface density of Pt NPs, which results in a uniform and dense distribution of catalytically-active spots over the Au NR surface. Their optical properties will be discussed in the following sections.

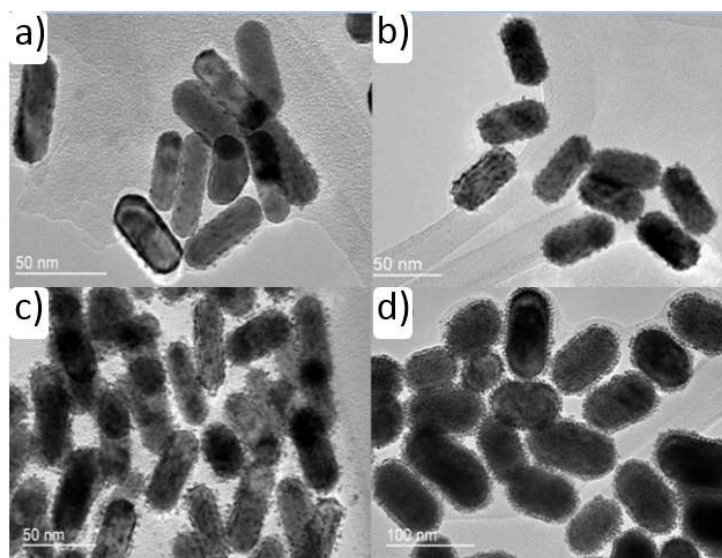


Figure 3.2 TEM images of the Au@Pt hybrid nanostructures with gradual increase in the surface coverage of Pt NPs on Au NRs.

Prior to the growth of Pt NPs, we have carefully tailored the length-to-diameter aspect ratio of Au NRs (~50 nm in length and ~20 nm in diameter) and tuned their localized surface plasmon resonance close to the excitation laser wavelength. Figure 3.3 shows the UV-Vis absorption spectra of the as-prepared Au NRs (1), the oxidized

Au NRs (2) and the Au@Pt-d sample. As can be seen from the figure, the starting Au NRs (1) display two absorption peaks at 515 and 693 nm (red curve), corresponding to the transverse and longitudinal localized surface plasmon resonances, respectively. After oxidation by adding additional H₂AuCl₄ (0.01 M) to the original Au NRs solution, the longitudinal resonance wavelength blue-shifts to 628 nm while the transverse resonance wavelength remains unchanged. Simultaneously, the color of the solution changes from light-grey to sky-blue due to the strong absorption in the red and yellow range of white light by the NRs. Such flexible modulation of localized surface plasmon resonance wavelength makes the Au@Pt core-shell nano hybrids more versatile in matching different excitation wavelengths than the spherical NPs used in previous studies.¹³⁻¹⁹ The other advantage associated with this resonance tuning method is that no other chemicals or ions are introduced and therefore the purity of the samples can be ensured. Figure 3.3 (a) also shows that further growth of Pt NPs on the Au NRs (2) results in little changes in the two resonance positions of the hybrid structure (i.e. Au@Pt-d) but induces significant damping of the longitudinal surface plasmon resonance amplitude, indicating a decrease in the plasmonic near-field enhancement as we will see from the SERS results later.

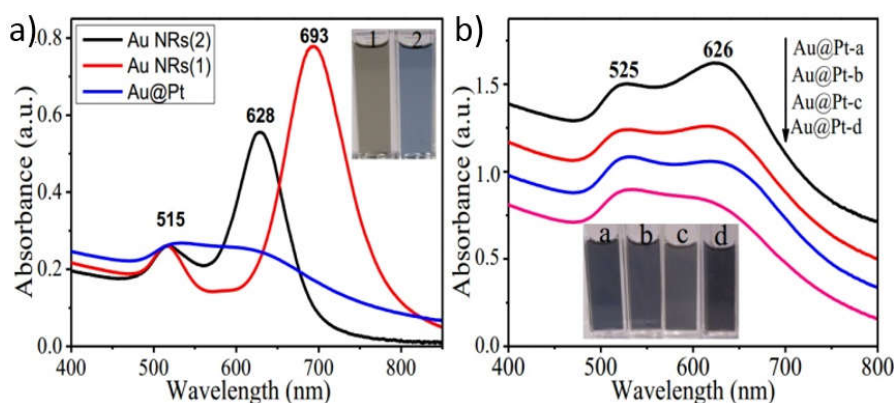


Figure 3.3 (a) Absorption spectra of two kinds of Au NRs. (b) Absorption spectra were measured for the four hybrid nanostructures.

Figure 3.3 (b) shows the UV-Vis absorption spectra for the four hybrid structures,



Au@Pt-a, -b, -c and -d, with Pt surface coverage increasing gradually. The absorption spectra clearly demonstrate that increasing the surface coverage of Pt on Au significantly damps the longitudinal resonance amplitude, resulting in lower absorption intensity. This could be attributed to the fact that the existence of Pt on the surface Au NRs prevents them from efficient excitation of surface plasmons by light and also provides additional ohmic loss channels to plasmon decay. We also note that after coating of Pt, the transverse resonance at 525 nm exhibits little changes in both the resonance position and amplitude. This can be understood from the fact that the electric near-field distribution profiles for the two plasmon resonances are completely different. For the longitudinal plasmon resonance the electric field is tightly localized within a small area at the two ends of the NR, which implies that a small perturbation such as attachment of Pt particles to the NR ends could result in enormous changes to the resonance properties; for the transverse plasmon resonance, the electric field with much weaker intensity is widely distributed over the whole transversal surface and thus much insensitive to changes in the local environment. Note that the Pt particles themselves have no observable absorption characteristic peak in the visible range. The corresponding photographs shown in the inset of Figure 3.3 (b) demonstrate a gradual color change from blue-brown (Au@Pt-a) to blue-black (Au@Pt-d) with the increase of Pt particles attached on the Au surfaces.

3.4 Monitoring of Catalytic Reactions of the Au@Pt NRs by SERS

3.4.1 Catalytic Activity of Au@Pt NRs

To explore the catalytic property of the Au@Pt core/shell nanostructures, the 4-NTP molecule was chosen as analyte in the experiments. A quartz vessel (4 mL capacity) was used as the catalysis reactor in which each of the following five samples,

including Au NRs, Au@Pt-a, -b, -c and -d hybrid nanostructures, was mixed separately with the 4-NTP solution. The catalytic activity of each structure was then determined by recording the absorption intensity of 4-NTP at wavelength 410 nm. It is due to the formation of 4-nitrophenolate ions from 4-NTP in the alkaline condition caused by the addition of NaBH₄. The detailed catalytic mechanism can be seen from Figure 3.4. The Pt NPs act as a catalyst and the catalytic reaction takes place at their surfaces. The borohydride ions react with Pt, forming a metal hydride to catalyze 4-NTP molecules. We recorded the absorption intensity as a function of reaction time and calculated the catalytic reaction rate using the well-established pseudo-first-order approximation.

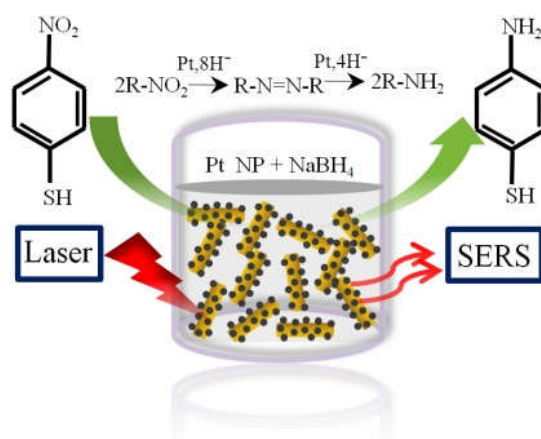


Figure 3.4 Representation of the reduction of 4-NTP by NaBH₄ to 4-AP, which takes place on Au@Pt superstructure surfaces. The reaction is catalyzed by the Pt NPs, while the SERS signal is brought about by local optical fields of the Au NRs.

Figure 3.5 renders the time-dependent UV-Vis absorption spectra of the 4-NTP solution (10⁻³ M) mixed respectively with the Au@Pt-b, Au@Pt-c and Au@Pt-d nanostructures. It can be clearly seen that the absorption intensity of 4-NTP at wavelength 410 nm decreases with the increase of NaBH₄ in the presence of the Au@Pt hybrid nanostructures and that the decreasing rate accelerates with the surface coverage of Pt NPs. In this way, as soon as we added the NaBH₄, these Pt NPs started the catalytic reduction by relaying electrons from the donor BH₄⁻ to the acceptor 4-

nitrophenol right after the adsorption of both onto the particle surfaces. Furthermore, the addition of a small amount of Au@Pt NPs can cause fading and ultimate bleaching of the yellow color of the reaction mixture. It shows the normalized concentration of 4-NTP, which is extracted from the absorption intensity and plotted as a function of reaction time in each of the five structures used in this study. By fitting each curve with an exponential decay function under the pseudo-first-order approximation, an apparent rate constant for the degradation of 4-NTP in each catalyst can be extracted to compare quantitatively the catalytic performance.

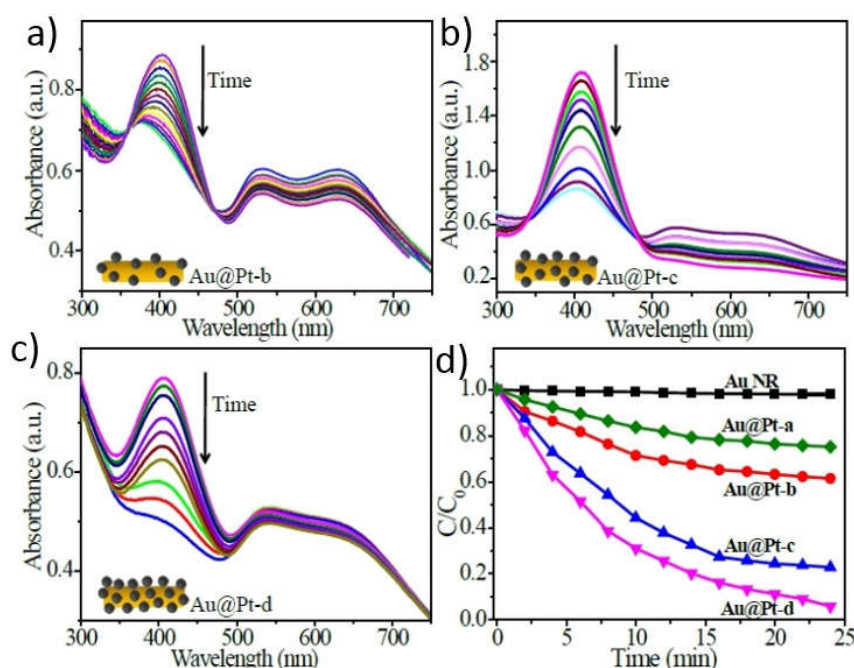


Figure 3.5 (a)-(c) Absorption spectra of the 4-NTP solution mixed respectively with the Au@Pt superstructures. (d) Normalized concentration of 4-NTP as a function of time.

There is a plasmon dampening in the colloidal spectra shown in Figure 3.5, because during catalytic reaction, the NaBH_4 solution was added in the mixed solution and thus the particle concentration decreases. In other words, after adding of NaBH_4 , the concentration of the Au@Pt core/shell nanostructures solution became increasingly low. To be specific, in Figures 3.5 (a) and (b), the original particle



concentrations are high; while the particle concentration changes are relatively large when diluted, therefore the plasma dampening looks obvious. However, in Figure 3.5 (c), the original particle concentration is low, when the particle concentration changes, the plasmon dampening changes less and thus looks not obvious.

The particle interband transition plays an important role in the extinction.²⁹ To be specific, for the high light extinction coefficient and the interband transition of Au core, the SPR bands at 410 nm were enhanced; but for the low light extinction coefficient and the inter-band transition of Pt shell, the SPR bands were damped. This study mainly focused on the effect of different Pt amount on the catalytic properties so we did not consider the particle's interband transition effect because the original extinction has little effect on the catalytic property of these particles.

We investigated the catalytic efficiency and discussed the reaction rate constants k for the different samples by comparison of decreases gradually in intensity of absorption peak for the reactant (4-NTP) at 410 nm. For further comparison of the catalytic efficiency of the different Au@Pt nanohybrids, $-\ln(A_{410(t)}/A_{410(0)})$ as a function of reaction time is depicted in Figure 3.6, in which $A_{410(t)}$ and $A_{410(0)}$ are the absorbance at fixed intervals and the initial stage. A linear relationship is obtained for all the nanohybrids samples, indicating pseudo-first-order kinetics for the reduction reactions. The reaction rate constants k are found to be 1.8, 2.7, 5.2, and $6.3 \times 10^{-4} \text{ s}^{-1}$ for Au@Pt-a, b, c, and d, respectively, as calculated from the linear fit equation $\ln(A_{410(t)}/A_{410(0)}) = -kt$. In sharp contrast, the concentration of 4-NTP remains unchanged in the presence of the bare Au NRs, demonstrating that Au NRs have none or very weak catalytic activity. This is due to the fact that in the absence of a proper catalyst, the thermodynamically favorable reduction of 4-nitrophenol is not launched and thus the peak due to 4-nitrophenol ions at 410 nm remains unaltered even after a couple of days as reported in the literature.¹⁴

3.4.2 Recyclability of Catalysts

The recyclability of catalysts is an important issue in their practical application. To evaluate the feasibility of the recyclable property for the Au@Pt core/shell nanostructures, three successive cycles of catalytic reactions using the same Au@Pt-c nanostructures were carried out as shown in Figure 3.6 (b). After each cycle, the nanostructures were centrifuged by DI water and then air-dried. There is a slight change in the reaction rate constant after three cycles. The k value still closes to that of the original Au@Pt hybrids. The main reason for the decrease in catalytic efficiency may be the loss of catalyst during the recycling process. The results demonstrate that these nanostructures have good catalytic stability in aqueous solution. Besides, we investigate the morphology change before and after the catalytic reaction because the dual functionalities of SERS enhancement and catalytic property in the Au@Pt nanostructures are based on the hybrid nanostructures containing plasmonic metal cores and catalytic metal shells. It is found that, although after three cycles, the morphologies of the coated Pt nanoparticles as well as the Au NRs keep almost unchanged and each Au NR is uniformly coated by a large number of well-dispersed Pt NPs with diameters of 2-5 nm. Maybe it's mainly due to the low laser power and the good heat dissipation of the liquid solution surrounding the Au@Pt nanostructures. All these results confirmed that these Au@Pt core/shell nanostructures can be recycled.

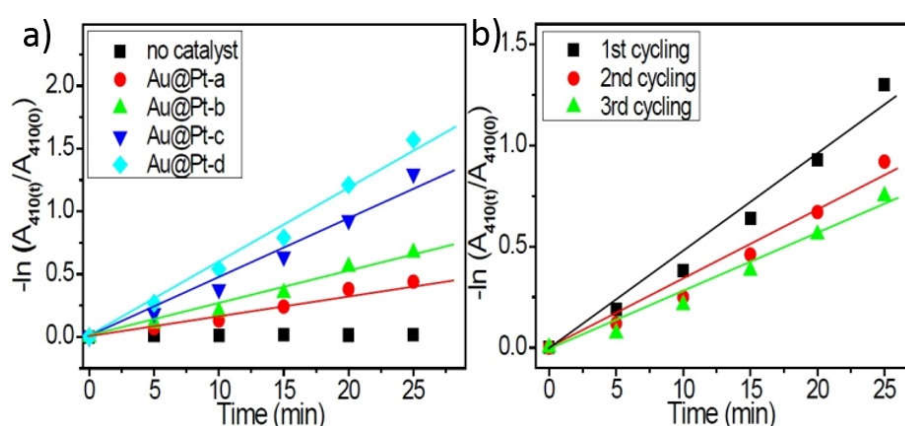


Figure 3.6 (a) The plot of $\ln(A_{410(t)}/A_{410(0)})$ as a function of time for the reaction catalyzed by different samples. (b) Three cycles of catalytic activity of the Au@Pt-c

hybrids.

In Figure 3.7 it is found that, even after three cycles, the morphologies of the Pt coated nanoparticles as well as the Au NRs keep almost unchanged and each Au NR is uniformly coated by a large number of well-dispersed Pt NPs with diameters of 2-5 nm. In addition, we find no colloidal aggregations or changes in their shapes. Such morphology preservation might be due mainly to the low laser power and good heat dissipation of the liquid solution surrounding the Au@Pt nano hybrids. All these results confirmed that these Au@Pt core-shell nanostructures can be recycled.

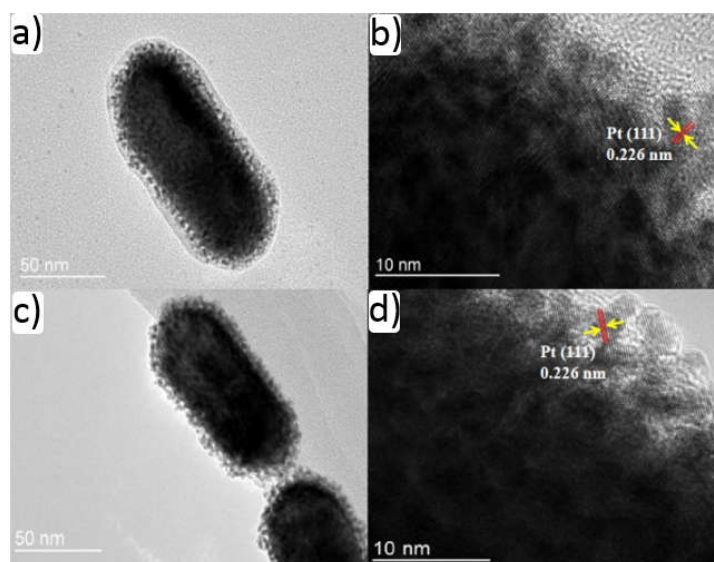


Figure 3.7 TEM images of Au@Pt core/shell nanostructures before (a) and (b) and after (c) and (d) three cycles.

3.4.3 SERS Activity of the Au@Pt NRs

Once we have determined the catalytic activity of the hybrid structures, in the following we move to study their SERS sensitivities, one of the dual functionalities. In this experiment, we mixed the solution of 4-NTP and each of the metal nanostructures and kept the mixture for a certain period of time to allow for a self-assembled monolayer of 4-NTP adsorbed on the surface of metal nanostructures.

Figure 3.8 (a) shows the SERS spectra of 4-NTP collected from the Au NRs and Au@Pt core/shell nanostructures. The Raman band at ca.1078, 1345 and 1572 cm^{-1} can be assigned respectively to the S-C stretching vibration, symmetric nitro stretching vibration and phenyl ring modes, respectively. To compare quantitatively the SERS enhancements from the five structures, Figure 3.8 (b) shows direct comparison between the measured Raman intensities at the four characteristic Raman peaks of 4-NTP for the five samples, which clearly demonstrates that the Raman intensity of 4-NTP decreases significantly with the increase of Pt coverage.

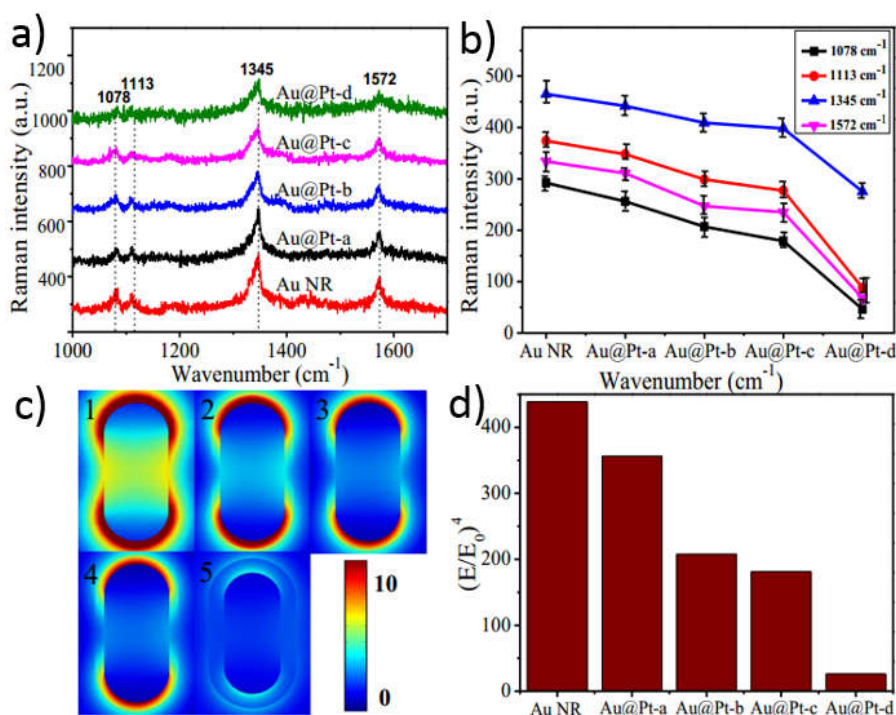


Figure 3.8 (a), (b) Measured SERS responses and (c), (d) calculated near-field for different Au@Pt samples.

As shown in Figure 3.8 (a) shows SERS spectra collected from 4-NTP self-assembled on the surface of Au and Au@Pt nanohybrids. 3.8 (b) presents Raman intensities at bands 1078 (black square), 1113 (red circle), 1345 (blue up-triangle) and 1572 cm^{-1} (purple down-triangle) extracted from (a), with each data point representing an average value from three measurements. The solid lines are guide to the eyes. 3.8 (c) indicates the cross-sectional view of the normalized electric-field intensity distribution profiles for the bare Au NR (1) and Au@Pt nanohybrids (2-5 for Au@Pt-



a,-b, -c and -d). The shell thickness of the effective medium is 3 nm for Au@Pt-a, -b, and -c and 6 nm for Au@Pt-d as determined from the TEM images shown in 3.8 (d). Spatially-averaged biquadratic field enhancement factors for Au and Au@Pt nanohybrids by integrating the enhancement over a closed surface at a distance of 1 nm from the NP surface. All the Raman band intensities were directly extracted from the spectra by comparing the Raman peaks height. For example, for the average SERS enhancements, the SERS signals were randomly collected from a number of positions on the Au@Pt core/shell nanohybrid substrate and following the Raman band intensities were extracted by measuring the average peaks height.

3.4.4 Mechanisms for the Different SERS Enhancements

To understand the underlying mechanism responsible for the different SERS enhancements observed as well as how the plasmonic behavior in the Au NR is governed by the dielectric variation in the shell, we employed the finite-element method, implemented in the multi-physics COMSOL software, to calculate the electric near-field enhancement factors for the four hybrid structures and the bare Au NR excited at wavelength 633 nm with incident polarization along the long axis of the rod. Here the dielectric response of the shell on the Au NR (50 nm in length and 22 nm in diameter) is modelled as an effective medium consisting of air and Pt NPs (3 nm in diameter) with the volume fraction of Pt determined from the TEM images (3.84%, 4.97%, 5.37%, and 13.93% for Au@Pt-a, -b, -c and -d, respectively). Figure 3.8 (c) presents the field intensity distribution profiles for the Au NR and Au@Pt nanohybrids, which show that the field intensity is suppressed gradually with increasing volume fraction of Pt. Since the 4-NTP molecules are expected to adsorb over the whole surface of metal NPs, the measured Raman intensity should be proportional to the integration of the biquadratic E-field enhancement over the NP surface.^{30,31}

$$I_{SERS} = \frac{1}{\Omega} \int \left(\frac{E}{E_0}\right)^4 dS$$

Where Ω is the area of a closed surface enclosing the nanostructure with 1 nm



distance from the NP surface and S is the surface integration element. Figure 3.8 (d) illustrates the spatially-averaged E-field enhancement factors calculated with the above equation for the five structures, showing perfect agreement with the SERS results. This confirms that the degraded SERS response in Au@Pt nanohybrids indeed comes from the field-shielding effect caused by the Pt coating and that larger surface coverage of Pt (corresponding to stronger catalytic activity) results in smaller near-field enhancement.

To verify whether the tuning of the NR surface plasmon resonance actually contribute to the improvement in the SERS intensity or not, some additional control experiments have been done. Two types of Au NRs with different surface plasmon resonance were first chosen to perform the SERS measurements in the same condition (Au NP concentrations, analyte concentration and laser power, etc.). The detailed SERS results are shown in Figure 3.9 and from which it is clearly seen that, after tailoring the surface plasmon resonance of Au NRs, the SERS signals from 628 nm longitudinal resonance wavelength NRs are improved obviously compared to the 693 nm longitudinal resonance wavelength ones (The data were collected randomly from several points and we picked the average values). It can be found that the signals from the 628 nm NRs are doubled compared to the 693 nm NRs'. Because the Au@Pt core/shell nanostructures have a good reproducibility across the entire substrate, it is believed that the tuning of the rod SPR prior to Pt coating actually contributes to the improvement in the SERS intensity. In addition, control SERS experiments on using unmatched excitation wavelength (488 nm) have been done by the two types of NRs. It can be seen that the SERS signals from the unmatched excitation wavelengths cannot be found clearly either in the starting NRs (1) or in the oxidized NRs (2). These results further confirmed the great importance of using the matched nanostructures and excitation wavelengths in the SERS tests.

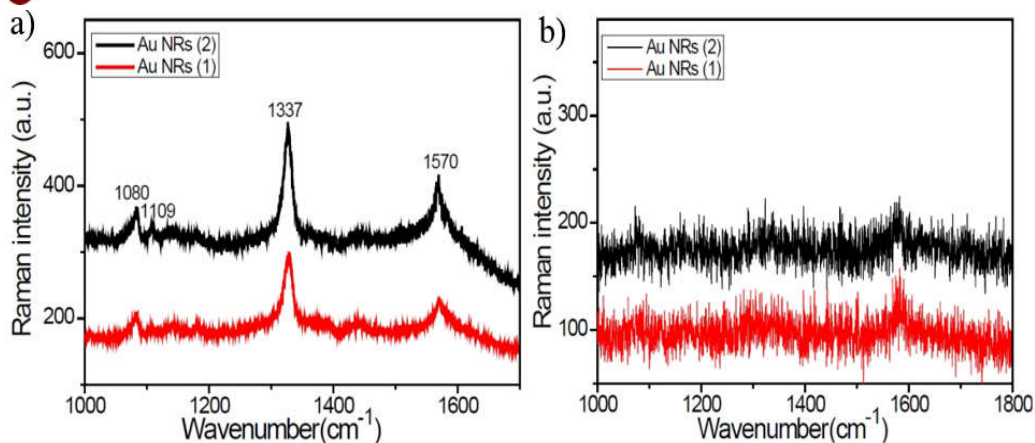


Figure 3.9 (a): SERS spectra collected for 4-NTP molecules adsorbed on two types of Au NRs with LSPR wavelengths at 628 nm (black curve) and 693 nm (red curve), respectively. (b) SERS spectra for the same measurements as that in (a) while the laser excitation wavelength is changed to 488 nm.

3.4.5 Reproducibility and Stability of SERS Substrates

While employing SERS technology to prepare recyclable Au@Pt core/shell nanostructures SERS substrates, reproducibility and stability of SERS substrates must be validated. The SERS experiments on Au@Pt-c substrate have been done to confirm the repeatability of the hybrid nanostructures. The relative standard deviation (RSD) of major peaks is often used to estimate the reproducibility of SERS signals. Figure 3.10 shows the SERS-RSD spectrum of 4-NTP molecules in the Raman shift range of 1000-1700 cm⁻¹, which is randomly collected from a number of positions on the substrate. The maximal RSD value of signal intensities of major SERS peaks is observed to be below 0.2, indicating that the Au@Pt-c core/shell nanostructures have a good reproducibility across the entire solution. From Figure 3.10 it can be found that, although the SERS signals are not very strong, the reproducibility and stability of the substrate are reversely good. It may be due to the fact that the excitation laser beam is appropriate (the diameter is 2 μm and the excitation depth is about 20 μm), and the particle concentration is relatively high in the solution (10^{-9} M~ 10^{-10} M), thus we can

speculate that those nanoparticles contributed the SERS signals are uniform and fixed. In that case, it is not surprising that there is a good repeatability of the SERS measurement using Au@Pt core/shell nanostructures.

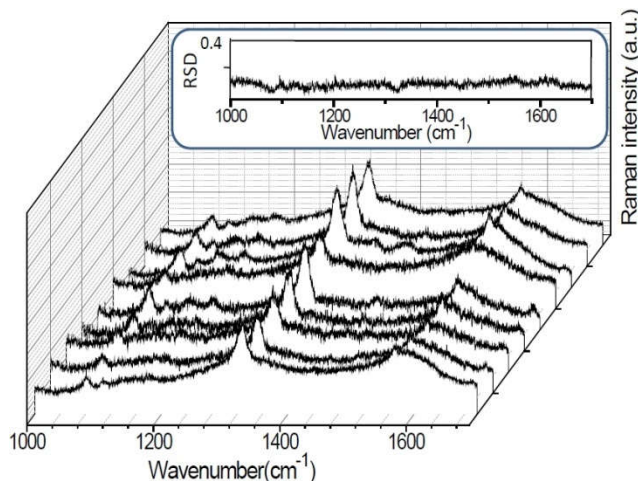


Figure 3.10 The SERS-RSD spectrum of 4-NTP molecules in the Raman shift range of 1000-1700 cm^{-1} , randomly collected from a number of positions on the Au@Pt core/shell substrate.

3.4.6 Monitoring of Catalytic Reaction by the SERS Substrates

It is well known that sub-5 nm Pt NPs own an excellent catalytic property due to their favorable electronic characteristics and huge surface area to volume ratio, and these small NPs usually have a poor SERS response. However, the hybrid structure can afford a platform for these Pt NPs to benefit from the field enhancement effect of the Au NR, which is the basis for realizing the bifunctional property and allows us to in-situ monitor the catalytic reaction process by recording the SERS response in real time. In the experiment, the Au@Pt-c structure was chosen as the optical probe because it exhibits a good balance between the catalytic activity and the SERS enhancement. The SERS spectrum was recorded each time after adding the NaBH_4 aqueous solution of 5 μL (10^{-3} M) to the Au@Pt solution of 600 μL (0.2 nM) with self-

assembled 4-NTP on the NP surface. The aqueous solution of NaBH₄ was continuously added till all the 4-NTP molecules were decomposed completely.

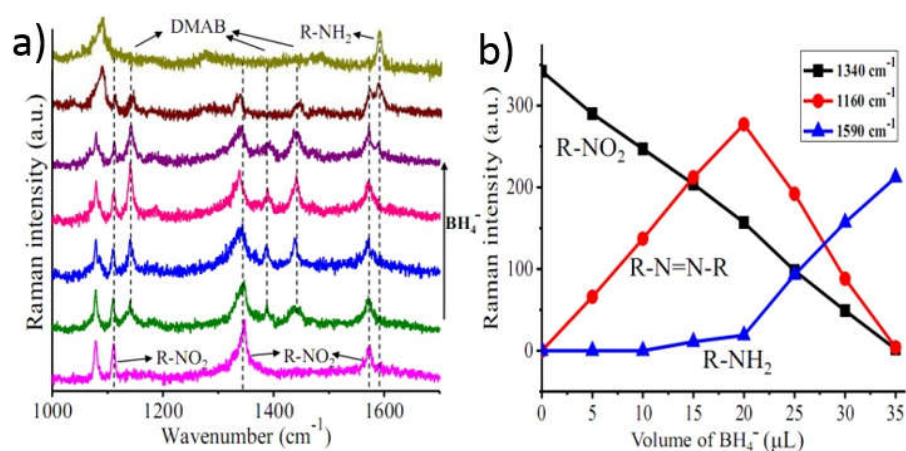


Figure 3.11 SERS spectroscopy recorded upon addition of different amounts of the NaBH₄ with Au@Pt nanohybrids. (a) Raman spectra recorded from 4-NTP molecules. (b) Raman intensities extracted from (a) at the bands 1340, 1160 and 1590 cm⁻¹, respectively.

Figure 3.11 shows a series of Raman spectra collected from the mixed solution in sequence of the addition of NaBH₄ (from bottom to top). The Raman spectrum at the bottom demonstrates that the reactant is pure 4-NTP as the three characteristic peaks at 1113, 1345 and 1572 cm⁻¹ are clearly observed. Upon addition of the solution of NaBH₄, the intensities of the Raman peaks associated with 4-NTP start to decrease immediately and three new peaks at 1140, 1385 and 1434 cm⁻¹ appear accordingly, which can be assigned to the vibrational modes of 4,4'-dimercapto-azobenzene(4,4'-DMAB), an intermediate product. Specifically, these three new Raman peaks correspond to the C-N symmetric stretching, N=N stretching, and C-H in-plane bending modes in 4,4'-DMAB, respectively.²¹ More interestingly, the intensities of the Raman peaks for 4,4'-DMAB significantly increase with further addition of NaBH₄ (from the green to red spectra) and then abruptly decrease till nearly zero (from the black to dark-yellow curve), further corroborating its character as an intermediate product. Meanwhile, the intensities of the peaks for 4-NTP also fade and vanish till



zero and a new peak at 1590 cm^{-1} , which corresponds to the amino vibrational mode, emerges accordingly and finally dominates the spectrum. We summarize the observations made above by plotting the Raman intensities of three characteristic peaks with each associated with the reactant 4-NTP, the intermediate product 4,4'-DMAB and the final product 4-ATP. More importantly, it provides quantitative information about their relative concentrations in the reaction process. It is also important to note that the 4,4'-DMAB increases while the 4-NTP decreases with adding NaBH_4 . After addition of a certain volume of NaBH_4 (20 μL in our case), the amount of 4,4'-DMAB decreases while the amount of 4-ATP arises rapidly since this conversion reflects a sequential hydride reduction of 4-NTP to 4,4'-DMAB and finally to 4-ATP. After adding a sufficient volume of BH_4^- (35 μL in our case), the 4-NTP and 4,4'-DMAB both transform completely and the product is 4-ATP only.

It should be noted that the signal to noise ratio of the SERS spectra is relatively low. This may be due to the following two reasons: (1) in the SERS experiment, we mixed the solution of 4-NTP and each of the metal nanostructures, and to allow for a self-assembled monolayer of 4-NTP adsorbed on the surface of metal nanostructures, then washed out the residual 4-NTP molecules and diluted the mixed solution. Therefore, it is assumed that the efficient 4-NTP molecules contributing to SERS signal enhancements are relatively low; (2) the residual CTAB molecules on the surface of the Au@Pt core/shell nanostructures will cause the poor affinity between the hybrid nanostructures and the absorbed molecules will also result in a low SERS signal.

Moreover, the particle density will have without question an important impact when comparing relative SERS intensities. In fact, in order to optimize the SERS signals from the metal NPs, a series of particle concentrations have been chosen in SERS measurements to determine the maximized enhancement. For example, the SERS signals of metal NPs with 10^{-11} - 10^{-12} M concentrations would be extraordinary low or disappear compared to the higher particle concentrations such as 10^{-9} - 10^{-10} M

in our experiments. But slight variations in particle density will not have a significant impact when comparing relative SERS intensities.

3.5 Summary

We have prepared Au@Pt core/shell nanostructures using a facile wet chemical method, and the synthesized hybrid structures exhibit tunable localized surface plasmon resonance, excellent catalytic activity and strong SERS enhancement. We have demonstrated that the dual functionalities, catalysis and SERS of the hybrid structures can be readily tailored by adjusting the surface decoration density of Pt NPs on the surfaces of Au NRs, and a balance between them can be achieved at an optimal surface density. The optimized hybrid nanostructure has been used as a sensitive optical probe to in-situ monitor the catalytic reaction process by recording the SERS response in real time, enabling the determination of the intermediate and final products and their quantities. We believe that this SERS-based synergy technique could be applied to a more general class of chemical reactions and study of the reaction process both qualitatively and quantitatively by recording both the Raman peak positions and intensities.

References

- 1 V. Giannini, A. I. Fernández-Domínguez, S. C. Heck, and S. A. Maier, *Chem. Rev.*, 2011, **111**, 3888.
- 2 A. Kinkhabwala, Z. F. Yu, S. H. Fan, Y. Avlasevich, K. Müllen and W. E. Moerner, *Nat. Photon.*, 2009, **3**, 654.
- 3 K. Kneipp, H. Kneipp, I. Itzkan, R. R. Dasari, and M. S. Feld, *Chem. Rev.*, 1999, **99**, 2957.
- 4 Y. Wang, B. Yan, L. Chen, *Chem. Rev.*, 2013, **113**, 1391.



- 5 A. O. Govorov, H. H. Richardson, *Nano Today*, 2007, 2, 30.
- 6 J.-W. Kim, E. I. Galanzha, E. V. Shashkov, H.-M. Moon, V. P. Zharov, *Nat. Photon.*, 2009, 4, 688.
- 7 P. Fang, S. Duan, X. Lin, J. R. Anema, J. Li, O. Buriez, Y. Ding, F. Fan, D. Wu, B. Ren, Z. L. Wang, C. Amatore and Z. Q. Tian, *Chem. Sci.*, 2011, 2, 531.
- 8 A. Marimuthu, J. W. Zhang, S. Linic, *Science*, 2013, 339, 1590.
- 9 H. Kim, K. M. Kosuda, R. P. Van Duyne, P. C. Stair, *Chem. Soc. Rev.*, 2010, **39**, 4820.
- 10 J. Y. Chen, B. Wiley, J. McLellan, Y. J. Xiong, Z. Y. Li, Y. N. Xia, *Nano Lett.*, 2005, 5, 2058.
- 11 S. J. Guo, L. Wang, Y. Wang, Y. Fang, E. K. Wang, *J. Colloid Interface Sci.*, 2007, **315**, 363.
- 12 S. Z. Zou, C. T. Williams, E. K. Y. Chen, M. J. Weaver, *J. Am. Chem. Soc.*, 1998, **120**, 3811.
- 13 L. Guerrini, E. Lopez-Tobar, J. V. Garcia-Ramos, C. Domingo, S. Sanchez-Cortes, *Chem. Commun.*, 2011, **47**, 3174.
- 14 K. Kim, K. L. Kim and K. S. Shin, *J. Phys. Chem. C*, 2011, **115**, 14844.
- 15 K. N. Heck, B. G. Janesko, G. E. Scuseria, N. J. Halas and M. S. Wong, *J. Am. Chem. Soc.*, 2008, **130**, 16592.
- 16 W. Xie, C. Herrmann, K. Kompe, M. Haase and S. Schlücker, *J. Am. Chem. Soc.*, 2011, **133**, 19302.
- 17 V. Joseph, C. Engelbrekt, J. Zhang, U. Gernert, J. Ulstrup and J. Kneipp, *Angew. Chem. Int. Ed.*, 2012, **51**, 7592.
- 18 M. Cao, L. Zhou, X. Xu, S. Cheng, J. L. Yao and L. J. Fan, *J. Mater. Chem. A*, 2013, 1, 8942.
- 19 Y. F. Huang, H. P. Zhu, G. K. Liu, D. Y. Wu, B. Ren and Z. Q. Tian, *J. Am. Chem. Soc.*, 2010, **132**, 9244.
- 20 D. Y. Wu, L. B. Zhao, X. M. Liu, R. Huang, Y. F. Huang, B. Ren, Z. Q. Tian,



- Chem. Commun.*, 2011, **47**, 2520.
- 21 E. M. van Schrojenstein Lantman, T. Deckert-Gaudig, A. J. G. Mank, V. Deckert and B. M. Weckhuysen, *Nat. Nanotechnol.*, 2012, **7**, 583.
- 22 L. Li, T. Hutter, A. Finnermore, F. M. Huang, J. J. Baumberg, S. Elliot, U. Steiner and S. Mahajan, *Nano Lett.*, 2012, **12**, 4242.
- 23 Z. Dai, X. Xiao, Y. Zhang, F. Ren, W. Wu, S. Zhang, J. Zhou, F. Mei and C. Jiang, *Nanotechnology*, 2012, **23**, 335701.
- 24 W. Xie, B. Walkenfort and S. Schlücker, *J. Am. Chem. Soc.*, 2013, **135**, 1657.
- 25 M. Sun, Z. Zhang, H. Zheng and H. Xu, *Sci. Rep.*, 2012, **2**, 647.
- 26 M. D. Xiao, R. B. Jiang, F. Wang, C. H. Fang, J. F. Wang, J. Yu, *J. Mater. Chem. A*, 2013, **1**, 5790.
- 27 S. Mukherjee, F. Libisch, N. Large, O. Neumann, L. V. Brown, J. Cheng, J. B. Lassiter, E. A. Carter, P. Nordlander and N. J. Halas, *Nano Lett.*, 2013, **13**, 240.
- 28 W. Ni, X. Kou, Z. Yang and J. Wang, *ACS Nano*, 2008, **2**, 677.
- 29 R. Liu, J.-F. Liu, Z. -M. Zhang, L. -Q. Zhang, J. -F. Sun, M. -T. Sun, and G. -B. Jiang, *J. Phys. Chem. Lett.* 2014, **5**, 969.
- 30 Z. Y. Bao, J. Y. Dai, D. Y. Lei and Y. C. Wu, *J. Appl. Phys.*, 2013, **114**, 124305.
- 31 Y. D. Zhao, X. Liu, D. Y. Lei and Y. Chai, *Nanoscale*, 2013, **6**, 1311.

Chapter 4 Interband Absorption Enhanced Optical Activity by Au@Ag nanocuboids

4.1 Introduction

Optical chirality and nonzero CD are present in a molecule if the molecular structure has neither a mirror plane nor an inversion center. In other words, the molecule acquires a sense of rotation and hence reacts differently to right- and left-handed circularly polarized lights.¹⁻⁵ One of the well-established methods, known as CD spectroscopy, is widely utilized to examine the efficiency of synthetic organic chemical reactions and determine enantiomer handedness, protein folding, and conformational changes of chiral molecules due to physical and chemical stimuli.⁶⁻⁹ In particular, the molecular recognition capability in stereochemistry offers the possibility to design and realize “smart” systems with the ability of chiral discrimination.¹⁰⁻¹⁴ Chiral detection of cysteine, a typical proteinogenic amino acid, has been intensively studied because of its critical role in many biological systems. For example, anomalous concentration of cysteine in blood is an important beacon of various diseases such as Alzheimer’s disease, cardiovascular disease, liver damage, and skin lesions.¹⁵⁻²⁰ However, the CD signals of many biomolecules like cysteine are typically very weak, and thus a significant amount of materials at a relatively high concentration is required for producing a detectable signal, constituting a technical impediment in many practical aspects.

Subwavelength nanostructures made of noble metals (such as Au and Ag) support localized surface plasmons (LSPs) - the collective oscillation of conduction electrons at a metal-dielectric interface. Upon resonant excitation of LSPs, the incident light energy can be squeezed into a nanoscale volume around a metal nanostructure, thereby largely enhancing the local field strength and consequently the light-matter interaction for a molecule, for instance, adsorbed on the surface of the metal nanostructure.²¹⁻²⁴



The enhanced electromagnetic interaction serves as the basis for using LSPs-based nanosensors to locally detect nanoscale environmental changes, such as molecular-binding events, catalytic reactions, phase-changing processes, and hydrogen adsorption dynamics.²⁵⁻³¹ It has been demonstrated that there is a direct correlation between the sensitivity of such a nanosensor and the near-field intensity enhancement around the metal nanostructure.^{11,13} Recently, the enhanced plasmonic fields in achiral metal nanoparticles were employed to modulate the CD response of chemisorbed chiral molecules.⁶ On the one hand, the plasmon-induced CD bands were observed in the complex of a metal nanoparticle and chiral molecules in the spectral range corresponding to the LSP band of the metal nanoparticle ($\lambda > 350$ nm), and the new CD bands were generally believed to arise from either the molecule-induced atomic-scale chirality of the metal nanoparticle itself,^{6,32-36} chiral arrangement of the thiolates attached on the surface of the nanoparticle,³⁷⁻³⁸ electronic ‘imprint’ of the molecule’s chirality (for example, peptides),³⁹⁻⁴⁵ or the molecular linkers mediated chiral arrangement of nanoparticle assemblies at the nano- and sub-microscale.^{10,46} On the other hand, the UV chiroptical activity in the spectral range of 220 - 380 nm was observed in aqueous solutions of Ag^+ and cysteine or Ag^+ -cysteine coordination polymers, due to $\text{Ag}^+ \dots \text{Ag}^+$ argentophilic interaction and electrostatic interaction between neighboring amino acid residues.^{18,19} The UV chiroptical activity was generally thought to be related to the formation of chiral aggregates consisting of metal ions and chiral molecules, and has rarely been observed in a hybrid of an individual metal nanoparticle and chiral molecules.¹⁷⁻¹⁹

Besides supporting the geometry-dependent LSPs, noble metal nanoparticles such as chemically prepared Au and Ag nanoparticles also have strong intrinsic interband absorption due to photo-excited interband transitions in the wavelength range of around 220 - 320 nm. The interband transition in a noble metal involves the promotion of an electron from an occupied *d*-level state to an empty state above the Fermi level, and the induced absorption is strongly determined by the joint density of

d and *s* states of the conduction electrons.⁴⁷ Previous studies seldom reported the use of interband transitions because of their high energy levels located in the ultraviolet region, but recent research has ignited the interest in this intrinsic property of noble metals. For example, surfactants and capping molecules were observed to influence the intensity and linewidth of the interband absorption peaks of Au and Ag spherical nanoparticles due to their spectral overlapping with the absorption of the molecules and this effect was successfully used for novel biosensing applications.⁴⁸ Moreover, the third harmonic generation from Au nanoparticles was strongly enhanced when the fundamental beam energy was approximately one third of the interband transition energy of Au.⁴⁹ Considering the significant matching of their resonance energies, one can thus anticipate that the interband transitions of noble metal nanoparticles can accelerate the electronic transitions of adhered molecules, consequently amplifying the absorption difference of right- and left-handed circularly polarized lights by the chiral molecules.

Here we report on the observation of an unusual CD resonance at the interband transition region of discrete achiral Au@Ag core-shell nanocuboids (CSNCs) chemisorbed by chiral cysteine molecules. The new CD band spectrally deviates from that of pristine cysteine and shows a 170-fold intensity enhancement. Comprehensive studies as functions of solution temperature, pH value and added ions, together with Raman spectroscopy and electromagnetic calculations, reveal the formation of extended helical networks through linking the amino nitrogen and carboxylate oxygen atoms of neighboring cysteine molecules with hydrogen bonds, which is responsible for the origin of the new CD band that is dramatically enhanced by the interband transition of Ag.

4.2 Morphological Characterizations of Au@Ag Nanocuboids

Figure 4.1 (a) depicts a typical TEM image of the as-prepared Au@Ag CSNCs

of ~ 90 nm in length and ~ 60 nm in diameter. The Au NR cores are ~ 50 nm in length and ~ 10 nm in diameter. The inset shows the cysteine-coated Au@Ag CSNCs used in the CD experiments, demonstrating good dispersion and no aggregation. Figures 4.1 (b) and (c) show the high-magnification TEM and STEM images of an individual Au@Ag/L-cysteine CSNC, corroborating that the Au NR core is fully wrapped with a uniform Ag shell, consistent with the elemental mappings of Ag and Au as shown in Figures 4.1 (d) and (e). Note that the O and S elemental mappings shown in Figures 4.1 (f) and (g) confirm a uniform coating of cysteine on the CSNC. Figure 4.1 (h) depicts the Au and Ag crystal-lattice mappings profiled by the red dash line. The inset shows a Fast Fourier Transform (FFT) image captured over a small area of the Au@Ag CSNC, and two clear sets of diffraction spots are observed, indicating that both Au core and Ag shell are single crystals. Further calculations show that the interplanar spacings measured for the core and shell regions are 0.210 nm and 0.232 nm, corresponding to Au (200) and Ag (111) crystal planes, respectively.

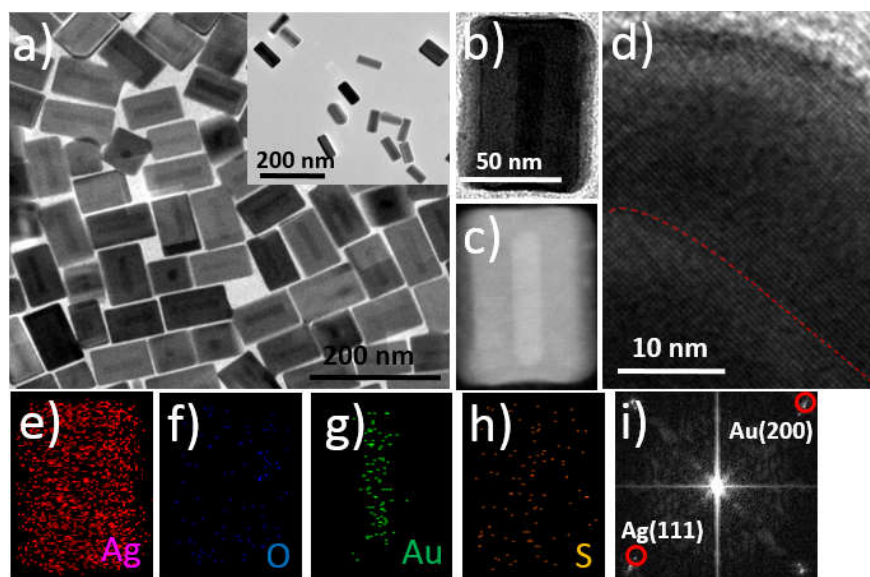


Figure 4.1 Morphology and composition characterizations of as-prepared Au@Ag CSNCs.

4.3 Characterizations of Conformation Change of Cysteine on Ag Surface

FT-IR spectra were measured to characterize the chemical environment and conformation change of cysteine molecules before and after adsorbed on the surface of Au@Ag CSNC (Figure 4.2). It is noted the L-cysteine in solution shows an evident absorption band at 2551 cm^{-1} because of S-H stretching vibration (black curve), which is absent in the spectrum of the L-cysteine adsorbed on Au@Ag CSNCs (red curve), indicating the formation of thiolates and covalent interaction of Ag-S bond. The two characteristic peaks of symmetric $\nu_s(\text{COO}^-)$ ($\sim 1392\text{ cm}^{-1}$) and asymmetric stretching $\nu_{as}(\text{COO}^-)$ ($\sim 1586\text{ cm}^{-1}$) in both spectra indicate that the carboxylate form of L-cysteine is preserved after chemisorbed on the surface of Ag. The broad peak appearing around $3000\text{-}3400\text{ cm}^{-1}$ in the black spectrum is attributed to the N-H stretching of hydrogen bonded NH_3^+ of L-cysteine. After adsorbed on the surface of Ag, both COO^- and NH_3^+ stretching modes become weaker, which is likely due to the screening-induced decrease in the dipole moments of the two groups in the presence of Ag. Moreover, the NH_3^+ stretching band shows a considerable blue-shift, indicating the strong electrostatic interaction between the NH_3^+ and COO^- groups.

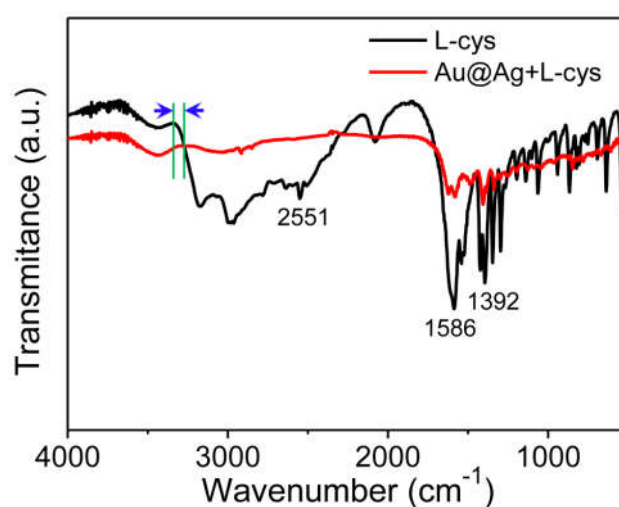


Figure 4.2 FT-IR spectra of L-cys and Au@Ag/L-cys solution.

Besides, ^1H NMR technique was applied to investigate the interaction between the cysteine molecules and the Ag surface as shown in Figure 4.3. The two peaks at ~ 4.01 and 3.08 ppm in the ^1H NMR spectrum of the L-cysteine solution can be assigned to the protons attached to α and β carbons, respectively. After adsorbed on the Au@Ag CSNCs, the two peaks of the L-cysteine shift to 3.11 and 4.0 ppm, respectively. The peak shifts of the β carbon proton is assumed to be sensitive to the molecular binding to the Ag surface through sulphur donor and the shift of the α carbon proton is expected to sense the electrostatic interaction between the NH_3^+ group and the Ag surface. Comparison of the chemical shifts of the α carbon and β carbon protons suggests that the electron density of the two groups around the S- and N-donors of the ligand changes in the Au@Ag CSNC/L-cysteine complex. This is because the presence of the Au@Ag CSNCs can create inhomogeneous magnetic fields and thus the local chemical environment has changed. Moreover, the chemical shift of the β carbon proton is larger compared to that of the α carbon one, which may be due to a shorter distance between the β carbon proton and the Ag surface. These results clearly confirm the conformational change of cysteine before and after absorption on the surface of Au@Ag CSNC.

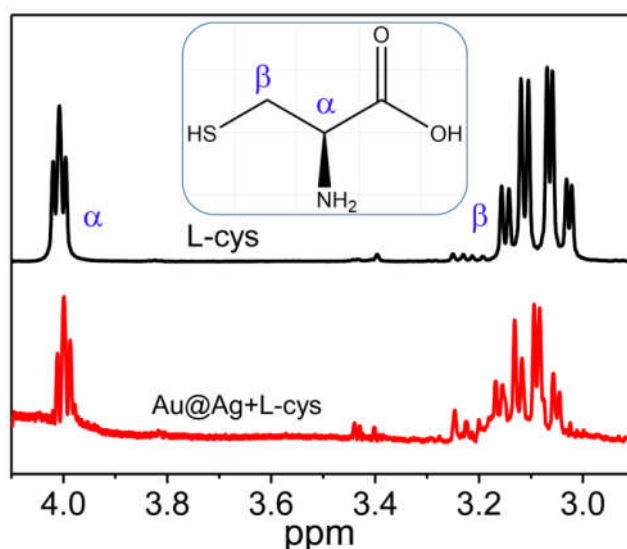


Figure 4.3 ^1H NMR spectra of L-cysteine and L-cysteine absorbed Au@Ag CSNCs solution.

4.4 Interband Absorption Enhanced CD

4.4.1 The Unusual Observed CD in Au@Ag/cysteine System

Figure 4.4 (a) shows the extinction spectra of as-prepared solutions of pristine L- and D-cysteine, bare Au@Ag CSNCs, L- and D-cysteine-adsorbed Au@Ag CSNCs. It can be seen that the L- and D-cysteine molecules have the same absorption response peaked below 200 nm. The extinction spectrum of the Au@Ag CSNCs exhibits four well-defined plasmon bands, which are located at, from low to high energy, 620, 463, 422 and 346 nm; the first two peaks are ascribed to the longitudinal and transverse dipolar modes, similar to the plasmon resonance bands of an Au NR,³⁷ and the latter two to the octupolar and multipolar modes, respectively.³⁸ The mode assignment is consistent with the simulated charge distributions and electric near-field profiles shown in Figure 4.4 (b). Upon the adsorption of cysteine, the four extinction bands of the CSNCs show a slight blue-shift in peak position and a decrease in peak intensity, possibly due to the decrease in the local effective refractive index.

The measured CD spectra for the five samples are shown in Figure 4.4 (c). As can be seen, the pure L- and D-cysteine show two mirror-symmetric bisignate CD resonances, manifesting their enantiomer correspondence, in the UV region close to the absorption band of cysteine, and both peak position and spectral profile are similar to those of most other α -amino acids. In sharp contrast, the Au@Ag CSNCs (10 nM) colloid solution has no CD response, consistent with their achiral character. However, upon capping the achiral Au@Ag CSNCs (10 nM) with L-cysteine (1.35 μ M), two bisignate (peak-dip) CD resonances emerge in the UV region, with the short-wavelength one (200 to 240 nm) significantly weaker than the long-wavelength one (240 to 320 nm) in intensity. Since the second bisignate locates neither in the absorption band of the L-cysteine ($\lambda < 220$ nm)^{8,12} nor in the typical plasmon bands of the CSNCs ($\lambda > 350$ nm),^{5,15,22} here we name it a molecule-induced unusual CD and it could originate from conformational change of the chemisorbed cysteine molecules.

In general, it is believed that surface plasmonic fields can accelerate the electronic transition, and thus increase the absorption, of a molecule nearby a metal nanoparticle. This absorption enhancement is responsible for plasmon-enhanced CD response because the enhanced local fields can amplify the absorption difference of right- and left-handed circularly polarized photons,^{8,24} which, unfortunately, cannot account for the CD resonance observed here. Replacing L-cysteine with D-cysteine flips the spectral profile, demonstrating that the observed CD response indeed results from the differential absorption of the left- and right-handed circularly polarized lights by the hybrid system.

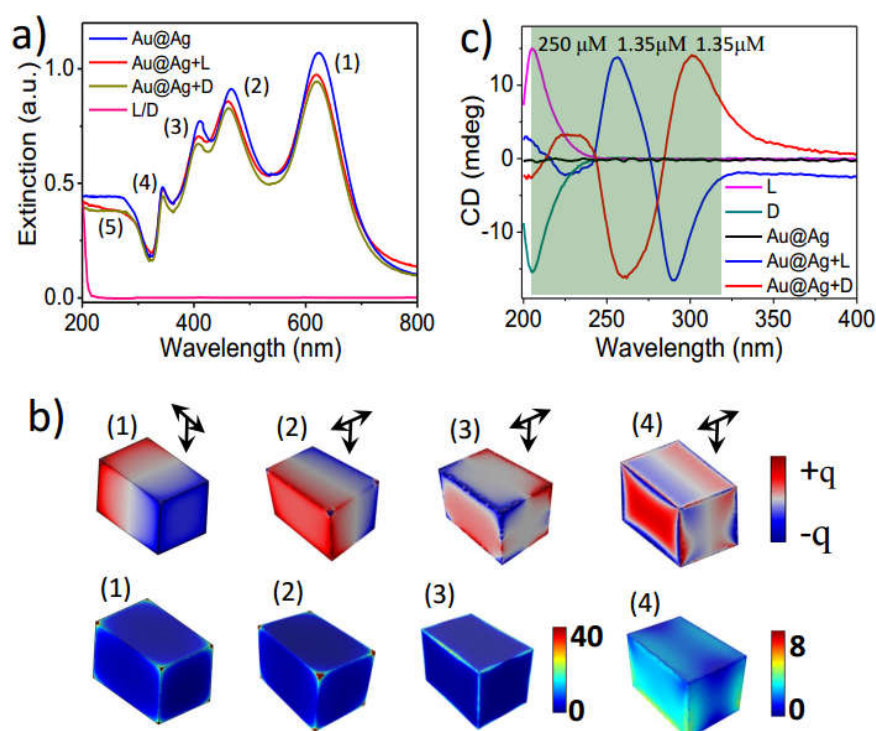


Figure 4.4 (a) Extinction spectra. (b) CD spectra. (c) Simulated surface charge and electric near-field distributions in an Au@Ag CSNC structure at different wavelengths.

4.4.2 The Generality of Observed CD

By defining an enhancement factor $EF_{CD} = CD_{\lambda, \text{new}} / CD_{\lambda, \text{original}}$, where $CD_{\lambda, \text{new}}$ and $CD_{\lambda, \text{original}}$ are the CD signals of pure cysteine and Au@Ag-cysteine complex at their

respective spectral peaks, we estimate EF_{CD} to be ~ 170 for the unusual bisignate CD (~ 15.2 mdeg at 205 and 290 nm for the pristine D-cysteine and the Au@Ag-D-cysteine complex at concentrations of 1.35 μM and 250 μM , respectively). In order to elaborate the generality of the observed Ag-surface-exclusive formation of the proposed extended helical network, we investigate the CD response of cysteine-adsorbed Ag NSs (~ 20 nm in diameter) and Ag NRs (~ 60 nm in length and ~ 30 nm in diameter, see Figure 4.5 and 4.6, which show similar spectral features as the Au@Ag-cysteine systems). To further evaluate the absorption difference, we calculate the anisotropy or dissymmetry factor, g-factor,³² defined as $g = \Delta\alpha/\alpha$, where $\Delta\alpha$ and α are the molar CD and molar extinction, respectively. Using the measured extinction and CD signals at wavelength 290 nm, the g-factor for the Au@Ag CSNCs is determined to be 1.45×10^{-3} , three (two) times that of the Ag NSs/NRs.

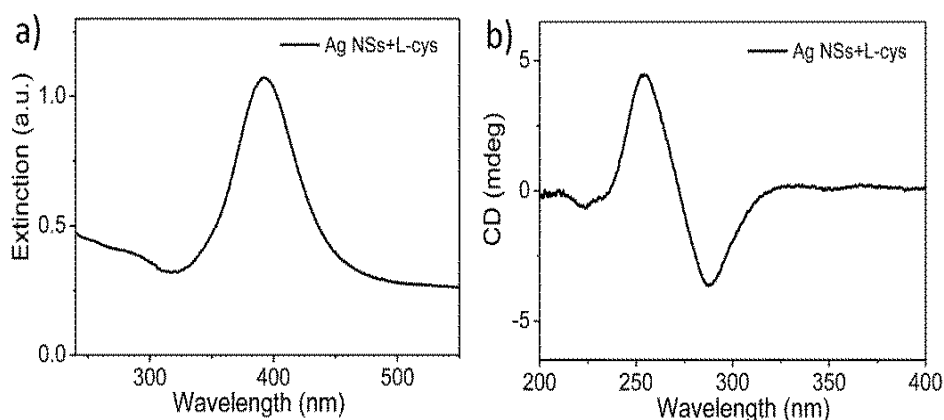


Figure 4.5 UV and CD spectra of Ag NSs/cysteine system.

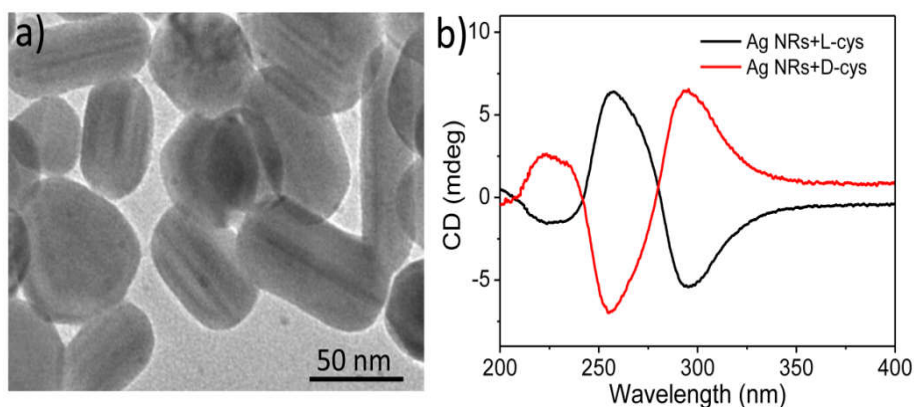


Figure 4.6 (a) TEM of as-prepared Ag NRs. (b) CD spectra of L-/D-cysteine-adsorbed Ag NRs.

4.4.3 Ag-exclusive Feature of Induced CD

Control experiments show that the CD enhancement factor strongly depends on the composition and shape of the metallic nanostructures supporting the chiral molecules. For instance, cysteine-coated Au NRs and NSs exhibit no detectable CD signals (Figure 4.7). Such comparison indicates that the induced CD resonance is exclusive for Ag surfaces. This is probably due to the fact that Ag is more susceptible to environmental changes than Au,³³ and therefore structural changes of chiral molecules could be easier to occur on an Ag surface.³⁵ By comparing with the electric permittivity of Ag shown in Figure 2D, we find surprisingly that the unusual CD bands are located exactly at the interband absorption region of Ag (shadowed area, 220 - 320 nm). It is well known that the large imaginary part of permittivity at 220 - 320 nm is due to the interband absorption of Ag and that the extinction peaks located at 340 - 620 nm are attributed to the excitation of geometry-dependent LSPRs in the Au@Ag CSNCs. In our case, the LSPR bands of the Au@Ag CSNCs are far from the absorption of cysteine and completely off-resonant with each other. Therefore, the enhanced optical activity of the cysteine-coated Au@Ag CSNCs and NSs cannot be fully attributed to the plasmonic enhancement effect as reported in previous studies.^{8,20,36} Moreover, the near-field enhancement factor of the Au@Ag CSNC at 300 nm is much smaller than that at its LSPR bands (see Figure S1), further indicating that the plasmon-enhanced optical activity is not the dominant role in the observed unusual CD resonance.

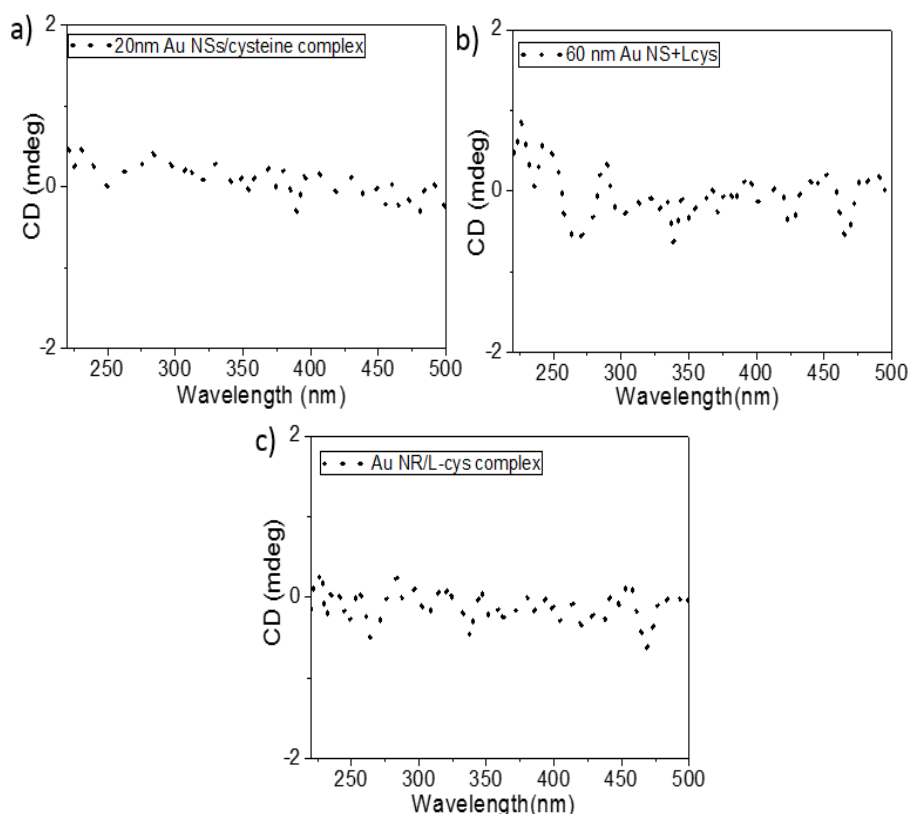


Figure 4.7 Measured CD spectra for L-cysteine-coated Au NSs of diameter 20 nm (A) and 60 nm (B), and (C) Au NRs. All the spectra show no induced CD signal above the level of background noise.

4.4.4 Mechanism Discussion of Induced CD

The above observations are also distinctively different from many of previous theoretical and experimental studies in the following aspects. First, the signal magnitude of the induced UV CD (~ 170 -folds enhancement) is significantly larger than the supramolecular UV CD observed in Ag^+ /cysteine coordination polymers^{18,20} or the plasmon-induced visible CD in chiral molecules capped Au nanostructures,²⁴ both of which are comparable to their native molecular electronic CD. Second, the induced bisignate CD resonance occurs at the interband absorption region of Ag [region (5)] in the extinction spectrum of the Au@Ag CSNCs rather than the

conventional LSPR bands of metal nanostructures [extinction peaks (1-4)], which provides a novel CD enhancement mechanism. Third, the induced CD is observed exclusively for Ag surfaces whereas previously reported plasmon-induced CD is a generic effect for all plasmonic materials including both Ag and Au. These remarkable differences all indicate a different physicochemical mechanism responsible for the observed CD band.

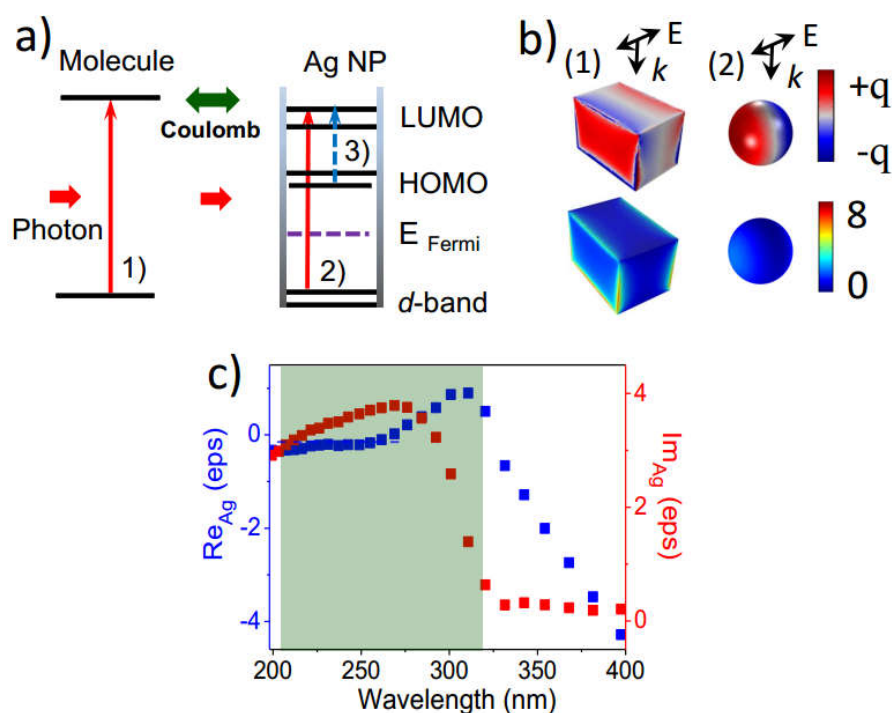


Figure 4.8 (a) Quantum transitions in the cysteine-coated Au@Ag CSNC system. (b) It shows the simulated charge distributions and electric near-field at wavelength 300 nm for an Au@Ag CSNC and Ag NS, respectively. (c) The real and imaginary parts of the electric permittivity for bulk Ag.

As shown in Figure 4.8 (a), the metal-based electronic transitions in the wavelength region of 220 - 320 nm can originate from Ag itself or Columbic coupling induced charge transfer between the metal and the chemisorbed molecules, both depending the local field strength. In either case, the absorbing center should have

different molar extinction coefficients for the left- and right-handed circularly polarized lights, and the extinction inequality results in unequal magnitudes of the left- and right-rotating electric field components of the incident light, giving rise to a differential absorbance quantified by molar ellipticity. This picture seems to be able to explain the difference in dissymmetry factor observed for the Au@Ag CSNC than for the Ag nanosphere because of the much larger electric near-field enhancement factor associated with the former structure (7.52 vs. 1.68) (Figure 4.8 (b)). However, it can not be fully accounted for the observed Ag-exclusive CD resonance because Au also has interband transitions in the wavelength region of 240 - 320 nm. As briefly mentioned earlier, here we propose that the unusual CD resonance arises from the formation of an extended helical network of neighboring cysteine molecules on the Ag surface through hydrogen bonding of their COO⁻ and NH₃⁺ groups, which has a new CD response at ~240 - 320 nm, spectrally matching with the intrinsic interband absorption of Ag thus being enhanced significantly (Figure 4.8(c)). It is because that Ag is more susceptible to environmental changes than Au, so structural changes of chiral molecules could be easier to occur on an Ag surface.^{22,24} Moreover, previous studies demonstrated that an extended helical network of neighboring cysteine molecules through hydrogen bonding of their COO⁻ and NH₃⁺ groups can be easily formed on the Ag surface.¹⁹ To verify this hypothesis, we carried out a series of sophisticated experiments, such as temperature-dependent adsorption-desorption dynamics, pH-switched and ions-suppressed hydrogen bonding of COO⁻ and NH₃⁺, and surface-enhanced Raman spectroscopy. All experiments coherently support the above-proposed mechanism. The temperature-dependent time-evolution and pH switched on or off behaviors of the induced CD observed in the Ag NRs/cysteine system are depicted in following.

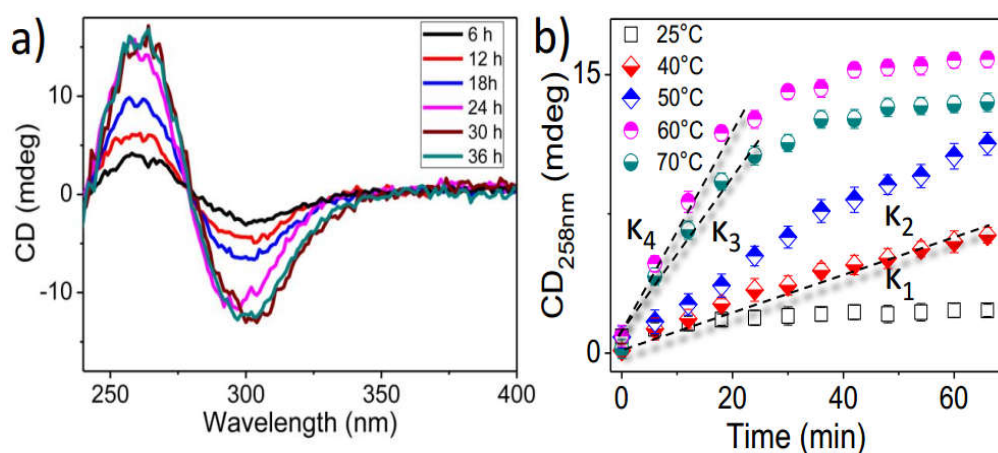


Figure 4.9 (a) Measured CD spectra for the hybrid L-cysteine-coated Au@Ag CSNC as a function of reaction time. (b) Time evolution of the CD as a function of temperature.

The measured temperature-dependent molecular adsorption-desorption dynamics indicates significant conformational changes. In Figure 4.9 (a), at room temperature (25 °C), the CD intensity of the hybrid system increases with reaction time, and reaches saturation after keeping the Au@Ag/L-cysteine mixture for ~24 h. As shown in Figure 4.9 (b), increasing temperature from 25 °C to 60 °C shortens the time required for the hybrid system to reach thermodynamic equilibrium from ~24 h to 30 min. This result demonstrates an accelerated reaction rate for hydrogen bonding of COO⁻ and NH₃⁺ groups at high temperature. Note that only the data points measured during the first 70 min are shown in Figure 4.9 (b) in order to better visualize the intensity change at the onset of reaction, where CD signal intensity of the system increases linearly with time, following with the well-known first-order adsorption kinetics.^{21,28} From the linear fittings, the adsorption rate constant *k* is found to be 0.063, 0.168, 0.390, and 0.512 min⁻¹ for 25, 40, 50, 60 and 70 °C, respectively. At 60 and 70 °C, the adsorption rate constant becomes much smaller after ~30 min, mainly due to adsorption saturation

of cysteine on the surface of the CSNCs, i.e. reaching a dynamic adsorption-desorption equilibrium. Surprisingly, the CD intensity at 70 °C is persistently lower than that at 60 °C, possibly due to heat-mediated desorption of the cysteine molecules and recovery of their conformational changes. Further increase of the temperature to 80 °C results in a much weaker CD signal as compared to 70 °C. It has to be pointed out that the temperature dependence observed in our system distinctively differs from that of sub-3-nm Ag NPs coated with chiral supramolecular structures, where both UV molecular CD and plasmon-induced CD bands diminished upon heating the solution due to incurred disordering of the supramolecular structure.⁵

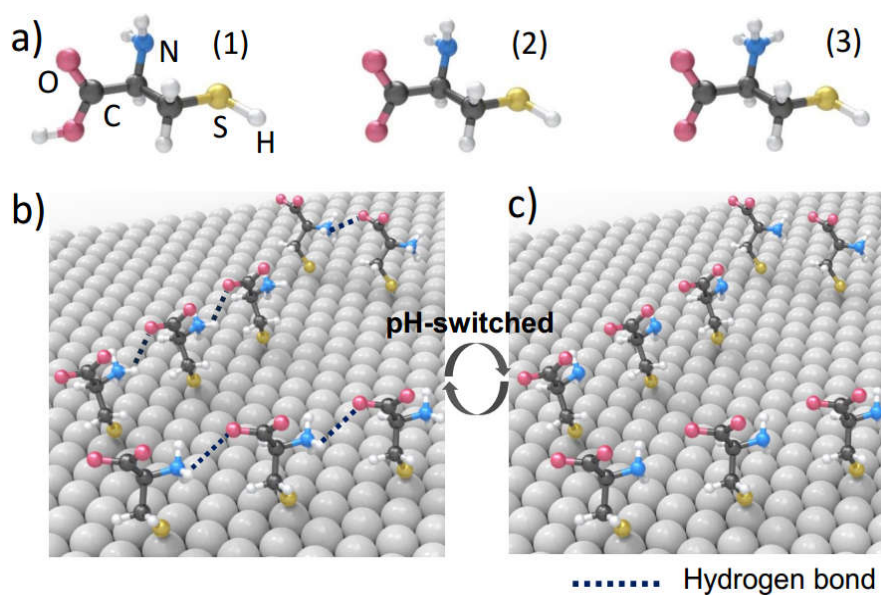


Figure 4.10 (a1-3) Schematic representations of three possible charge states in a cysteine molecule. (b) Formation of an extended helical network and high-pH-enabled dissociation of COOH-NH₂ (right).

The pH-controlled CD activity and silence evidences the linking of COO⁻ and NH₃⁺ groups in cysteine. In general, cysteine has three charge states as shown in Figure 4.10, namely (a) neutral, (b) zwitterionic, and (c) anionic, among which the

zwitterionic state favors forming of an extended helical network on an Ag surface. This can be investigated by monitoring the CD signal of Au@Ag CSNCs/L-cysteine with changing the solution pH. The induced CD signal drops dramatically with increasing pH and becomes negligible at pH = 10. In contrast, the CD intensity remains unchanged under acidic environment. Considering the pKa value of CO₂H (1.9), SH (8.4), and NH₃⁺ (10.7), and the isoelectric point of cysteine (5.2), the CO₂H and NH₂ groups tend to deprotonate to CO₂⁻ and protonate to NH₃⁺ at low pH, respectively, facilitating the electrostatic interaction between zwitterionic cysteine molecules. This sensitive pH responsivity provides an additional degree of freedom to control the CD response of the hybrid system as schematically shown in Figure 4.10.

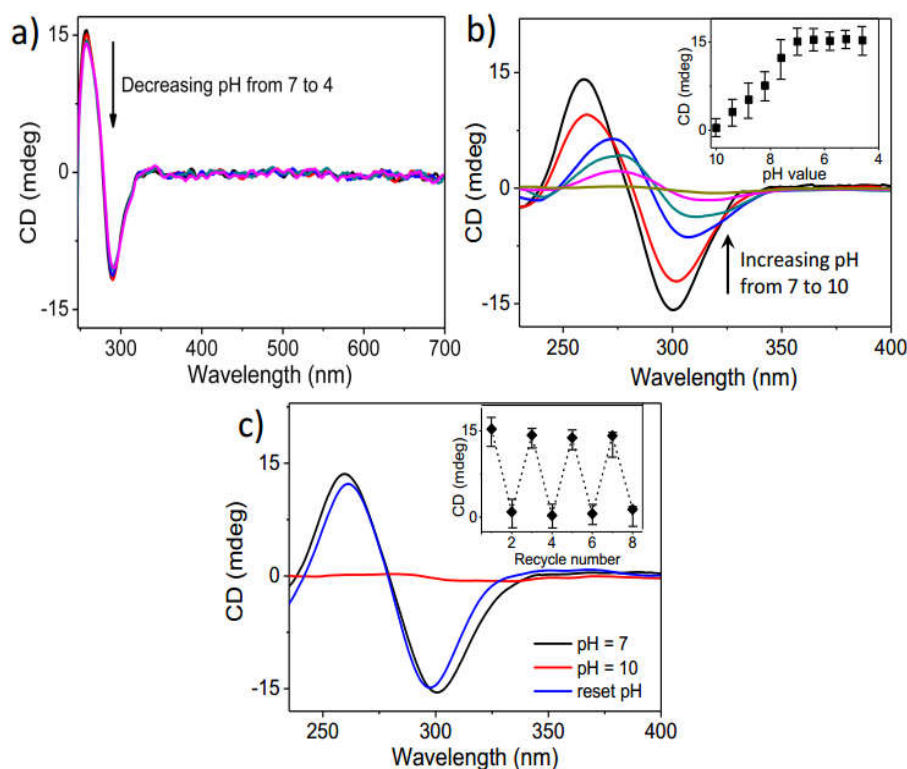


Figure 4.11 (a) Measured CD spectra for the complex with decreasing the solution pH from 7 to 4. (b) Measured CD spectra for the Au@Ag-L-cysteine complex with increasing the solution pH from 7 to 10. (c) pH-switched CD “active” and “silence” of the complex.



Figure 4.11 shows that the induced CD bisignate at pH = 7 disappears at pH = 10, but recovers when resetting pH to 7. It can also be found that the CD intensity keeps unchanged with the decrease of pH. The inset shows that the “on-off” CD signal can be cycled easily by setting the solution pH at 7 and 10 alternatively.

Orientation modulation of adsorbed molecules by negative ions suppresses the induced CD. As shown in Figure 4.12, cysteine molecules vertically orientated on the Ag surface are easier to form hydrogen bonding than those with random orientation. This indicates that disturbing the molecular arrangement could decrease the induced CD by suppressing the formation of extended helical networks on Ag surfaces. To test this effect, we added a certain amount of negatively charged polyelectrolyte (PSS) to the Au@Ag/cysteine system and monitor the CD change as a function of the PSS concentration. The as-prepared Au@Ag CSNCs are positively charged due to the presence of CTAB surfactant, and therefore the PSS ions can easily attach on the Ag surface and, in the meanwhile, significantly disturb the vertical alignment of cysteine molecules due to electrostatic interaction. Consequently, occurrence of hydrogen bonding between COO^- and NH_3^+ groups is suppressed, resulting in the diminished CD. Briefly, the CD intensity decreases from 12.6 to 6.5 mdeg by increasing the PSS concentration from 0.20 to 0.40g/L at a fixed amount. The inset shows that the maximum CD signal intensity measured around 258 nm monotonically decreases with the PSS concentration while the extinction intensity of the complex at 615 nm shows little variation, confirming that the diminished CD does not come from the slight dilution of the complex solution. The pH-switched and ions-suppressed characteristics of CD responses further confirm the helical conformation of chemisorbed cysteine molecules on the surface of Ag.

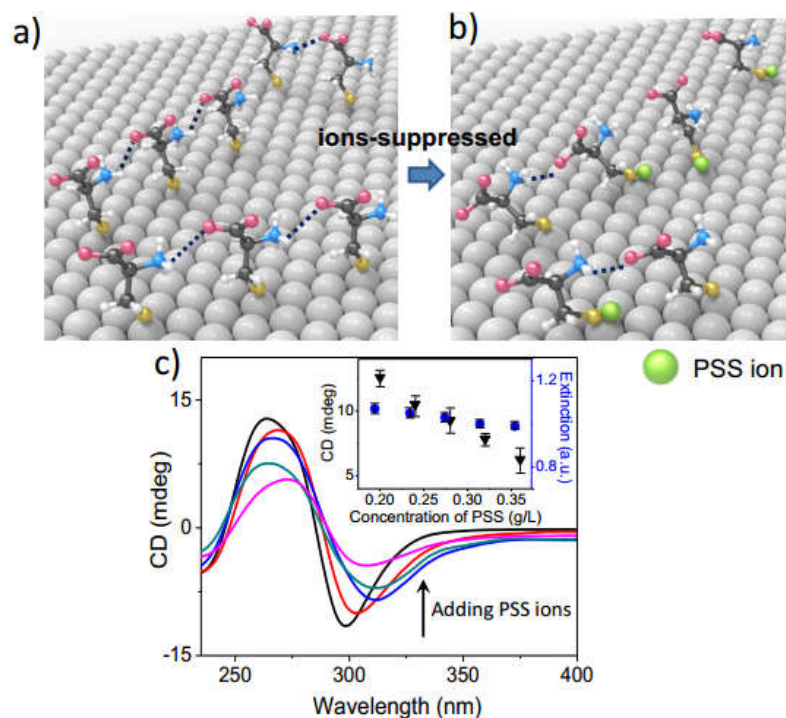


Figure 4.12 (a-b) Schematic diagram showing the block effect of PSS ions. (c) Measured CD spectra for the complex with increasing the PSS concentration.

SERS spectroscopy provides direct evidence of the proposed conformational change by detecting the molecular fingerprint of hydrogen bonding. In combination with structure-based approach, SERS has been used to understand the interfacial interactions in metal-ligand systems, providing a cost-effective and robust technique for analyzing the interactions between metals and cysteine. The measured SERS spectrum for blank Au@Ag CSNCs shown in Figure 4.13 exhibits no detectable peaks above 500 cm^{-1} , demonstrating the cleanness of this SERS substrate. The spectra for the Au@Ag/L-cysteine complex solution measured after mixing them for 1 h and 24 h show a few common spectral features but also some distinctively different characteristics. The strong Raman band observed at 233 cm^{-1} in both spectra can be attributed to the Ag-S bond as the SH group is chemically bonded to the Ag surface. The band at 658 cm^{-1} is assigned to the C-S stretching vibration. The spectrum measured after 1 h exhibits a characteristic peak at 511 cm^{-1} , ascribed to the S-S bond,

which cannot be found in the spectrum measured after 24 h because the new formation of Ag-S bond. However, the latter spectrum shows two intense bands at 892 and 1390 cm^{-1} , assigned to the C-COO⁻ stretching vibration and COO⁻ symmetric stretching vibration, respectively, indicating that the COOH group shortens the distance of COO⁻ from the Ag surface. The Raman peak at 1042 cm^{-1} is assigned to the stretching vibration of the C-N band, which is very weak in an ordinary Raman spectrum. This enhanced Raman intensity evidences the shortened distance between NH₃⁺ and Ag. These distinct SERS enhancement and characteristic vibrations of the functional groups strongly supports the existence of a synergetic interplay between the COO⁻ and NH₃⁺ groups being responsible for the origin of the induced chirality.

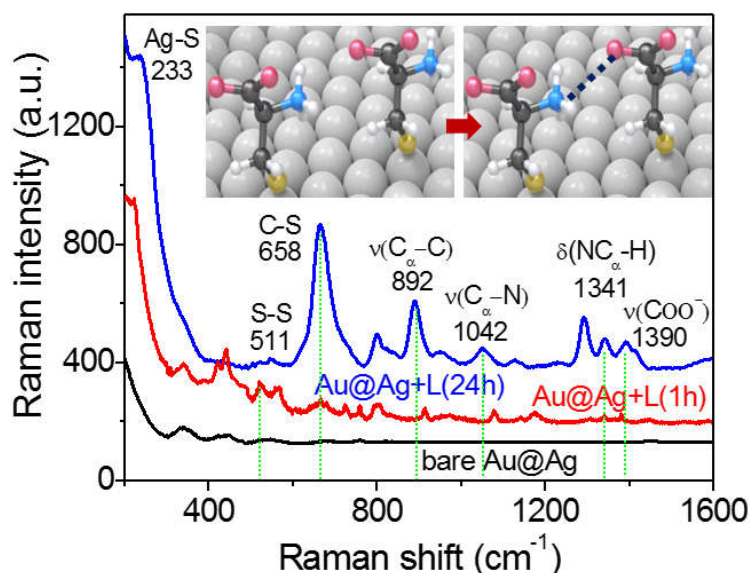


Figure 4.13 SERS spectra of bare Au@Ag CSNCs (black curve) and the complex solution measured with different time.

Other control experiments were also carried out to further confirm our hypothesis and clarify some possibly unambiguous aspects. On one hand, chloride ions were introduced to eliminate Ag⁺ possibly existing in the Au@Ag/cysteine system, after which we observed no changes in either solution color or CD signals (see Figure 4.14). On the other hand, a fresh Ag⁺ solution mixed with L/D-cysteine well reproduces the

CD spectra observed in previous studies (see Figure 4.15) and the CD bands at 360 nm related to the $\text{Ag}^+ \dots \text{Ag}^+$ interaction was observed. These results prove that the induced CD bisignate in our experiment originates from the interfacial interaction of cysteine and Ag.

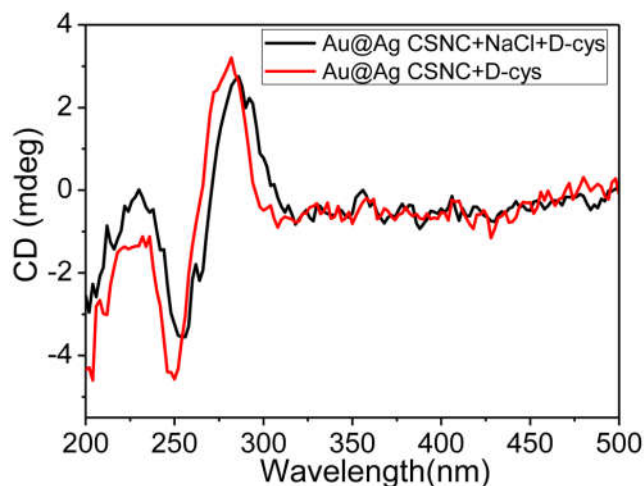


Figure 4.14 Measured CD spectra of the hybrid D-cysteine-coated Au@Ag CSNC with and without adding chloride ions.

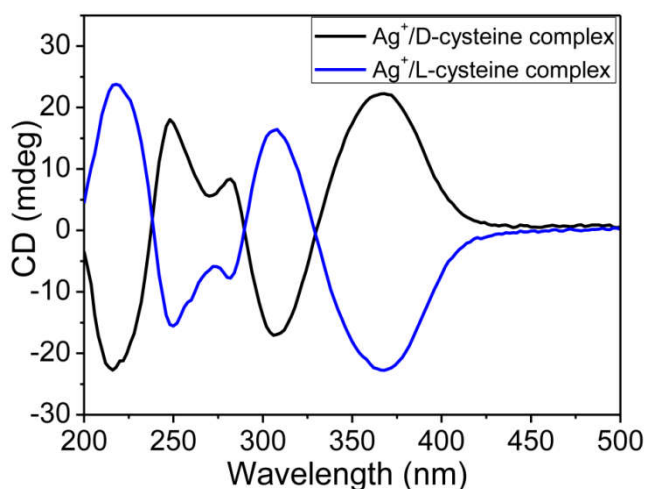


Figure 4.15 Measured CD spectra of Ag^+ -L-cysteine (blue) and Ag^+ -D-cysteine complex (black), reproducing the previous observation of the CD signal at 360 nm due to the $\text{Ag}^+ \dots \text{Ag}^+$ interaction.

4.4.5 Generality of Induced CD for Probing Conformational Changes of Other Molecules

In order to explore the generality of the induced CD for probing conformational evolution and structural rearrangement of general biomolecules, we performed additional experiments with L- and D-penicillamine because they have similar chemical structures as cysteines. The structures of penicillamine, with the two H atoms at the β carbon of cysteine replaced by two methyl groups, are shown in Figure 4.16 (a). CD measurements were carried out for Au@Ag and L/D- penicillamine complex systems, showing very similar spectral characteristics (and a slight blue-shift compared to) as the Au@Ag/cysteine systems shown in Figure 4.16 (b). Interestingly, a more consecutive CD peak appears at ~ 315 nm, which is due to the fact that the two methyl groups at the β carbon also participate in the self-assembly of neighboring penicillamine molecules. Therefore, this observation further confirms that the conformational change of the chiral molecules chemisorbed on the surface of Ag can be spectroscopically monitored. This is of great importance for understanding the molecule-induced UV optical activity.

Hydrogen bonds are often employed as effective intermolecular linkers for arranging a variety of molecules into supra-molecularly ordered structures. For instance, Jonathan et al. reported the realization of an extended two-dimensional network of porphyrin on the surface of Cu at monolayer coverage by forming arrayed hydrogen bonds.²⁵ The particular conformation of cysteine molecules adsorbed on the surface of Ag through hydrogen bonds was also suggested in previous studies. For instance, Fischer et al. observed that zwitterionic cysteine molecules formed a dense-packed layer through the formation of arranged hydrogen bonding upon depositing the molecules on the surface of Ag by sublimation. They proposed that, in the zwitterionic case, the cysteine molecules can optimize the carboxylate-ammonium interaction and exhibit a more regular conformation.²⁶ The proposed mechanism is further verified in

our Au@Ag-cysteine complex that the temperature-dependent time-evolution of the observed CD indicates obvious conformational changes of the chemisorbed cysteine molecules due to temperature-modulated adsorption and desorption rates. Moreover, the observed pH-controlled CD activity and the external ions-suppressed CD strength both support the driving force arising from the hydrogen bonding for structural rearrangement of cysteine molecules, giving rise to the unusual CD resonance.

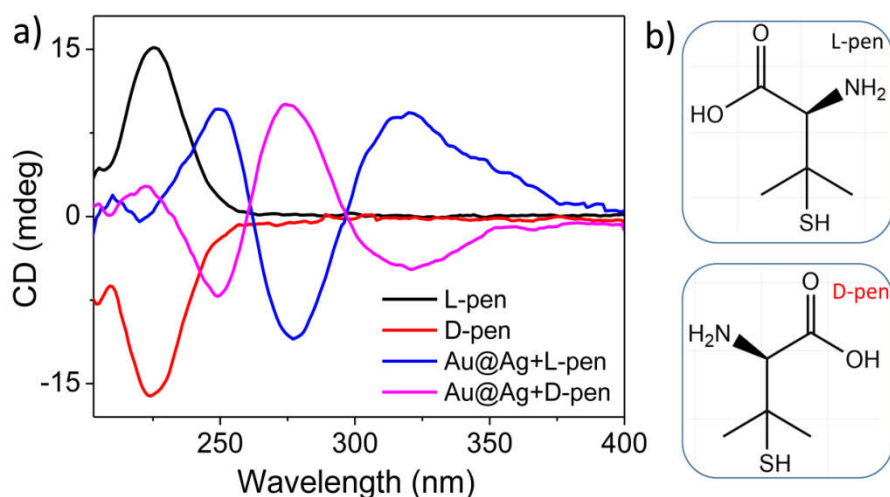


Figure 4.16 (a) CD spectra of L/D-penicillamine, L/D-penicillamine-coated Au@Ag CSNCs. (b) Chemical structures of L/D-penicillamine.

We believe that the presence of two thiol groups attached to the surface of Ag and the hydrogen bond linkage between neighboring molecules are equally important for the new CD resonance. To prove this, we performed a control experiment with two derivatives of L-cysteine, including L-cysteine methyl ester (C-cysteine) and N-acetyl-L-cysteine (N-cysteine). Compared to L-cysteine, the carboxyl group in C-cysteine and amino group in N-cysteine are packed by other chemical groups, respectively. As shown in Figure 4.17, no unusual CD resonance can be observed in the Au@Ag/C-cysteine or Au@Ag/N-cysteine complex compared to pristine C-cysteine or N-cysteine solution.

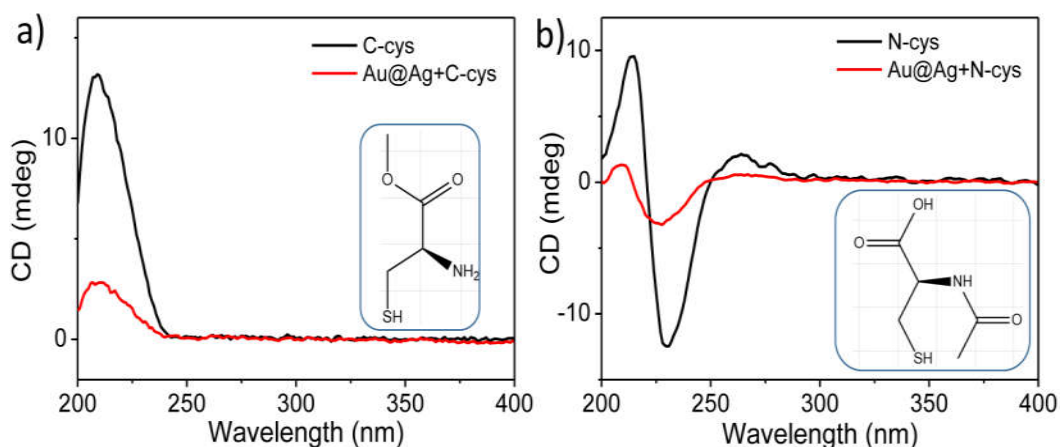


Figure 4.17 (a) CD spectra of pure C-cysteine, C-cysteine-coated Au@Ag CSNCs. (b) CD spectra of pure N-cysteine, N-cysteine-coated Au@Ag CSNCs.

Compared to Au@Ag CSNCs, the complicated preparation process and harsh reaction condition (usually synthesized in oil bath at high temperature) restrict the practical applications of Ag nanocubes. More seriously, it is very difficult to completely remove the remaining precursors, organic macromolecules EG and excess PVP from the surface of Ag according to previous studies (at least 3-5 times centrifugation).^{33,34} To generate the unusual CD resonance observed in our experiment, the condition of the Ag surface is of vital importance because the residual macromolecules may impede the self-assembly of cysteine molecules. In addition, our simulation results indicate that the Au@Ag CSNC has stronger electric field intensity than the Ag nanocuboid with the same dimension (see Figure 4.18). Considering these points, we have selected the Au@Ag CSNCs rather than Ag nanocubes in our experiment.

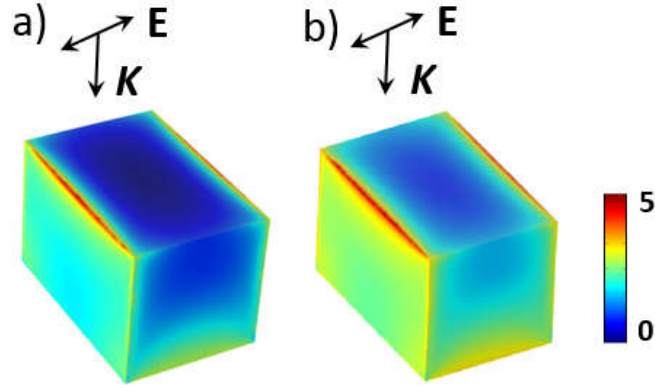


Figure 4.18 Simulated near-field distributions at wavelength 290 nm for an Ag nanocuboid (a) and Au@Ag CSNC (b).

4.4.6 Simulation Model

Finally, a semi-quantitative theory is developed to understand the physical origin of the induced CD. As concluded from our experiments, the interaction between Au@Ag NP (or Ag NS) surface and cysteine molecular networks leads to the formation of a new chiral configuration and the induced CD response. For simplicity without loss of generality, we model the helical networks of spiral molecules with two new CD bands centered at ~ 230 and 275 nm in the case of Au@Ag NPs.

The chirality of the hybrid Au@Ag-spirals system can be expressed as $CD_M = Q_M^L - Q_M^R$, where Q_M^L and Q_M^R are the absorption of Au@Ag NPs for left/right circularly polarized fields. We first consider the incident field with wave vector along z direction, $\vec{E}_0 = E_0(\vec{e}_x + i\eta\vec{e}_y)$, where \vec{e}_x and \vec{e}_y are the unit vectors along x, y coordinate axes, $\eta = \pm 1$ for left/right circularly polarized fields. The absorption coefficient of the hybrid system can be calculated as $Q_M^{L/R} = \omega \text{Im}[\alpha_M] |\vec{E}_M|^2$, where ω is the incident field frequency, \vec{E}_M is the local electric field at the nanoparticle location, and $\alpha_M = V_{NP} \frac{3(\epsilon_0 - \epsilon_1)}{2\epsilon_0 + \epsilon_1}$ is the effective polarizability of the nanoparticle with



V_{NP} the volume of the nanoparticle, ϵ_0 and ϵ_1 the dielectric constants of background and bulk Au. The local field on nanoparticle is determined by the interaction between the nanoparticle and spiral molecules, which is modeled by an effective dipole interaction. Thus, we have the following coupled equations for the local field on nanoparticle and spiral molecules:^[13e]

$$\vec{E}_{cys} = E_x^{cys} \vec{e}_x + iE_y^{cys} \vec{e}_y = \vec{E}_0 + G\vec{p}^M = \vec{E}_0 + G(\gamma_{0x} E_x^M \vec{e}_x + i\gamma_{0y} E_y^M \vec{e}_y)$$

$$\vec{E}_M = E_x^M \vec{e}_x + iE_y^M \vec{e}_y = \vec{E}_0 + G\vec{p}^{cys} = \vec{E}_0 + G(\alpha_{L/R} E_x^{cys} \vec{e}_x + i\alpha_{L/R} E_y^{cys} \vec{e}_y)$$

where $\gamma_{0x} = \gamma_{0y} = \alpha_M$ for spherical nanoparticle, $G\vec{p} = \frac{3(\vec{n} \cdot \vec{p})\vec{n} - \vec{p}}{R^3}$, p refers to the dipole moment of the nanoparticle p^M or spiral molecule p^{spi} . Here $\alpha_{L/R} = \bar{\alpha} \pm \Delta\alpha$, $\alpha_{L/R}$, $\bar{\alpha}$, $2\Delta\alpha$ are the polarizabilities of spiral molecule for left/right circularly polarized fields, the average polarizability, and the polarizability difference between left and right circularly polarized fields, respectively. To the first order of $\Delta\alpha$, the CD can be expressed as

$$CD_M = \frac{\omega \cdot \text{Im}[\alpha_M] \cdot E_0^2}{|1 - \bar{\alpha}\gamma|^2} 2 \text{Re} \left[(1 + \bar{\alpha}^*) \frac{(1 + \gamma)\Delta\alpha}{1 - \bar{\alpha}\gamma} \right].$$

From the above formula, it can be concluded that the system's CD is induced by the spiral molecules (since it is proportional to $\Delta\alpha$) and enhanced by the LSPs of the Au@Ag CSNCs (since it is proportional to the $\text{Im}[\alpha_M]$). Figure 4.19 shows the CD spectra obtained with the derived formula, and the results are consistent with our experimental results by reproducing the two bisignate features with similar spectral positions and signal amplitude contrast.

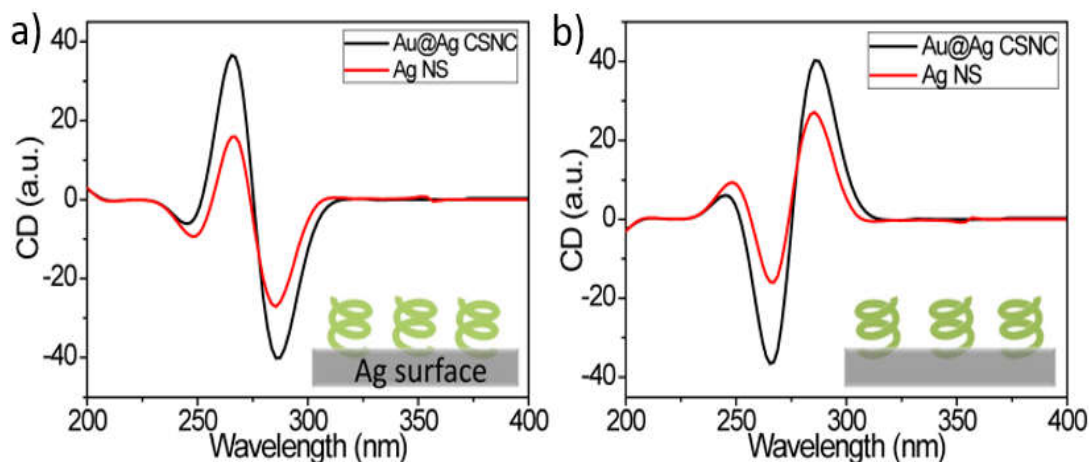


Figure 4.19 Simulated CD spectra for an Ag NS (red curves) or an Au@Ag NP (black curves) capped with vertically-aligned right-handed (a) or left-handed spiral molecules (b), respectively. The insets show the detailed models used in the simulations.

4.5 Summary

We report herein an unusual optical activity induced in discrete Au@Ag CSNC capped with cysteine molecules. Extensive experimental and theoretical investigations reveal that the induced circular dichroism in the hybrid system is due to the formation of many hydrogen-bonding-connected helical networks of chemisorbed cysteine

Figure 4.20 Simulated CD spectra for an Ag NS (red curves) or an Au@Ag NP (black curves) capped with vertically-aligned right-handed (a) or left-handed spiral molecules (b), respectively. The insets show the detailed models used in the simulations.

molecules on the nanostructure surface. This unusual CD response is further amplified through the strong interband absorption and electric field supported in the Au@Ag NP and can be switched on or off (or prompted or suppressed) by controlling environmental conditions such as temperature, pH and added ions. The observed phenomenon is beyond the scope of previous plasmonic chirality studies and opens up



opportunities for extending the use of plasmon-enhanced CD spectroscopies to low-concentration molecular structural recognition in stereochemistry and chirality discrimination in biomedicine.

References

- 1 S.Ostovar, L. Rocks, K. Faulds, D. Graham, V. Parchaňský, P. Bouř., E. W. Blanch, *Nat. Chem.*, 2015, **7**, 591-596.
- 2 A. Kuzyk, R. Schreiber, H. Zhang, A. O. Govorov, T. Lied and N. Liu, *Nat. Mater.*, 2014, **13**, 862-866.
- 3 Y. Wang, J. Xu., Y. Wang., H. Chen, *Chem. Soc. Rev.*, 2013, **42**, 2930-2962.
- 4 N. Cecili., L. G. Ignacio, *Chem. Soc. Rev.*, 2009, **38**, 757-771.
- 5 Z. G. Wang, B. Ding, *Acc. Chem. Res.*, 2014, **47**, 1654-1662.
- 6 B. M. Maoz, R. Weegen, Z. Fan, A. O. Govorov, G. Ellestad, N. Berova, E. W. Meijer, and G. Markovich, *J. Am. Chem. Soc.*, 2012, **134**, 17807-17813.
- 7 Lieberman I., Shemer G., Fried T., Kosower E. M., and Markovich G., *Angew. Chem. Int. Ed.*, 2008, **47**, 4855- 4857.
- 8 T. Nakashima, Y. Kobayashi, T. Kawai, *J. Am. Chem. Soc.*, 2009, **131**, 10342-10343.
- 9 G. Shemer, O. Krichevski, G. Markovich, T. Molotsky, I. Lubitz, A. B. Kotlyar, *J. Am. Chem. Soc.*, 2006, **128**, 11006-11007.
- 10 Z. N. Zhu, W. J. Liu, Z. T. Li, B. Han, Y. L. Zhou, Y. Gao, Z. Y. Tang, *ACS Nano*, 2012, **6**, 2326.
- 11 B. Han, Z. Zhu, Z. Li , W. Zhang, and Z. Y. Tang, *J. Am. Chem. Soc.*, 2014, **136**, 16104-16107.
- 12 L. Xu, Z. Xu, W. Ma, L. Liu, L. Wang, H. Kuang, and C. Xu, *J. Mater. Chem. B*, 2013, **1**, 4478-4483.
- 13 W. Ma, H. Kuang, L. Xu, L. Ding, C. Xu, L. Wang, and N. A. Kotov, *Nat. Commun.*, 2013, **4**, 3689(1-8).



- 14 X. Wu, L. Xu, L. Liu, W. Ma, H. Yin, H. Kuang, L. Wang, C. Xu, and A. K. Nicholas, *J. Am. Chem. Soc.*, 2013, **135**, 18629-18636.
- 15 X. Wang, Y. Wang, J. Zhu, and Y. Xu, *J. Phys. Chem. C*, 2014, **118**, 5782-5788.
- 16 J. S. Shen, D. H. Li, M. B. Zhang, J. Zhou, H. Zhang, and Y. B. Jiang, *Langmuir*, 2011, **27**(1), 481-486.
- 17 T. Li, H. G. Park, H. S. Lee and S. H. Choi, *Nanotechnology*, 2004, **15**, S660-S663.
- 18 R. Randazzo, A. D. Mauro, A. D'Urso, G. C. Messina, G. Compagnini, V. Villari, N. Micali, R. Purrello, and M. E. Fragala, *J. Phys. Chem. B*, 2015, **119**, 4898-4904.
- 19 Q. Zhang, Y. Hong, N. Chen, D. D. Tao, Z. Li, and Y. B. Jiang, *Chem. Commun.*, 2015, **51**, 8017-8019.
- 20 J. Nan and X. P. Yan, *Chem. Eur. J.*, 2010, **16**, 423-427.
- 21 X. Lan, Q. Wang, *Adv. Mater.*, 2016, DOI: 10.1002/adma.201600697.
- 22 S. H. Jung, J. Jeon, H. Kim, J. H. Jung, *J. Am. Chem. Soc.*, 2014, **136**, 6446-6452.
- 23 C. Song, M. G. Blaber, G. Zhao, P. Zhang, H. C. Fry, G. C. Schatz, and N. L. Rosi, *Nano Lett.*, 2013, **13**, 3256-3261.
- 24 W. Liu, Z. Zhu, K. Deng, Z. Li, Y. Zhou, H. Qiu, Y. Gao, S. Chen, Z. Tang, *J. Am. Chem. Soc.*, 2013, **135**, 9659-9664.
- 25 K. Appavoo, D. Y. Lei, Y. Sonnefraud, B. Wang, S. T. Pantelides, S. A. Maier, R. F. Haglund, *Nano Lett.*, 2012, **12**, 780-786.
- 26 Z. Y. Bao, X. Liu, J. Dai, Y. Wu, Y. H. Tsang, D. Y. Lei, *Appl. Surf. Sci.*, 2014, **301**, 351-357.
- 27 H. J. Halas, S. Lal, W. S. Chang, S. Link, P. Nordlander, *Chem. Rev.*, 2011, **111**, 3913-3961.
- 28 D. Y. Lei, K. Appavoo, F. Ligmajer, Y. Sonnefraud, R. F. Haglund, and S. A. Maier, *ACS Photon.*, 2015, **2**, 1306-1313.
- 29 S. P. Rodrigues, Y. Cui, S. Lan, L. Kang, and W. Cai, *Adv. Mater.*, 2015, **27**, 1124-1130.
- 30 E. Hendry T. Carpy, J. Johnston, M. Popland, R. V. Mikhaylovskiy, A. J. Lapthorn,



- S. M. Kelly, D. Barron, N. Gadegaard and M. Kadodwala, *Nature Nanotech.*, 2010, **5**, 783-787.
- 31 Z. Wang, F. Cheng, T. Winsor and Y. Liu, *Nanotechnology*, 2016, **27**, 412001.
- 32 K. C. See, J. B. Spicer, J. Brupbacher, D. Zhang, and T. G. Vargo, *J. Phys. Chem. B*, 2005, **109**, 2693-2698.
- 33 F. Frederix, J. Friedt, K. Choi, W. Laureyn, A. Campitelli, D. Mondelaers, G. Maes, and G. Borghs, *Anal. Chem.*, 2003, **75**, 6894-6900.
- 34 G. Hajisalem, D. K. Hore, and R. Gordon, *Opt. Mater. Exp.*, 2015, **5**, DOI:10.1364/OME.5.002217.
- 35 N. A. Abdulrahman, Z. Fan, T. Tonooka, S. M. Kelly, N. Gadegaard, E. Hendry, A. O. Govorov, and M. Kadodwala, *Nano Lett.*, 2012, **12**, 977-983.
- 36 B. M. Maoz, Y. Chaikin, A. B. Tesler, O. B. Elli, Z. Fan, A. O. Govorov, and G. Markovich, *Nano Lett.*, 2013, **13**, 1203-1209.
- 37 Z. Y. Bao, D. Y. Lei, R. Jiang, X. Liu, J. Dai, J. Wang, L. W. C. Helen, and Y. H. Tsang, *Nanoscale*, 2014, **6**, 9063.
- 38 R. Jiang, H. Chen, L. Shao, Q. Li, J. Wang, *Adv. Mater.*, 2012, **24**, OP200-OP207.
- 39 F. Lu, Y. Tian, M. Liu, D. Su, H. Zhang, A. O. Govorov, and O. Gang, *Nano Lett.*, 2013, **13**, 3145-3151.
- 40 X. Wu, L. Xu, W. Ma, L. Liu, H. Kuang, W. Yan, L. Wang, and C. Xu, *Adv. Funct. Mater.*, 2015, **25**, 850-854.
- 41 Y. Xia, Y. Zhou, Z. Tang, *Nanoscale*, 2011, **3**, 1374-1382.
- 42 Y. Zhao, L. Xu, W. Ma, L. Wang, H. Kuang, C. Xu, and N. A. Kotov, *Nano Lett.*, 2014, **14**, 3908-3913.
- 43 J. M. Slocik, A. O. Govorov, and R. R. Naik, *Nano Lett.*, 2011, **11**, 701-705.
- 44 H. Liu, Y. Ye, J. Chen, D. Lin, Z. Jiang, Z. Liu, B. Sun, L. Yang, J. Liu, *Chem. Eur. J.*, 2012, **18**, 8037- 8041.
- 45 Z. Li, Z. Zhu, W. Liu, Y. Zhou, B. Han, Y. Gao, and Z. Tang, *J. Am. Chem. Soc.*, 2012, **134**, 3322-3325.



46 Z. Zhu, J. Guo, W. Liu, Z. Li, B. Han, W. Zhang, Z. Tang, *Angew. Chem.*, 2013, **125**, 13816-13820.

47 C. Jing, Y. Fang, *Chem. Phys.*, 2007, **332**, 27-32.

48 P. Rezanka, J. Koktan, H. Řezanková, P. Matějka, V. Král, *Colloids and Surfaces A: Phys. Chem. Eng. Aspects*, 2013, **436**, 961-966.

49 C. Jing, Y. Fang, *Chem. Phys.*, 2007, **332**, 27-32.

50 Y. Zhou, M. Yang, K. Sun, Z. Tang, and N. A. Kotov, *J. Am. Chem. Soc.*, 2010, **132**, 6006-6013.

51 Y. Zhou, Z. Zhu, W. Huang, W. Liu, S. Wu, X. Liu, Y. Gao, W. Zhang, and Z. Tang, *Angew. Chem. Int. Ed.*, 2011, **50**, 11456-11459.

52 W. Zhang, A. O. Govorov, G. W. Bryant, *Phys. Rev. Lett.*, 2006, **97**, 146804.

Chapter 5 Au@Pt/C₃N₄ Complex for Plasmon-enhanced Photocatalytic hydrogen Evolution

5.1 Introduction

Photochemical synthesis shows an attractive superiority in comparison with traditional high-temperature chemical reactions.¹ The photocatalytic splitting of water into oxygen and hydrogen using visible light represents a promising approach to the looming energy crisis.²⁻⁴ Photocatalytic reactions require efficient separation and transfer of photogenerated electron-hole pairs in semiconductor,^{5,6} and to achieve higher redox abilities we usually select those semiconductors with higher conduction band and lower valence band. Unfortunately, those semiconductors can only absorb light in short wavelength regions, thereby reducing the efficiency of light utilization. Therefore, how to make the most use of visible or even near-infrared light (NIR) in photocatalytic systems becomes an urgent issue that needs to be addressed.

Graphitic carbon nitride (GCN), with a medium band gap (2.7 eV), is a desired semiconductor matching the potential and bandgap requirements in photocatalytic water splitting reactions.⁷⁻¹⁰ Besides, GCN, possessing a layered sp² hybridization of carbon and nitrogen structure with the formation of π -conjugated planes packed structures, has attracted increasingly growing attention because of its high thermal and chemical stability, abundant elements reserves, nontoxicity, and visible-light response.¹¹⁻¹³ Though GCN exhibits great potentials for H₂ evolution system, it still suffers from low efficiency due to poor light utilization and serious recombination of photogenerated carriers.^{14,15} Loading co-catalyst is an effective way to suppress charge carrier recombination so that it not only traps electrons but also provides effective proton reduction sites, and thus dramatically improves the photocatalytic performance.



A number of methods have been exploited to inhibit the carriers recombination in GCN, such as metal deposition (e.g. Pt,¹⁶ Au,¹⁷ Fe¹⁸), nonmetal doping (e.g. N,¹⁹ B,²⁰ S,²¹ P²²), constructing complex structure coupled with other semiconductors (CeO₂,²³ UIO-66,¹⁴ CdS,²⁴ TiO₂,²⁵ ZnWO₄,²⁶ NiS,²⁷), and so on. However, it is desirable to explore more efficient materials to further optimize the photocatalytic reactivity of GCN.

Plasmon-enhanced photocatalytic reactions are of great significance not only in the field of chemical catalysis on metal surface but also in other surface plasmon fields such as sensor, photon detection, photocatalytic water splitting, etc.²⁸⁻³³ Unfortunately, traditional plasmonic metals have limited surface chemistry, while conventional catalysts are poor optical absorbers. In comparison, noncoinage transition metals have historical precedence as excellent catalysts, yet are generally considered poor plasmonic metals, because they suffer from large nonradiative damping, which results in weak absorption across the visible region of the spectrum. For example, Platinum (Pt), was usually regarded as most efficient H₂ evolution co-catalysts. However, there are still several issues that limit its photocatalyst efficiency due to the fact that: 1) visible light utilization is ultra-low; 2) photon-reduced or chemically synthesized Pt nanoparticles (NPs) modified on photocatalysts normally suffer from nonuniform size distributions, while the large Pt NPs greatly hamper industrial upscaling since normally only surface active-site atoms participate in noble-metal co-catalyst systems; 3) the poor heterogeneous junction. An effective junction between the photocatalysts and co-catalyst is needed because only if in this case can it reduce the aggregation of the supported Pt NPs and facilitate the charge separation. Recently, the photocatalysts composed of bimetal heterostructures have been reported to exhibit enhanced catalytic activity for chemical reactions upon plasmon excitation. Nevertheless, the utilization of anisotropic bimetal/semiconductor heterostructures in the field of photocatalysis has been rarely reported and the mechanism for electron transfer in the system is still ambiguous.



In this chapter, an anisotropic heterophotocatalyst was synthesized for the first time, in which the Au NRs coated by 2-5 nm-Pt NPs were well deposited on the surface of carbon nitride nanosheets (CNNs). Conventional methods in constructing heterocatalysts normally suffer from either poor control over the size of the metal NPs or insufficient charge transfer through the metal/semiconductor interface, which limit their photocatalytic activity. To solve this problem, we construct the photocatalyst by depositing pre-synthesized well controlled colloidal Au@Pt nanostructures to CNNs by removing capping ligands on the Au surface through a ligand-exchange method, which leads to close Au-CNNs contact after a mild annealing process. Here we show that the optical antenna effects of Au NRs can be used to directly enhance light absorption and modify the catalytic activity of directly adjacent reactive Pt NP surfaces, consequently accelerating the light-matter interaction and improving the H₂ productivity. Moreover, compared to monometallic particles, bimetal heterostructures exhibit enhanced catalytic properties and stabilities in general. It is believed that this kind of anisotropic heterostructure would provide the potential for multichannel separation of the photoexcited charges because of the anisotropic junction in the system.

5.2 Experimental Methodology

5.2.1 Synthesis of Samples

The starting Au NRs and Au@Pt nanohybrids were grown according to the previous seed-mediated method as shown in previous chapters.

Bulk C₃N₄ nanosheets were prepared by calcination of melamine powder according to a modified thermal oxidation method. Briefly, 5 g of melamine was put into an alumina crucible with a cover and calcined at 520 °C for 4 h with a heating rate of 5 °C min⁻¹. After calcination, the obtained bulk C₃N₄ was grounded into powder and then heated at 590 °C for 3 h to prepare C₃N₄ nanosheets. Following that, the



resulting C_3N_4 nanosheets were dispersed in glycol followed by sonication for 4 h. The final product was centrifuged and dried at 80 °C for overnight.

In this experiment, identical amount (10 mL, 10 nM) of the selected Au NRs and five Au@Pt NRs were added separately to 50 mg CNNs followed by 10 mL glycol solution being added under vigorous stirring, and then these CNNs were spontaneously coated on Au@Pt NRs through a chemical bonding and self-assembly process. The amino-groups modified on the CNNs can readily replace the CTAB on Au NRs (Au@Pt NRs) due to their high affinities to Au. The subsequent removal of these ligands and the formation of close Au NR/CNNs (Au@Pt/CNNs) contact were obtained by the evaporation and annealing method (heating samples in the furnace at 120 °C for 2 h). The resulting product was washed with distilled water and ethanol several times, and was dried in oven at 40 °C overnight. While for the control sample Au/Pt/CNNs (0.01 wt% Pt loading), the H_2PtCl_6 (0.01 M, 240 μ L) was added into previously prepared Au NR/CNNs solution via illumination by Xe lamp for 6 h. For the Au@Pt NSs/CNNs samples (0.01 wt% Pt loading), the approach is similar to that of Au@Pt NR/CNNs except that the Au NRs were replaced by Au NSs.

5.2.2 Hydrogen Production and Photocurrent Experiments

Hydrogen production experiments were carried out in a Pyrex top-irradiation glass reactor connected to a closed gas-circulation system. The photocatalyst powder (40 mg) was transferred into a 100 ml triethanolamine aqueous solution (15 vol.%, served as the sacrificial agent). After stirring for 10 mins, the whole solution was irradiated from the top of the reactor by a 300 W Xe lamp with a cut-off filter ($\lambda > 420$ nm). The temperature of reactant solution was maintained constantly at 10 °C by a flow of cooling water during the reaction process. The H_2 gas was quantified by an on-line gas chromatograph (Techcomp, GC7900) with a TCD detector and a packed column (5Å molecular sieves, 2 mm \times 4 mm).

The photocurrents were measured using the same instrument within a

conventional three-electrode configuration, in which a platinum sheet as the counter electrode and a saturation calomel electrode (SCE) as the reference electrode. To fabricate working electrodes for carrying out the photocurrent measurements, the ethanol dispersion of Au@Pt/CNNs samples ca. 0.15 mg mL^{-1} was uniformly spin-dropped on the ITO-coated glass at 2500 rpm by a desktop spin coater (TC 100 spin coater MTI Corporation China) firstly. Then the ITO glass with liquid film was held at $120 \text{ }^\circ\text{C}$ for 120 min to volatilize the ethanol, and $0.05 \text{ M H}_2\text{SO}_4$ aqueous solution was used as the electrolyte. The light source was a 300 W Xe lamp with a cut-off filter ($\lambda > 550 \text{ nm}$).

5.2.3 Morphological and Componential Characterization of samples

In order to obtain high active photocatalyst with anisotropic junction, the preparation process plays a key role and the synthetic method is the important foundation. In this work, the formation of the Au@Pt/CNNS anisotropic hybrid structure involves a three-step process, as explained in the Experimental Section and shown in Figure 5.1.

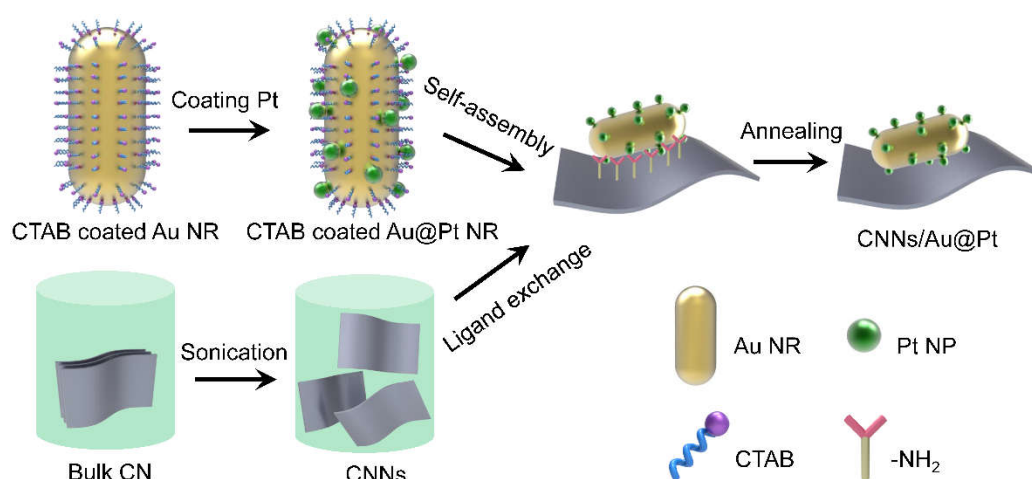


Figure 5.1 Schematic illustration of the preparation of the Au@Pt/CNNs anisotropic

heterogeneous nanostructure.

Firstly, the Au NRs were prepared by a seed-mediated growth approach.^{34,35} Then Pt ions were reduced on the synthesized Au NRs for the formation of Au@Pt hybrid nanostructure. Simultaneously, bulk CN was transmuted into CNNS precursor by a two-step calcination process and then CNNS were obtained by a liquid exfoliation route from CNNS precursor in water/glycol solution ($v_{\text{wat}}:v_{\text{gly}}=1:1$). In the following, a predefined mass ratio of the as-prepared CNNS and Au@Pt NRs were dispersed in water under vigorous stirring, and then these CNNS were spontaneously coated by Au@Pt NRs through a chemical bonding process. The amino-groups on the CNNS can readily replace the original ligand (CTAB) of Au NRs due to their high affinities to Au at ambient temperature.³⁶ The subsequent evaporation and annealing method further complete removal of the ligand and therefore benefit the electron transfer process. It is worth mentioning that the thermal treatment temperature of 120 °C is lower than that required in the conventional deposition-precipitation method.³⁷

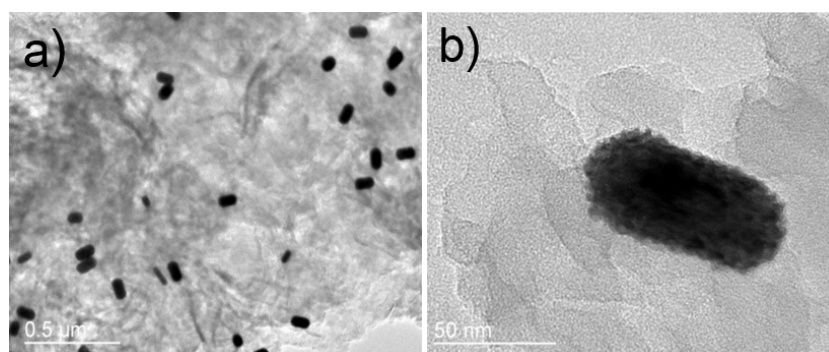


Figure 5.2 Morphological characterizations of Au@Pt/CNNS anisotropic heterogeneous nanostructures.

Anisotropic junction is closely related to the morphology and structure of material. Figure 5.2 shows TEM images of the Au@Pt/CNNS anisotropic nanostructure, where one can see that the Au@Pt NRs are uniformly distributed on the

surface of CNNs without aggregations. It shows a single Au@Pt/CNNs nanostructure, in which it is facile to find that the NR is decorated with tiny Pt NPs. Note that the small CNNs are highly facet, which is beneficial for the photocatalytic reactions.

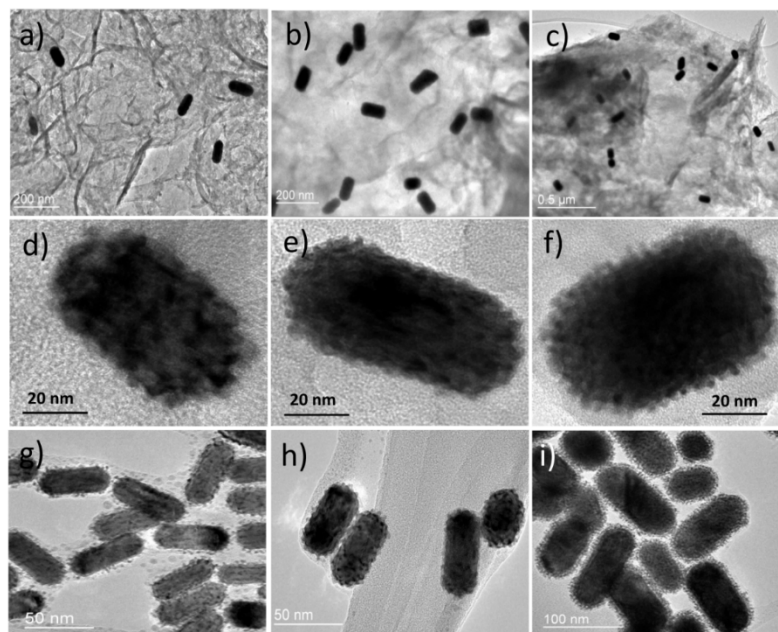


Figure 5.3 TEM images of different Au@Pt/CNNs anisotropic heterogeneous nanostructures with various Pt loading.

To investigate near field effect and plasmonic behavior in the Au NR governed by the dielectric variation in the shell, we employed the finite-element method, implemented in the multi-physics COMSOL software, to calculate the electric near-field enhancement factors for the Au@Pt hybrid structures and the bare Au NR excited at wavelength 700nm with incident polarization along the long axis of the rod. Here the dielectric response of the shell on the Au NR (52 nm in length and 22 nm in diameter) is modelled as an effective medium consisting of air and Pt NPs (3 nm in diameter) with the volume fraction of Pt determined from the TEM images shown in Figure 5.3 (3.26%, 4.96%, 6.77%, and 14.53% for Au@Pt-0.006, -0.008, -0.01 and -0.02 wt%, respectively). Figure 5.4 presents the field intensity distribution profiles for the Au NR and four kinds of Au@Pt hybrids, which show that the field intensity is suppressed gradually with increasing volume fraction of Pt.

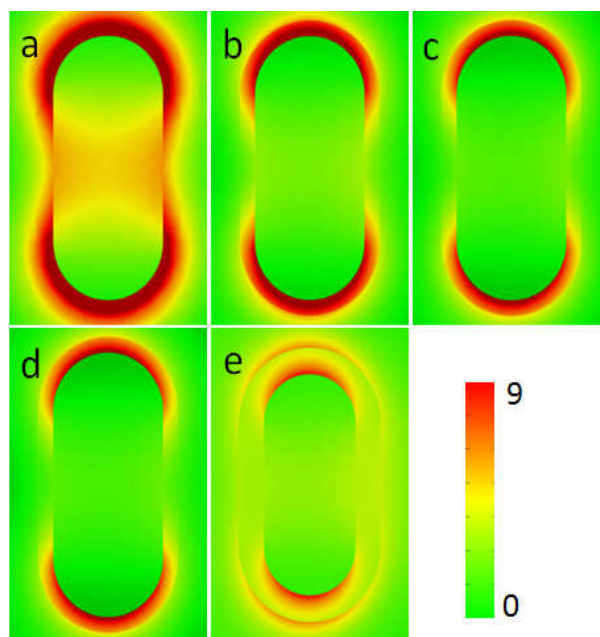


Figure 5.4 Cross-sectional view of the normalized electric-field intensity distribution profiles for the bare Au NR (a) and Au@Pt hybrids (b)-(e).

5.2.3 The Advantages of Samples with Anisotropic Configuration

It needs to point out that such a configuration is particularly important for achieving strong dual functionalities because of the robust catalytic activity of sub-5 nm Pt NPs with large surface area-to-volume ratio and a significantly enhanced local electromagnetic field originated from Au NRs with nanometer-scale gaps. Figure 5.5(a) indicates that most of the Pt NPs are single-crystalline and the measured lattice spacing of 0.22 nm corresponds to the (111) plane of Pt. Figure 5.5 (b) is the STEM image of a single Au@Pt NR coated on CNNs, while (c) and (d) show the element mappings of Au and Pt in the hybrid nanostructure. For comparison, we perform the control experiment and synthesize the Au NR/CNNs hybrid structure. Figure 5.5 (e) and (f) show HRTEM and SEAD images for an Au NR/CNNs nanostructure, in which the measured lattice spacing of 0.20 nm corresponds to the (200) plane of Au, and the

bright periodic lattice points further confirm the single crystal nature of Au. The HRTEM further reveals that the whole surface of each Au NR is uniformly coated with a number of well-dispersed, discontinuous Pt NPs with diameters of 2-5 nm. Moreover, the blur aureoles shown in Figure 5.5 (f) imply the poor crystallinity of CNNs, indicating the inferior conductivity of CNNs. Thus, it is indispensable to ameliorate the electron transfer capability aiming to improve the photocatalytic reactivity.

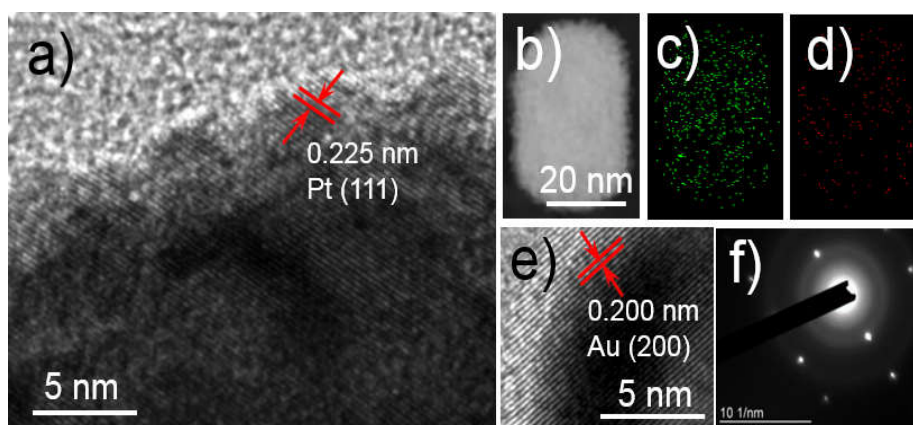


Figure 5.5 (a) HRTEM images of CNNs/Au@Pt NR anisotropic heterogeneous nanostructures. b) STEM image of single Au@Pt hybrid deposited on CNNs. c, d) Elemental mapping of Au and Pt in the Au@Pt hybrid, respectively. e, f) HRTEM and SEAD images for single CNNs/Au NR nanostructure.

5.2.4 The Electric Property and Chemical Status of Samples

The crystalline and electronic structures as well as the structure related optical properties of the CNNs, Au NR/CNNs, Au/Pt/CNNs and Au@Pt/CNNs were studied by recording their X-ray diffraction (XRD) patterns, optical absorption and Raman spectra (Figure 5.6 a-d). As presented in Figure 5.6 (a), the CNNs shows two peaks at $13.0^\circ(100)$ and $27.6^\circ(002)$, which are consistent with those of previously reported values for the CNNs. Compared to pure CNNs, the Au/CNNs, Au/Pt/CNNs and Au@Pt/CNNs samples exhibit three additional peaks at 38.1 , 44.3 , and 64.6° , which

are indexed as the (111), (200), and (220) planes of Au, respectively. These results indicate that the Au NRs are successfully loaded on the CNNs and the CNNs keep the nanostructure unchanged after annealing. Nevertheless, the diffraction peaks of Pt are absent for the samples of Au/Pt/CNNs and Au@Pt/CNNs, probably due to its low loading content. Figure 5.6 (b) shows the UV-Vis absorption spectra for the Au NRs and Au@Pt hybrid structures. Au NRs display two absorption peaks at 533 and 715 nm (black curve), corresponding to the transverse and longitudinal localized surface plasmon resonances (LSPRs), respectively.

It is noted that the Pt particles themselves have no observable absorption characteristic peak in the visible range. The absorption spectrum of Au@Pt NRs clearly demonstrates that the two LSPR modes of Au NRs would be dampened. This could be attributed to the existence of Pt on the surface of Au NRs, which prevents efficient excitation of surface plasmons by light and also provides additional ohmic loss channels to plasmon decay. Moreover, the slightly red-shift of the two LSPR modes may be due to the strong coupling between the Au NR and Pt NP. Figure 5.6 (c) shows the Raman spectra of the synthesized four samples, recorded with a 488 nm laser as the excitation source. It is obvious that the pure CNNs and CNNs composite nanostructures show similar Raman patterns. It further confirms that the CNNs can keep the identical nanostructure after the annealing process. To be specific, the characteristic peaks of the C-N extended network at 1040 and 1236 cm^{-1} are attributed to the different types of ring breathing modes of s-triazine.¹⁵

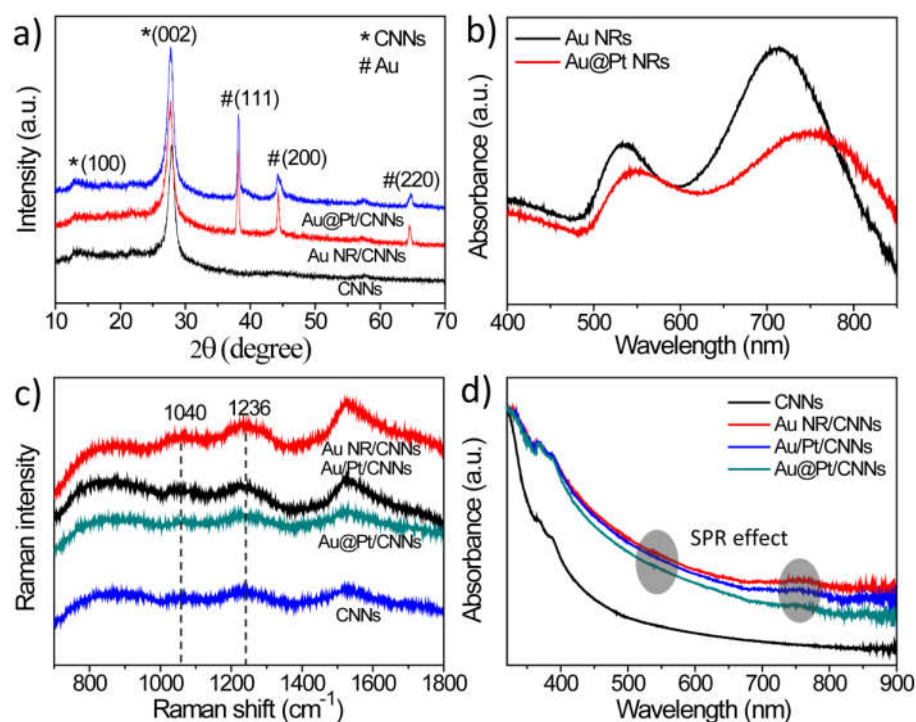


Figure 5.6 a) XRD patterns of different CNNs samples. b) UV-vis spectra of Au NR and Au@Pt hybrids. c, d) Raman and UV-vis characterizations of different CNNs samples.

Moreover, compared with pure CNNs, the Au NRs/CNNs composite undoubtedly show much stronger Raman signals due to the SPR effect. While the Raman intensity of Au/Pt/CNNs nanostructures is a bit higher than that of the Au@Pt/CNNs ones, indicating a weaker electric near field induced by the latter one. UV absorption spectra were measured to determine the optical properties of the prepared samples, and the results are shown in Figure 5.6 (d). It can be seen that the pure CNNs present an absorption edge about 470 nm, which corresponds to a band gap of 2.65 eV, resulting in a low visible light utilization efficiency. Whereas the Au NRs/CNNs, Au/Pt/CNNs and Au@Pt/CNNs samples exhibit an obviously enhanced broad absorption across the whole visible spectra region, especially for the peaks at around 540 nm and 750 nm located at the transverse and longitudinal LSPR positions

of Au NR, respectively. The slightly lower absorption of Au/Pt/CNNs and Au@Pt/CNNs compared to the Au NR/CNNs in the 450-900 nm could be attributed to the dampening effect of Pt decorated on Au NRs, being consistent with the previous Raman and UV measurements. Benefiting from such enlarged light absorption range and intensity, these unique and anisotropic hybrid plasmonic photocatalysts are expected to enhance the solar energy utilization efficiency in the photocatalysis process, showing improved visible-light driven photocatalytic performance.

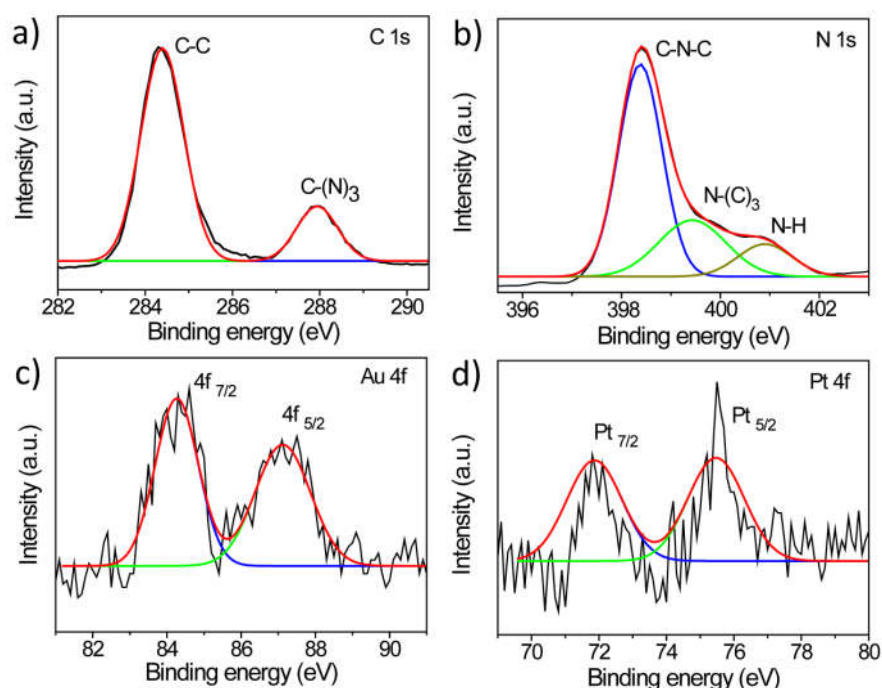


Figure 5.7 XPS spectra of (a) C 1s, (b) N 1s, (c) Au 4f and (d) Pt 4f of the Au@Pt/CNNs anisotropic heterogeneous nanostructure.

The XPS spectra were carried out to further analyze the detailed electronic and chemical status of the sample. As observed from Figure 5.7, the C 1s spectrum can be deconvoluted into two peaks at binding energies of 284.5 and 288.0 eV, which are attributed to pure graphitic sites in the carbon nitride matrix (C-C) and the sp^2 -hybridized carbon in the aromatic ring attached to the amino group (C-(N)₃), respectively. The N 1s spectrum can be fitted into three peaks, ascribable to C-N-C at 398.2 eV, N-(C)₃ at 399.5 eV, and N-H at 401.1 eV. While for the Au 4f and Pt 4f

spectra shown in (c) and (d), they both consist of two relatively weak peaks, well in agreement with the Au⁰ and Pt⁰ state values.³⁸ These amino groups can strongly attach to the Au surface, which pave the way to formation of Au@Pt/CNNS anisotropic hybrid structure. Moreover, the CNNS colloidal suspension is negatively charged according to previous studies,¹⁴ while the Au NR and Au@Pt NRs are positively charged, thus the CNNS and NRs can combine together by a self-assembly method due to the electrostatic reaction (More Au NR/CNNS morphological characterizations are presented in Figure 5.8). In brief, a valid junction between the CNNS and co-catalyst is prerequisite for an effective charge separation that can facilitate the high-performance photocatalysis reaction.

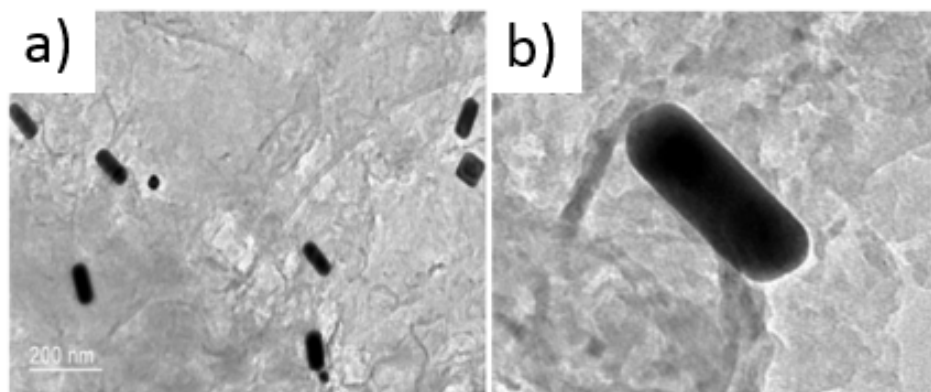


Figure 5.8 TEM images of Au NR/CNNS heterostructure (The scale bar in two Figures is 200 nm).

5.2.5 The Hydrogen Evolution Experiments

Figure 5.9 (a) compares the photocatalytic H₂ evolution performance of Au NR/CNNS, Au/Pt/CNNS, Au@Pt/CNNS (0.01 wt% Pt loading, Pt content was calculated based on the elemental weight distribution) and bare CNNS. It should be noted that in this study CNNS alone gives a very low activity with a negligible H₂ evolution level, which may be due to the small quantity of CNNS added and the serious recombination of photogenerated carrier-pairs. With Au NR as co-catalyst, the



photocatalytic activity has a little improvement with a H₂ evolution of 9.61 μmol h⁻¹ because Au itself has a limited surface chemistry activity and the Au NRs with large size also restrict the hydrogen evolution. While for the Au/Pt/CNNs photocatalyst, a notable improvement of H₂ evolution with 52.52 μmol h⁻¹ were observed, which can be ascribed as the synergistic effect between Au and Pt co-catalysts (detailed morphological characterizations of Au/Pt/CNNs are shown in Figure 5.10). Besides, the optical antenna effects of Au NRs would be used to directly enhance light absorption and scattering, therefore, modify the catalytic activity of those adjacent reactive Pt NP surfaces.³²

However, this type of material has its own shortcomings: 1) photo-reduced or thermal-reduced Pt NPs usually have a nonuniform size distribution and the large Pt NPs greatly hamper the photocatalytic efficiency; 2) those Au NRs and Pt NPs are randomly distributed on the CNNs surface, therefore it is impractical for Au NRs to improve the absorption of each optically insensitive Pt NP, which is a common conundrum that need to be addressed. However, in the anisotropic Au@Pt/CNNs hybrid structure system, the Au NR is an optical antenna where every single Pt NP decorated on the Au antenna acts as a reactor of H₂ evolution.

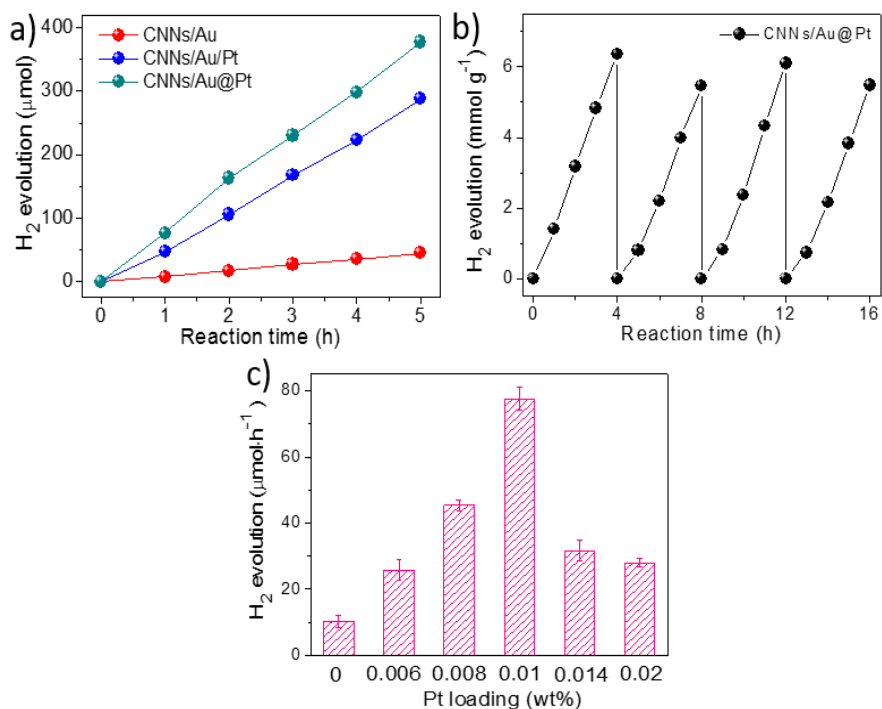


Figure 5.9 a) Time course of H₂ evolution over Au NR/CNNs, Au/Pt/CNNs and Au@Pt/CNNs photocatalysts. b) Photocatalytic H₂ generation activity of Au@Pt/CNNs (0.01 wt% Pt loading). c) Photocatalytic activity comparison of Au@Pt/CNNs with various Pt loading.

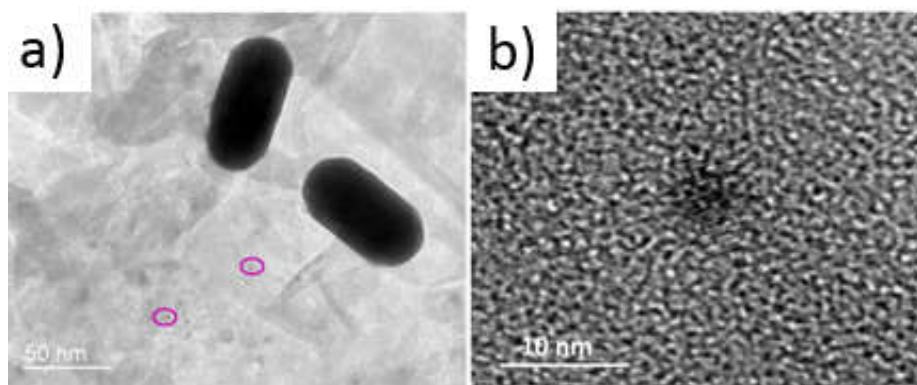


Figure 5.10 TEM and HRTEM images of Au/Pt/CNNs hybrid nanostructure.

This “antenna-reactor” complex, with the antenna and reactor composed of two distinct materials, is predominant due to the fact that the incident light energy can be squeezed into a nanoscale volume around the Au NR, thereby largely enhancing light-



harvesting capacities and the local field strength of Pt NPs, consequently improving the H₂ production efficiencies. Therefore, it is reasonable to observe the highest H₂ generation rate of 76.62 μmol h⁻¹ over Au@Pt/CNNs (Figure 5.10 (a)). As far as we know, this is the highest value of H₂ production of CNNs in the plasmon-assisted water splitting system. Besides, the stable H₂ evolution rate of Au@Pt/CNNs (0.01 wt% Pt loading) in the test further reflects the stability of single “antenna-reactor” complex in the framework of CNNs. As shown in Figure 5.10 (b), during each cycle of 4 h test, almost the same amount of hydrogen was generated, and no significant decay in the photocatalytic activity was observed in 16 h of our investigation. The high stability can be attributed to the intrinsic erosion-resistance of the Au@Pt NPs and CNNs, and their robust contact constructed by the method of ligand-exchange and mild annealing. It was found that even more Au@Pt/CNNs photocatalysts were introduced in the reaction system, it still exhibits a linear increase of activity, providing a potential benefit for industrial upscaling.

In addition, the varied H₂ evolution rates based on an optimized surface coverage of Pt in the anisotropic nanostructures were also investigated. Such an optimized H₂ evolution can be achieved due to the fact that large-area coating of Pt on an Au NR significantly degrades its near-field enhancement while little Pt loading will suppress active spots of the photocatalytic system. The Au@Pt/CNNs exhibits an approximately linear increase of activity when the Pt loading contents are varied from 0.006 to 0.01 wt% with an average H₂ generation rate of 24.85 to 76.62 μmol h⁻¹, as shown in Figure 5.10 (c). However, when the Pt loading contents exceed 0.014 wt%, the activity suddenly decrease. This could be attributed to following reasons: It is obvious that overloaded Pt content cannot trigger bigger Pt particle growth, but it would suppress the absorption and SPR effect of Au, limiting the light utilization efficiency of the whole system. More importantly, the superfluous Pt NPs existence between the CNNs and Au NRs can seriously restrict the electron transfer channels, and therefore decrease the life time of these electrons. To be specific, on one hand,

hydrogen overvoltage of Pt (0.01 V) is lower than that of Au (0.18 V), making it possible for electrons transfer from Au to Pt.³⁹ While for CNNs, it is known that the photogenerated semiconductor exhibits higher conductivity due to more charge carriers created in the structure by the excitation. Therefore, CNNs could serve as an excellent electron generator for the rapid transport of the photogenerated electrons to its supported Au NRs. This is feasible because the conduction band of CNNs with near -1.12 eV (vs. NHE) is lower than the work function of Au (5.1 eV). It means the Au NR could act as an electron transfer mediator and “freight station”, which is helpful for the effective electron separation and transportation from the conduction band of CNNs to Pt NPs.

5.2.6 Mechanisms for the plasmon-enhanced hydrogen evolution

This kind of multi-channel electron transfer process is believed to prolong the average electron life time, and finally leads to a giant photocatalytic performance improvement. On the other hand, SPR-excitation of Au NRs generated hot electron-hole pairs, and the hot electrons transiently occupied empty states in the Au conduction band above the Fermi energy, further energetically injected to the Pt NPs, with the holes left on the VB of Au NRs. These holes can partly neutralize the photogenerated electrons from the conduction of CNNs or serve as an oxidizer to react with TEOA. In both cases, the photogenerated charge carrier separation can be boosted, and the electron transportation process was accelerated as well. The schematic diagram for electron transfer pathway and reaction mechanism for H₂ evolution will be systematically discussed in following.

Further insight into the electron transfer behavior was revealed by PL-quenching and fluorescence-lifetime experiments as shown in Figures 5.11 (a) and (b). A wide emission peak centered at about 460 nm is observed, which could be attributed to the band gap recombination of photoexcited electron-hole pairs in CNNs.³⁹ These results

show that, in the presence of Au NR, there is unambiguous quenching of the PL intensity and an increase in the fluorescence lifetime, indicating that the recombination of carriers is suppressed and the separation of electron-hole pairs is visibly improved. A clear blue-shift of PL spectra can be observed which may be due to the shifting of conduction and valence bands in opposite directions, as well as the decrease of the interlayer conjugation strength of CNNs.¹⁴ These embed co-catalysts among layered CNNs can serve as effective electron separation supporters.

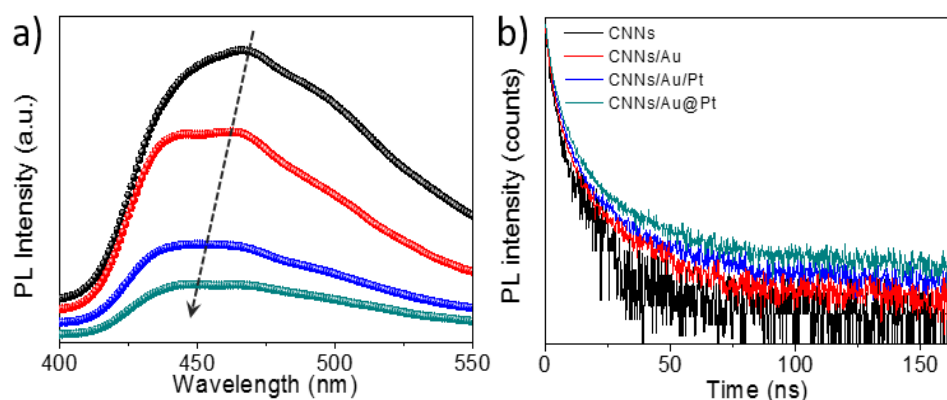


Figure 5.11 (a) PL spectra and (b) decay curves of CNNs, Au NR/CNNs, Au/Pt/CNNs and Au@Pt/CNNs photocatalysts.

From the decay curves fitted well with a tri-exponential function, we can calculate that the average lifetimes for CNNs, Au NR/CNNs, Au/Pt/CNNs and Au@Pt/CNNs are 5.43 ns, 7.33 ns, 7.86 ns and 9.77 ns, respectively. The longest lifetime obtained by the Au@Pt/CNNs composite could be ascribed to multi-channel electron transfer from the conduction band of CNNs to Au and then to Pt, as well as the SPR-excited hot electrons decay from Au conduction band to Pt. This result confirms the modulation of the charge transfer pathway by building the anisotropic junction structure is favorable to the separation of photogenerated carriers and also such structure will undoubtedly be propitious to the photocatalytic reactions.

Surface plasmon resonance (SPR) of plasmonic nanostructures could help to enhance the solar light harvesting by several ways. For instance, scattering (far field) mechanism, charge transfer mechanism, local electric field enhancement mechanism

and so on.^{42,43} In order to explore the mechanism for electron transfer process in this water splitting system, photocurrent tests with different irradiation energy were performed systematically. Compared to pure CNNs, CNNs/Au@Pt heterostructures shown in Figures 5.12 (a) and (b) display a significant photocurrent increase in the visible light range. To be specific, under the same irradiation energy intensity in different wavelength ranges (> 420 , 495 and 645 nm), the photocurrent of CNNs/Au@Pt heterostructures was enhanced 2.7, 11.7 and 8.6 times, respectively. Different mechanisms can be attributed to the varied photocurrent augmentation with altered irradiation wavelength range in the anisotropic hybrid nanostructure.

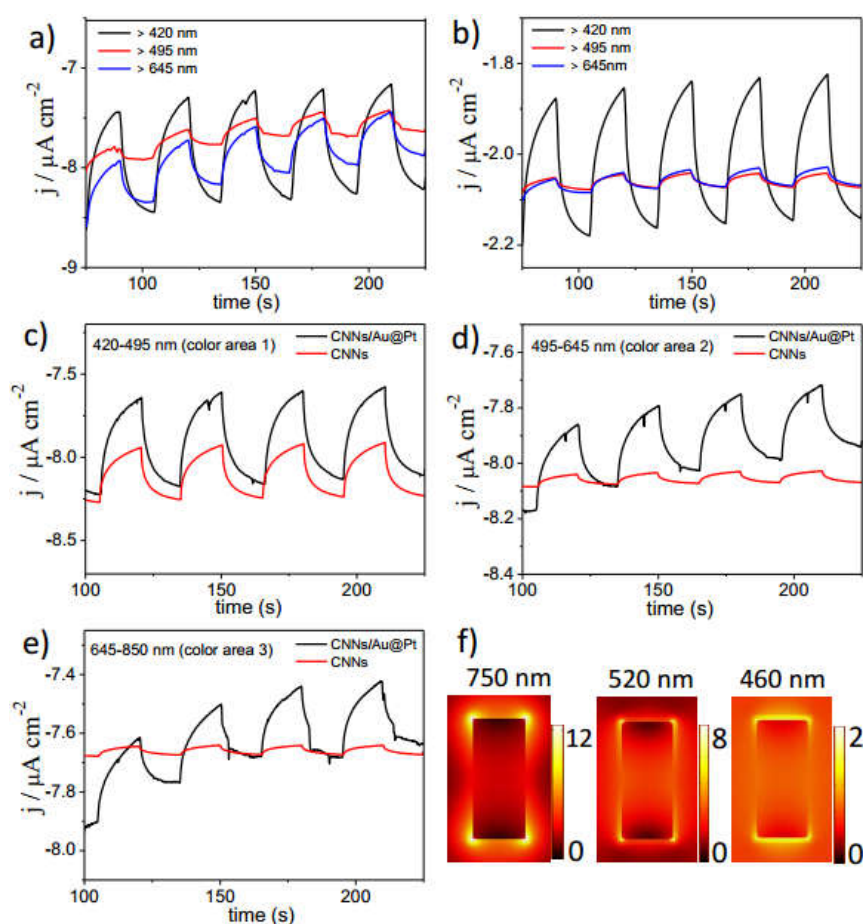


Figure 5.12 Photocurrent-time dependence of (a) CNNs and (b) Au@Pt/CNNs anisotropic heterogeneous nanostructure under different light irradiation. (c)-(e) Photocurrent-time dependence of (a) CNNs and (b) Au@Pt/CNNs anisotropic heterogeneous nanostructure under different wavelength range irradiation. (f)

Calculation spatially averaged E-field enhancement at 460, 520 and 750 nm of Au@Pt.

Figures 5.12 (c), (d) and (e) reveal that, compared to CNNs, the photocurrent of CNNs/Au@Pt heterostructures in the water splitting reaction under 420-495 nm irradiation has shown 1.6 time enhancement, while for 495-645 nm and 645-850 nm the enhancement values are 14.7 and 8.7, respectively. In other words, using the CNNs/Au@Pt heterostructures, the photocurrent produced in 420-495 nm wavelength region contributes 56.25% to the total hydrogen evolution; while in 495-645 nm and 645-850 nm regions, they are 27.5% and 16.25% respectively. However, for the CNNs in the same wavelength regions, the corresponding portions are 90%, 5% and 5%. Therefore, after attachment of Au@Pt hybrids onto CNNs, the contribution to the hydrogen production efficiency for longer wavelength regions is fairly increased. This confirms the ability of the hybrid plasmonic photocatalysts to distinctly improve the solar energy utilization efficiency in the photocatalysis process, showing enhanced wavelength-dependent photocatalytic performance. In 420-495 nm range, the inherent energy match between the incident light and the CNNs absorption can greatly boost the carrier generation in CNNs/Au@Pt hybrids. In this case, more photogenerated carriers in CNNs can reach the semiconductor-metal interface before recombination, and therefore, contribute to the photocatalysis. On the other hand, the 495-645 nm and 645-850 nm region, which include the transverse and longitudinal LSPR of Au NR, give much stronger photocurrent enhancement than that of 420-495 nm (14.7 and 8.7 vs 1.6). In addition to aforementioned charge transfer mechanism within CNNs, in the longer wavelength range (>495 nm), the local electric field enhancement generated from the plasmonically active Au NRs should play an important role in photocatalytic process because the electric field intensity of local plasmonic “hot spots” can be greatly improved compared to the incident electromagnetic field. Plasmon resonance can result in an increased amount of hot electrons generated and transferred into the Pt. Previous studies confirm that the bimetal Au@Pt hybridstructure catalysts can

exhibit pronounced hydrogen evolution upon resonant plasmon excitation due to greater number of interfaces for hot electrons transfer.^{40,41} Moreover, strongly localized electric field provides a way to relieve carrier diffusion problem by coupling light effectively from the far-field to the near-field at the heterostructures interface. As a result, most of the photogenerated charge will diffuse to the surface and contribute to catalysis.

To further reveal the mechanism responsible for the observed wavelength-dependent photocatalytic performance as well as the mutative photocurrent augmentation with varied irradiation wavelength range, we employed the finite-element method, implemented in the multi-physics COMSOL software, to calculate the electric near-field enhancement for the hybrid structure at wavelengths of 460, 520 and 750 nm with incident polarization along the long axis of the rod. Here the dielectric function of the shell on the Au NR is modelled as an effective medium consisting of water and Pt NPs (3 nm in diameter) with the volume fraction 6.33% of Pt determined from the TEM images. Calculation results shown in Figure 5.12 (f) illustrate the spatially averaged E-field enhancement, which is in good agreement with the wavelength-dependent photocurrent augmentation performance.

In addition, we have done the control experiments for synthesizing the similar anisotropic structure except Au NRs replaced by Au NSs (TEM images are shown in Figure 5.13).

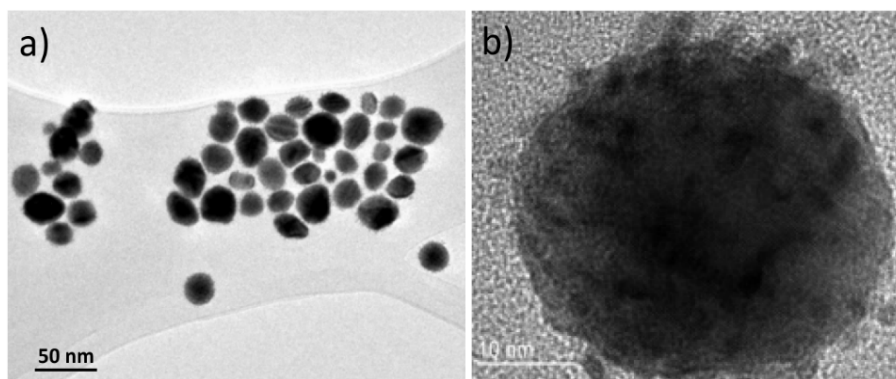


Figure 5.13 TEM images of Au@Pt NSs/CNNs hybrid nanostructure.

The H₂ production results show that H₂ evolution rate of Au@Pt NSs/CNNs is much lower than that of Au@Pt NRs/CNNs. This is due to the fact that spherical Au NPs have a narrow SPR band and only absorb a small portion of visible light, limiting their photocatalytic efficiency (Details related to the H₂ production of Au@Pt NSs/CNNs are shown in 5.14). Moreover, it needs to point out that, the utilization of bimetallic heterostructures in the field of photocatalytic water splitting has also been reported recently. For instance, Pd-modified Au NRs have been reported to exhibit enhanced catalytic activity for chemical reactions upon plasmon excitation.⁴⁰ Pt-Au triangular nanoprisms with strong dipole plasmon resonance for hydrogen generation have been investigated because of the strong electric field and interaction between Au and Pt, resulting in more interfaces for hot electrons transfer.⁴¹

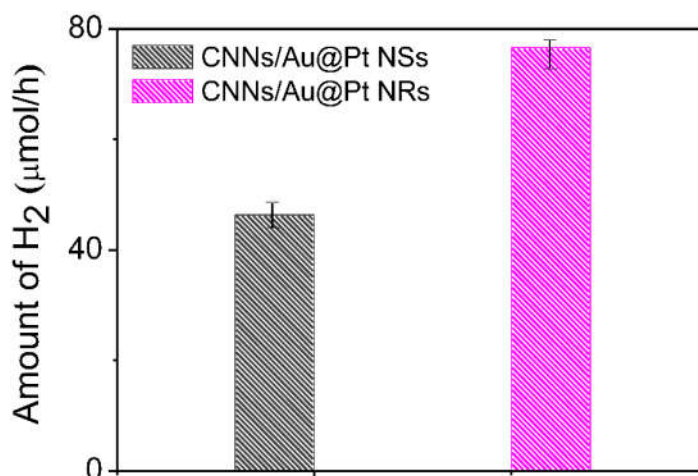


Figure 5.14 Photocatalytic activity comparison of Au@Pt NSs/CNNs and Au@Pt NRs/CNNs with the identical Pt loading.

Benefited from its advanced anisotropic nanostructure fabricated by the unique self-assembly synthesis strategy, the obtained photocatalysts show superior activity to conventionally prepared hybrid photocatalysts in water-reduction hydrogen production under visible-light illumination. Manipulating the materials used for both the plasmonic antenna and catalytic reactor can theoretically lead to numerous

possibilities for controlling plasmon-assisted absorption enhancement and chemical reactivity. We demonstrate this concept by designing the Au@Pt/CNNs nanostructure with optimized parameters, and the reactor exhibits dramatically increased photocatalytic activity over the sum of their individual components. The modularity of this approach provides for independent control of chemical and light-harvesting properties and paves the way for the rational, predictive design of efficient plasmonic photocatalysts. As shown in Figure 5.15 (a), each Au@Pt entity can be seen as a robust “antenna-reactor”, which provides steady and powerful potentials for the H₂ production. The detailed schematic diagram for electron transfer pathway and reaction mechanism for this system was proposed in Figure 5.15 (b).

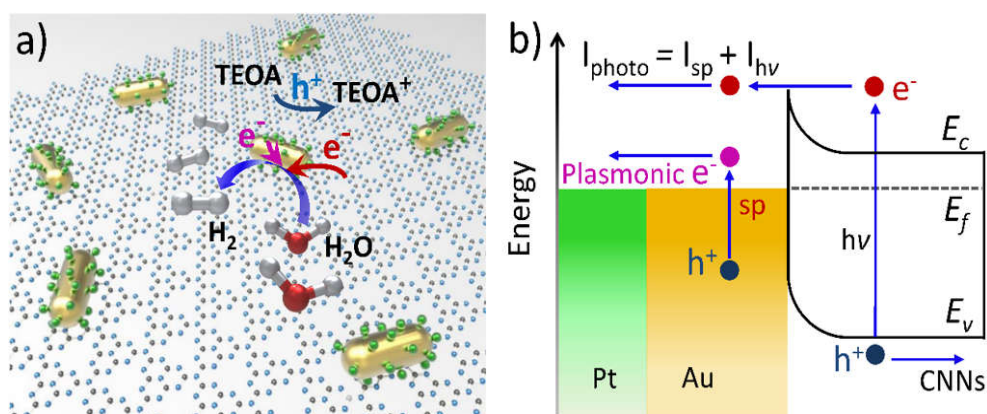


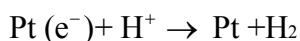
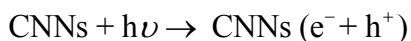
Figure 5.15 Schematic illustration and b) proposed mechanism of H₂ evolution by the Au@Pt/CNNs anisotropic heterocatalyst under visible light irradiation. Route 1) represents the photogenerated electrons from conduction band of CNNs transfer to Au and then to Pt while route 2) indicates SPR-excitation hot electrons of Au transfer to Pt.

It is well known that metal can serve as a sink for the photogenerated electrons or holes when forming a close junction with n-type or p-type semiconductor.⁴¹ The formed barrier can inhibit the backflow of electrons or holes from metal to semiconductor. As a result, the charge “pump” role of the junction ensures the efficient

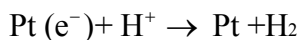
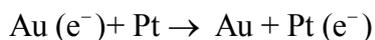
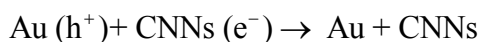
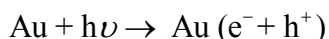


unidirectional transfer of charge carriers across the interface of metal-semiconductor junction. Under visible-light irradiation, the CNNs will be excited and the photoinduced electrons will transfer to Au and then to Pt, and finally react with H^+ to generate H_2 ; while the photoinduced holes would leave on valence band of CNNs to oxidize TEOA, rather than oxidize the OH^- to generate $\bullet OH$ radicals due to lower positive potential of valence band of CNNs (1.49 eV) against standard redox potential of $\bullet OH/OH^-$ (1.99 eV) (shown in Route 1).³⁸ Simultaneously, the hot electrons generated by SPR excitation would transport to Pt and leave the holes in Au. These hot electrons further raise the H_2 production of Pt while the left holes can partially neutralize the photogenerated electrons from the conduction of CNNs or oxidize TEOA to $TEOA^+$ (shown in Route 2). The major routes of photocatalytic H_2 evolution under visible-light irradiation were proposed as follows:

Route 1:



Route 2:



It is demonstrated that such anisotropic hetero nanostructure is favorable to fast separation of charge carrier pairs and results in the holes accumulating in the valence band of CNNs to form oxidation center. While the exciton-induced electrons and SPR-excitation hot electrons sunk in the Pt NPs can be served as active reduction sites. As a consequence, this multichannel electron transfer process decreases recombination rate of photo-excited carriers and significantly prolongs the lifespan of charge carrier

pairs, thus improving the photocatalytic performance.

5.3 Summary

Anisotropic Au@Pt/CNNs have been successfully synthesized by a three-step preparation method. The unique bimetallic NRs in the complex can act as the light antenna and the catalytically active site simultaneously, and exhibit higher performance towards plasmon-enhanced hydrogen production. It was demonstrated that Au@Pt/CNNs eventually possesses tremendously enhanced photocatalytic H₂ generation rate over their individual components, nearly 150% higher than that of Au/Pt/CNNs. This improved photocatalytic activity can be attributed to the valid anisotropic junctions and effective multichannel electron transfer processes. Moreover, an optimized Pt coverage on the Au NRs plays an important role in the photocatalytic system because large-area Pt coating significantly degrades its near-field enhancement and restrict the effective electron transfer pathway while little Pt loading will suppress active spots. It is also revealed that H₂ evolution rate of Au@Pt NRs/CNNs is much higher than that of Au@Pt NSs/CNNs, which is due to the fact that Au NRs have a wide SPR band and can absorb a large portion of visible light. In addition, the modularity of this approach provides for independent control of chemical and light-harvesting properties and paves the way for the rational, predictive design of efficient anisotropic nanostructured plasmonic photocatalysts.

References

- 1 J. D. Holladay, J. Hu, D.L. King, Y. Wang, *Catal. Today*, 2009, **139**, 244.
- 2 A. J. Esswein, D. G. Nocera, *Chem. Rev.*, 2007, **107**, 4022.
- 3 D. Voiry, J. Yang, and M. Chhowalla, *Adv. Mater.*, 2016, **28**, 6197.
- 4 F. E. Osterloh, *Chem. Soc. Rev.*, 2013, **42**, 2294.
- 5 G. Xie, K. Zhang, B. Guo, Q. Liu, L. Fang, J. R. Gong, *Adv. Mater.*, 2013, **25**,



3820

- 6 J. Chen, X. J. Wu, L. Yin, B. Li, X. Hong, Z. Fan, B. Chen, C. Xue, H. Zhang , *Angew. Chem.*, 2015, **127**, 1226.
- 7 X. Wang, K. Maeda, A. Thomas, K. Takanabe , G. Xin, J. M. Carlsson, K. Domen, M. Antonietti, *Nat. Mater.*, 2009, **8**, 76.
- 8 J. Liu, Y. Liu, N. Liu, Y. Han, X. Zhang, H. Huang, Y. Lifshitz, S.-T. Lee, J. Zhong, Z. Kang, *Science*, 2015, **347**, 970.
- 9 D. Wang, Y. Zhang, W. Chen, *Chem. Commun.*, 2014, **50**, 1754.
- 10 Y. Zhang, J. Liu, G. Wu, W. Chen, *Nanoscale*, 2012, **4**, 5300.
- 11 J. Liu, T. Zhang, Z. Wang, G. Dawson, W. Chen, *J. Mater. Chem.*, 2011, **21**, 14398.
- 12 X. Li, W. Bi, L. Zhang, S. Tao, W. Chu, Q. Zhang, Y. Luo, C. Wu, and Y. Xie, *Adv. Mater.*, 2016, **28**, 2427.
- 13 J. Liu, Y. Zhang, L. Lu, G. Wu, W. Chen, *Chem. Commun.*, 2012, **48**, 8826.
- 14 L. Shi, T. Wang, H. Zhang, K. Chang, and J. Ye, *Adv. Funct. Mater.*, 2015, **25**, 5360.
- 15 Li Liu, Y. Qi, J. Lu, S. Lin, W. An, Y. Liang, W. Cui, *Appl. Catal. B: Environ.*, 2016, **183**, 133.
- 16 J. Yu, K. Wang, W. Xiao, B. Cheng, *Phys. Chem. Chem. Phys.*, 2014, **16**, 11492.
- 17 X. Chen, J. Zhang, X. Fu, M. Antonietti, X. Wang, *J. Am. Chem. Soc.*, 2009, **131**, 11658.
- 18 N. Cheng, J. Tian, Q. Liu, C. Ge, A.H. Qusti, A.M. Asiri, A.O. AlYoubi, X. Sun, *ACS Appl. Mater. Interfaces*, 2013, **5**, 6815.
- 19 Y. Hou, Z. Wen, S. Cui, X. Guo, J. Chen, *Adv. Mater.*, 2013, **25**, 6291.
- 20 D. Merki, S. Fierro, H. Vrubel, X. Hu, *Chem. Sci.*, 2011, **2**, 1262.
- 21 G. Liu, P. Niu, C. Sun, S. C. Smith, Z. Chen, G. Q. Lu, H. -M. Cheng, *J. Am. Chem. Soc.*, 2010, **132**, 11642.
- 22 Y. Zhou, L. Zhang, J. Liu, X. Fan, B. Wang, M. Wang, W. Ren, J. Wang, M. Li, J. Shi, *J. Mater. Chem. A*, 2015, **3**, 3862.
- 23 M. Li, L. Zhang, M. Wu, Y. Du, X. Fan, M. Wang, L. Zhang, Q. Kong, J. Shi, *Nano*



Energy, 2016, **19**, 145.

24 J. Zhang, Y. Wang, J. Jin, J. Zhang, Z. Lin, F. Huang, J. Yu, *ACS Appl. Mater. Interfaces*, 2013, **5**, 10317.

25 S. Zhou, Y. Liu, J. Li, Y. Wang, G. Jiang, Z. Zhao, D. Wang, A. Duan, J. Liu, Y. Wei, *Appl. Catal. B: Environ.*, 2014, **158**, 20.

26 L. Sun, X. Zhao, C. J. Jia, Y. Zhou, X. Cheng, P. Li, L. Liu, W. Fan, *J. Mater. Chem.*, 2012, **22**, 23428.

27 J. Hong, Y. Wang, Y. Wang, W. Zhang, R. Xu, *ChemSus Chem*, 2013, **6**, 2263.

28 F. Pincella, K. Isozaki, and K. Miki, *Light-Sci. Appl.*, DOI:10.1038/lssa.2014.14.

29 Z. Bian, T. Tachikawa, P. Zhang, M. Fujitsuka, and T. Majima, *J. Am. Chem. Soc.*, 2014, **136**, 458.

30 P. Wang, B. B. Huang, X. Y. Qin, X. Y. Zhang, Y. Dai, J. Y. Wei, M. H. Whangbo, *Angew. Chem., Int. Ed.*, 2008, **47**, 7931.

31 C. Clavero, *Nat. Photonics*, 2014, **8**, 95.

32 D. F. Swearer, H. Zhao, L. Zhou, C. Zhang, H. Robotjazi, J. M. P. Martirez, C. M. Krauter, S. Yazdi, M. J. McClain, E. Ringe, E. A. Carter, P. Nordlander, and N. J. Halas, *Proc. Natl. Acad. Sci.*, 2016, **113**, 8916.

33 Z. Y. Bao, X. Liu, J. Dai, Y. Wu, Y. H. Tsang, D. Y. Lei, *Appl. Surf. Sci.*, 2014, **301**, 351.

34 Z. Y. Bao, D. Y. Lei, R. Jiang, X. Liu, J. Dai, J. Wang, H. L. W. Chan and Y. H. Tsang, *Nanoscale*, 2014, **6**, 9063.

35 R. B. Jiang, H. J. Chen, L. Shao, Q. Li, J. F. Wang, *Adv. Mater.*, 2012, **24**, OP200-OP207.

36 T. Sainsbury, T. Ikuno, D. Okawa, D. Pacilé, J. M. J. Fréchet, and A. Zettl, *J. Phys. Chem. C*, 2007, **111**, 12992.

37 D. Ding, K. Liu, S. He, C. Gao, and Y. Yin, *Nano Lett.*, 2014, **14**, 6731.

38 J. Xue, S. Ma, Y. Zhou, Z. Zhang, and M. He, *ACS Appl. Mater. Interfaces*, 2015, **7**, 9630.



- 39 A. Tanaka, K. Hashimoto, H. Kominami, *J. Am. Chem. Soc.*, 2014, **136**, 586.
- 40 Z. Zheng, T. Tachikawa, and T. Majima, *J. Am. Chem. Soc.*, 2015, **137**, 948.
- 41 Z. Lou, M. Fujitsuka, and T. Majima, *ACS Nano*, 2016, **10**, 6299.
- 42 W. Hou and S. B. Cronin, *Adv. Funct. Mater.*, 2013, **23**, 1612.
- 43 N. Zhou, L.-P. Vanesa, Q. Wang, L. Polavarapu, I. Pastoriza-Santos and Q.-H. Xu, *RSC Adv.*, 2015, **5**, 29076.

Chapter 6 Conclusion and Future Prospect

Based on the distinctive plasmonic behaviors of Au NRs, I report on my work related to Au NRs on three main topics. Monitoring of catalytic reactions by SERS spectroscopy, interband absorption enhanced CD and preparation of anisotropic heterostructures for plasmon-enhanced photocatalytic hydrogen evolution. The following lists the detailed conclusions and some future plans.

In the first part, I have synthesized Au@Pt core-shell NRs which can be used as a sensitive optical probe for monitoring of the 4-NTP to 4-ATP catalytic reaction. In this core-shell nanostructure, the surface density of Pt NPs has been readily controlled and its effects on the SERS enhancement and catalytic efficiency have been fully examined. In the second part, Au@Ag CSNCs have been synthesized and used to promote the chiral cysteine molecules assembly process by recording the changes in the intensities of induced CD peaks with the reaction time. Comprehensive experiments and simulations reveal that the formation of an extended helical network of cysteine molecules on the Ag surface is responsible for the origin of the new CD band that is strongly amplified by the interband transition of Ag through Coulomb coupling and enhanced local field around the Au@Ag CSNC. In the last part, anisotropic Au@Pt/C₃N₄ nanosheets heterostructures have been prepared for the first time. This kind of nanostructure has been demonstrated to tremendously enhance photocatalytic H₂ generation rate over their individual components. The reason is that each Au NR in the heterostructures serves as the optical antenna while every Pt NP decorated on the Au antenna can act as a reactor of H₂ evolution. Therefore, the incident light energy can be squeezed into a nanoscale volume around the Au NR, leading to the improved H₂ production efficiencies.

Nevertheless, there are still some limitations in this work. For example, the CD

measurement results shown in the second part of this thesis are mainly located in the short-wavelength region. How to tune the CD responses to longer wavelength becomes necessary and urgent.

Next, we intend to study the plasmon-induced CD response by one-dimensional assembly of chiral cysteine and Au@Ag core-shell NRs (GS-CSNRs). In this case, the wavelength range of the CD responses was expected to be manipulated from 340 nm to more than 900 nm through altering the aspect ratios and assembly patterns of GS-CSNRs. Recent studies demonstrate that conjugation of Au NRs with chiral molecules could switch the optical activity, which is usually located in the UV light range for conventional molecular chirality, to the visible wavelength region. This new CD response located at the frequency of LSPR band of the NRs is termed as plasmonic CD, which originates from the Coulombic interaction between the noble metal NPs and the chiral absorbers. This work is meaningful because determination and manipulation of the chirality and corresponding optical activity in the near infrared (NIR) light region is significant to the fields of biochemical sensing, enantioselective catalysis, chiral separation, optical devices, and so on.